

Bachelor Thesis

Observations of ISM features in spectra of hot O and B stars

Submitted to fulfill the requirements for the 'Bachelor of Science (B.Sc.) Physics' to the
department of physics and astronomy at the University of Potsdam



October 2021

Submitted to:
Prof. Dr. Philipp Richter
Chair of astrophysics
University of Potsdam

by:
Florian Runger
Bergstrae 27
14558 Nuthetal
Matricle number: 796724

Contents

List of Abbreviations	3
1 Abstract	4
2 Kurzzusammenfassung	4
3 Introduction	5
4 Theoretical Background	6
4.1 Central Idea	6
4.2 Phases of the ISM	6
4.3 Components of the ISM	7
4.3.1 H II Regions	8
4.3.2 Reflection Nebula	9
4.3.3 Dark Clouds	9
4.4 Extinction and Reddening	9
4.5 Absorption Line Profiles	10
4.5.1 Natural Line Width	11
4.5.2 Thermal Doppler Broadening	12
4.5.3 Other Doppler Broadening Effects	12
4.5.4 The Voigt Line Profile	12
4.5.5 Equivalent Width	13
4.5.6 Computation of Column Densities	14
4.5.7 Saturated vs. Non-Saturated Features	16
4.5.8 Mean Particle Densities	18
4.6 Early Type Stars	18
4.6.1 Reference Spectra	19
4.7 ISM Absorption Features	20
4.7.1 Different Shapes	20
4.7.2 The Na I Doublet	21
4.8 Reference Systems	21
4.8.1 Equatorial Coordinate System	22
4.8.2 Altitude-Azimuth Coordinate System	23
4.8.3 Galactic Coordinate System	24
5 Setup	25
5.1 Corrected Dall Kirkham Telescope	26
5.2 German Equatorial Mount	27
5.3 Working Principle of BACHES - an Echelle Spectrometer	28

6	The Observations	32
6.1	Active Observations	32
6.1.1	Preselection of Promising Stars	32
6.1.2	Selection Criteria	33
6.1.3	Regions of General Interest	34
6.1.4	The Python Routine	35
6.1.5	The Observational Process	37
6.2	Data Processing	40
6.2.1	Data Reduction I - MIDAS	41
6.2.2	Data Reduction II - PySPAN	42
7	Overview on the Data	43
8	Discussion	49
8.1	Calculation of Column Densities	49
8.2	Computation of Mean Particle Densities	50
9	General Scientific Context	51
9.1	Extinction Maps and their use for Intra-/Intergalactic Observations	51
9.2	H I 21cm All-Sky Map	51
9.3	Comparison of ISM Absorption Lines with H I Line profiles	52
10	Peculiar Spectra	54
10.1	V1405 Cas	54
10.2	P Cygni - HIP 100044	56
11	Conclusion	58
12	Python Code	I
12.1	ATTITUDE (Automatized Tool To Identify Tons of Usable Stars with D-line absorption and Extinction) [v0.1.1]	I
12.2	PySPAN - Proceedings of a routine written in MIDAS language	VII
13	Comments on Spectra/Observation Log	VIII
13.1	Archival Data (31.08./01.09.2020)	VIII
13.2	Archival Data (07./08.11.2020)	IX
13.3	V1405 Cas (14./15.04.2021)	IX
13.4	Initial Observation Trial (21./22.04.2021)	IX
13.5	First Major Observation Night (25./26.04.2021)	X
13.6	Second Major Observation Night (26./27.04.2021)	XIV
13.7	Third Major Observation Night (27./28.04.2021)	XVIII
13.8	Fourth Observation Night (07./08.05.2021)	XXV
13.9	V1405 Cas (10./11.05.2021)	XXVI
13.10	V1405 Cas (02./03.06.2021)	XXVI

14 V1405 Cas Finder Chart	XXVII
15 V1405 Cas Na I - Spectra	XXVIII
16 Declaration of Originality	XXXV
17 Star Spectra Plot Sheets	XXXV

List of Abbreviations

AltAz	Altitude-Azimuth
CDK20	20 inch Corrected Dall Kirkham Telescope
Dec	declination
deg	degree (unit)
DSS	Digitized Sky Survey
EBHIS	Effelsberg Bonn H I Survey
GASS	Galactic All-Sky Survey
HIP	abbreviation for Hipparcos (High Precision Parallax Collecting Satellite), an ESA Satellite mission
ICRS	International Celestial Reference System
ISM	interstellar medium
MIDAS	refers to ESO-MIDAS; a system that is utilized for the data reduction
NASA	National Aeronautics and Space Administration
NGC	New General Catalog
OMS	Observatory Management System
RA	right ascension
SDSS	Sloan Digital Sky Survey
SNR	Signal to Noise Ratio
UV	ultraviolet radiation

1 Abstract

The aim of this thesis is to find stars showing absorption fingerprints of the interstellar medium (ISM) in the optical spectrum of hot O and B type stars. The thesis covers the whole observational process deeply described, as well as preparatory steps that have been taken in advance of the observations themselves, which were carried out at the OST in Potsdam, Golm. The observational setup consists of a corrected Dall-Kirkham telescope with 20" in aperture along with the BACHES spectrograph yielding us spectra with a resolution of about $R \approx 20\,000$.

This thesis also describes the development of a Python tool (**ATTITUDE** - **A**utomatized **T**ool **T**o **I**dentify **T**ons of **U**sable stars with **D**-line absorption and **E**xinction), utilized to further plan for observations of potentially promising stellar candidates.

As a result of the extensive data reduction process, a catalog of 39 different stellar systems, also containing information about Na I absorption equivalent widths, W_λ , in their spectra, has been compiled. In addition to that, for stars with noticeable Na I absorption, also the respective column densities, N , have been computed using a curve of growth analysis.

Additionally, another Python program with user interface has been developed, not only performing the curve of growth analysis, but also enabling the user to measure equivalent widths, W_λ , in a graphical, convenient way.

Furthermore, two objects (namely P CYGNI and V1405 CAS) of interest, along with their peculiarities, are discussed more in detail in the final part of this thesis.

2 Kurzzusammenfassung

Ziel dieser Arbeit ist es, heie O und B Sterne zu finden, in deren Spektren sich im visuellen Bereich der spektroskopische Fingerabdruck des ISM offenbart. Die Arbeit beschreibt unter anderem den gesamten Observationsprozess zur Aufnahme der Sternspektren, sowie auch einzelne vorbereitende Schritte dazu. Die Beobachtungen selbst wurden am OST in Potsdam, Golm durchgefhrt. Zur Datengewinnung diente ein korrigiertes Dall-Kirkham Spiegelteleskop mit 20" ffnung in Verbindung mit dem BACHES Echelle Spektrographen, welcher Spektren mit einer Auflsung von zirka $R \approx 20\,000$ liefert.

Des weiteren begleitet diese Arbeit den Entwicklungsprozess des Python Tools "**ATTITUDE**" - **A**utomatized **T**ool **T**o **I**dentify **T**ons of **U**sable stars with **D**-line absorption and **E**xinction, welches der Planung der Observationsnchte und der Auswahl einzelner Sterne, welche ISM Absorptionen in ihren Spektren zeigen knnten, diente.

Als das Resultat ausgiebiger Datenreduktion und -auswertung, konnte ein Katalog, bestehend aus 39 verschiedenen Sternsystemen, unter anderem mit Informationen zu entsprechenden quivalentbreiten W_λ der sich in den Spektren befindlichen Absorptionen des neutralen Natriums (Na I), erstellt werden. Zustzlich konnten mithilfe einer Wachstumskurvenanalyse die entsprechenden Sulendichten N des Na I entlang der Sichtlinie dieser Sterne rekonstruiert werden.

Fr diese Methode wurde ein weiteres Python Programm mit Benutzeroberflche entwickelt. Der Benutzer kann dabei nicht nur eine Wachstumskurvenanalyse durchfhren, sondern auch mittels einiger einfacher Schritte die quivalentbreiten der Absorptionen in den Sternspektren bestimmen.

Am Ende dieser Arbeit werden zwei Objekte (namentlich P CYGNI und V1405 CAS) von besonderem Interesse nher im Detail diskutiert.

3 Introduction

Experience tells us that our universe is an empty place which it, indeed, almost is. However, the space among the stars in our galaxy, as well as in other galaxies is not as empty as it might seem at the first glance. Since most of the matter that lies among the stars is too dim to be seen by early astronomers, it took a long time until the existence of the interstellar medium (ISM) has been discovered through absorption-spectroscopic observations. In observational data from the winters of 1902/1903 [5] JOHANNES FRANZ HARTMANN found evidence that there must be some kind of absorbent in the line of sight of the double star system δ Orionis, which is the westernmost star of the Orion belt. As he observed this very star system further in detail with the GREAT REFRACTOR in Potsdam, he noticed varying Doppler shifts of the respective stellar absorption features over a few days. Prior to HARTMANN'S observation, the French astronomer HENRI-ALEXANDRE DESLANDRES discovered periodical oscillations in the spectrum of δ ORIONIS, suggesting it to be a multiple star system with components orbiting their barycenter within a couple of days. DESLANDRES calculated the period to roughly two days [17], while HARTMANN in his observations corrected it to 5.7327 days on the basis of his observation results. [17].

An observer on Earth measures a modulation in the radial velocity of the star system constituents. Thus, also the Doppler shift, which can be determined through evaluation of high-resolution spectra, changes over time. HARTMANN took spectra during many nights, compared the respective Doppler shifts, and discovered that some absorption features, well-known to originate from the stellar atmospheres of hot stars, indeed fulfilled the expectation of shifting during one orbital period. Interestingly, some absorption could be found, unaffected by this movement. In his experiment, HARTMANN focused on the Ca II lines which remained stationary over time and exhibit, unlike the stellar absorption, very narrow line widths. Since they apparently cannot be involved in the dynamics of the system, they must be caused by something else along the line of sight to the stellar system. It turned out to be the ISM, causing these spectral features.

In the scope of this thesis, we aim to survey a couple of stars, likely to exhibit ISM absorption in their spectra. We will cover the whole observation process from its very beginning, to the final results with particular interest to the planning-, observational-, and data reduction processes in detail to demonstrate where we take crucial steps in between.

4 Theoretical Background

4.1 Central Idea

Almost all the material that our world consists of, leaves a specific spectral fingerprint since its atomic and molecular material's structure determines and forms its energetic transitions. By identifying the characteristics in the respective spectra, we can find out the absorbent's composition. In our case: The composition of the ISM.

The leading idea is to perform a cosmic-scale absorption experiment, that, in principle, is very similar to an experiment that also could be done in a lab. Here, a background illumination source provides us a continuous spectrum in first-order approximation. The space between the observer and the source of light now is filled with ISM¹, leading to absorption at specific wavelengths, which we are about to observe and interpret.

The following chapters should give us an overview of the basics, to provide us a better understanding of essential concepts, eventually leading to our final results.

4.2 Phases of the ISM

The ISM defines the diffuse part of our Milky Way. It consists of both gas and dust, where the gas can form multiple phases. They all can be characterized with respect to certain quantities like the particle density n , the *kinetic temperature* T_{kin} ², and ionization levels of the respective ISM species.

Values for particle densities, n , cover a broad range of roughly ($10^{-3} \sim 10^4$) particles/cm³ [33, p. 54]. However, all of these particle densities are negligible in comparison to what we are used to on Earth: In the lower layers of our atmosphere, the particle density is 10^{22} times larger [33, p. 54]. The idea to treat the gaseous state of the ISM as an ideal gas, therefore, seems legit. With this assumption, we can formulate the very simple equation of state for an ideal gas, simultaneously defining the thermal pressure p

$$p = nk_{\text{B}}T_{\text{kin}}. \quad (1)$$

We just discussed, how low the particle densities are, we deal with. In fact, they are not even high enough to let the particles reach their thermodynamic equilibrium, in a sense, that the particles, and their energy level populations do not satisfy the *Boltzmann distribution*. It is, therefore, hard to define a strict temperature scale, as defined by the *Boltzmann statistic*. We rather stick to the kinetic temperature T_{kin} which can be defined from classical thermodynamics with the help of the average kinetic energy per particle

$$\frac{m}{2} \langle v^2 \rangle = \langle E_{\text{kin}} \rangle := \frac{f}{2} k_{\text{B}} T_{\text{kin}},$$

where f denotes the count of degrees of freedom. Therefore, for a point-like particle, we get $f = 3$. [42, p. 306]

Even though the thermodynamic equilibrium in the interstellar gas is not reached, the particle's velocities follow a *Maxwell-Boltzmann distribution*. Interestingly, we could measure $\langle v^2 \rangle$ through spectroscopy, since for a Maxwell-Boltzmann distribution, the scattering of the particle's velocities along a line of sight shapes a Gaussian. The Doppler equation finally enables us to define the relationship between the particle's velocities and spectroscopy, so that we could measure the ISM's temperature indirectly by evaluating the Doppler parameter b as an indicator for the Doppler Broadening of the respective spectral features.

In general, the ISM's thermal pressure p as it is defined by equation (1) is believed to be almost equal everywhere. Such pressure equality is also the criterion for two adjacent *phases* of the ISM

¹If we compared this to the small-scale lab experiment, it would represent the chamber with the absorbent.

²In the ongoing text we might denote the kinetic temperature more general as T , but the meaning stays the same

to coexist so that none of them would repress one another. [42, p. 307]. Accounting for only this condition, the transition between two phases would be fluent since only the product of particle density and kinetic temperature is constrained to a certain value, but not the quantities themselves. However, for an arbitrary phase of the ISM to remain stable, it also must maintain its thermal stability.

Stable phases always form in environments where heating and cooling processes balance each other. The radiation field of stars in the vicinity may ionize the ISM particles, whereas they can cool themselves down at the same time, through collisional relaxation or de-excitation processes. Nevertheless, the cooling efficiency is strongly dependent on the environment temperature T , only enabling certain temperature intervals, where this thermostat can balance itself.

We eventually identify these regions as the different phases of the ISM and distinguish them with respect to T , n , and the ionization level. The following chart lists a couple of the phases along with some characteristic numbers.

Table 1: This table lists and distinguishes between the most important and fundamental phases of the ISM. The data has been taken from [33, p. 55].

Gas Phase	Particle Density	Temperature	Distribution
	$n/ [\text{particles cm}^{-3}]$	$T/ [\text{K}]$	
cold, molecular	$100 \sim 10^6$	$10 \sim 30$	clumpy, part of the inner disk
cold, neutral	$10 \sim 100$	$30 \sim 200$	filaments within the galactic disk
warm, neutral	$1 \sim 10$	$6000 \sim 10^4$	diffuse, within the galactic disk
warm, ionized	$0.01 \sim 1$	~ 8000	wind-blown ionized bubbles (gal. disk)
hot, ionized	$10^{-4} \sim 0.01$	$10^5 \sim 10^7$	diffuse, with in the galactic halo

In addition to the gas phase, some species also condense into macroscopic dust grains, making them, unfortunately, harder to detect, since the large group of atoms enables the particles to relax in a thermodynamic meaning. This makes them rather emit and absorb like black bodies in first-order approximation [42, p. 307].

Also, neutral sodium goes through this process, so that we can only detect a certain fraction of it, still remaining in the gas phase. However, thanks to its exceptionally large oscillator strength, with spectroscopic observations, we have a very sensitive tool to detect minute abundances of neutral sodium in interstellar space.

The last point to cover here is the ionization state of the respective elements. Referring to table (1), we can see how the ISM becomes more and more ionized the higher the temperatures are. Since sodium only shows transitions within the optical part of the electromagnetic spectrum in its neutral state, we are constrained to observe only the coldest of the ISM's phases.

Taking all together, occurrences of the ISM can form a variety of different structures in our Milky Way, depending on its local abundances and shapes. Some of them are even visible to the unaided eye.

4.3 Components of the ISM

The ISM itself comes in many different appearances, of which we want to mention only a few. Scattered over the celestial sphere, many regions of dense ISM can be found, of which some glow in the red light of $\text{H}\alpha$ emission, whereas some others just scatter the incoming star's light, and again others only are made visible through their absorption of light.

4.3.1 H II Regions

As the name suggests, the hydrogen in these regions is mainly ionized, therefore, belonging to the warm, and ionized ISM according to table (1). The ionization sources primarily are hot O-type and B-type stars, usually well-positioned in the center of such regions. Protons recombine with free electrons, which causes them to radiate light in particular wavelengths, allowed by the quantum states within the atom. Because hydrogen is so abundant in the ISM, these emission nebulae emit strongly in the Lyman and Balmer series. Among all hydrogen series, the Balmer series is the only one that falls mainly in the optical part of the spectrum³. Therefore, from visual observations, we usually find strong emissions at these specific wavelengths.

H II regions form an essential part of the cosmic matter cycle. Here, stars emerge from great clouds of gas, exceeding the jeans mass, which makes them collapse under their self-gravitational attraction. This leads to the formation of hot, newborn stars. In their inner regions, the stars produce the elements we are all made of and produce heavy elements like carbon, oxygen, or nitrogen through nucleosynthesis. Stars contribute their material at the end of their life, as they, sometimes violently, eject their shells when they die as supernovae or planetary nebulae.



(a) The Great Orion Nebula (Messier 42) is a glorious example of an active stellar nursery. Here, stars form as the gas collapses. In the inner part we can make out (the most luminous) stars, responsible for the nebula's excitation: The trapezium cluster, with its brightest star θ^1 Ori C. Additionally, it is a great example for the ISM exhibiting some of the phases, coexisting here. While the core of the nebula is bright and highly ionized, the outermost, and darker regions are only made visible through the scattering of starlight. This image was taken with an 8" Ritchey-Chrétien telescope on the 02./03.03.2021



(b) Another example of a very large H II region: NGC 604 (to be found at the bottom left of the image). Among many, it is one of the red spots floating within the galactic disk of its host galaxy: The Triangulum Galaxy (Messier 33). From this perspective, one can see, at least for this projection, how these H II regions are well positioned along the galactic spiral arms. The image was taken at the OST with the CDK20 on the 22/23.09.2020

Figure 4.1: Two examples of H II regions. In these color images, one can clearly see how the dominant $H\alpha$ emission causes the nebulae's characteristic reddish glow.

H II regions form predominantly in areas with high ISM density. These usually lie within the dusty regions within the galactic plane. Therefore, we can find most of these emission nebulae at comparably low galactic latitudes.

³Of course this is only the case for sufficiently small cosmic red shifts $z \approx 0$.

4.3.2 Reflection Nebula



Figure 4.2: Crop of the famous Pleiades open cluster in the constellation Taurus with the bright star Merope centered in the field of view. The stars are embedded in a faint and blueish nebulosity. The nebula does not glow on its own. Instead, it just reflects the photons, coming from the bright cluster members. The image was taken on 16.01.2020 utilizing a 10" newton reflector telescope.

Unlike for H II regions, here, the light is not the result of the deexcitation processes of the ISM itself. What one sees is the scattered starlight from the stars, illuminating the dust clouds around. Again, we should pay attention to the color of the respective nebulae. Usually, they appear slightly bluish-tinted, which has to do with the phenomenon of RAYLEIGH scattering. Scattering is the most efficient the closer the wavelength of the light is to the size of the dust particles. Since cosmic grains usually exhibit sizes of $\lesssim 0.3 \mu\text{m}$ [22, p. 337], blue light is scattered more easily. Vice versa, this means that if we looked directly onto a star, these blue photons were missing in the spectrum, leading to a reddened color.

In fact, this process is very familiar to us: It is the reason why our day sky appears blue, while the sun at sunrise or sunset looks heavily reddened to us.

4.3.3 Dark Clouds

Dark clouds are regions containing high-density, cold ISM⁴, leading to a high optical depth and, therefore, to an especially large opacity as the dense ISM absorbs most of the light, coming from the background stars. Hence, we can only make their silhouettes visible as the cloud itself exhibits itself as a rather starless region in the sky. These clouds can be found, just like the other forms of nebulae, in the vicinity of the galactic disk. They are highly abundant in galaxies like our Milky Way. Referring to the image of Messier 33 (4.1b), we can identify the large-scale dust structures along the galactic spiral arms, where also most of the dust lies. Since our solar system is well-positioned in one of the Milky Ways spiral arms, we can expect the ISM dust clouds to exist in every direction, just with different opacities.

4.4 Extinction and Reddening

A phenomenon, often to be found in the same context as ISM, is the extinction of light. It describes the process of light getting scattered and absorbed by a medium (like in our case the ISM) between an observational subject and the observer.

First, let us focus on the process of RAYLEIGH scattering:

As the light gets scattered, it is deflected into random directions. The photon's probability of getting coincidentally re-emitted towards us is negligible, since we, as the observer, cover only a tiny, truly unimportant fraction on the whole unit sphere, light years away. Therefore, from our

⁴As we recall table (1), these clouds can be either mainly made out of neutral atoms in their gas phase, or if the low temperatures permit, even molecules.

perspective, it seems like the light is *missing* from the initial flux, originating from the source, as it will propagate into different directions after the scattering process.

By nature, the effectiveness of this scattering process depends on the wavelength λ . The same material, therefore, takes away more light in specific wavelength regions. Theory shows, the effectiveness of RAYLEIGH scattering maximizes for particles with the same size as the wavelength of the respective light. ISM dust grains usually are not larger than $\lesssim 0.3 \mu\text{m}$ [22, p. 337], leading to increased effectiveness for scattering towards the UV. The *extinction curve* (see figure (4.3)) is a descriptive correlation, plotting the extinction of light as a function of wavelength, also visualizing the phenomenon, we just mentioned.

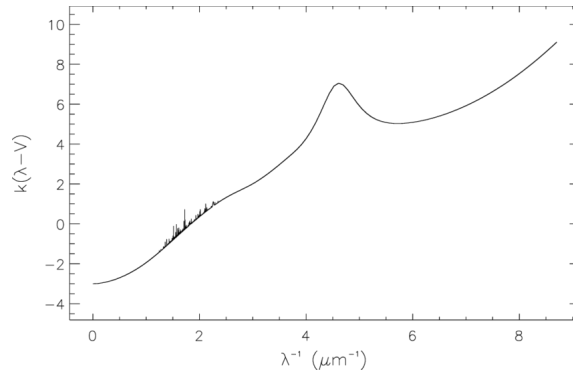


Figure 4.3: The averaged extinction curve for the galactic plane, extracted from a conference paper, is given with source [28, p. 329]. $k(\lambda - V)$ is defined as the extinction $E(\lambda - V)/E(B - V)$, normalized to the $B - V$ extinction. The bump in the UV (at $\lambda \sim 2175 \text{ \AA}$) is believed to result from organic molecules present in the galactic plane, whereas the noise-like features in the visible range, predominantly represent discretely, but yet unidentified absorption features. [28, p. 327]

We can see in figure (4.3) how the extinction rises towards smaller wavelengths, at least in first-order approximation in the optical range. This is the consequence that scattering of *optical* photons is rather effective for blue ones. The remaining optical light, hence, is dominated by red light. Because of its outcome, this process is also known as *reddening*.

In this regard, we have to keep in mind that RAYLEIGH scattering *re-shapes* the whole spectrum and is not constraint to a single wavelength, because it is a process, not having its origin in the quantum mechanical regime. The atom and molecule absorption, which we can see in the absorption spectra later, refer to a separated process here. However, a basic understanding of the formation of those absorption lines is required, since we will only make use of discrete absorption processes in our observations as we observe stellar absorption lines, not focusing on large-scale spectral structures, like the continuum's shape itself.

4.5 Absorption Line Profiles

Indeed, in absorption spectroscopy, we deal with a lot of absorption lines. It is, therefore, crucial to understand the concepts of how these absorption features form, and how to interpret their shape.

Absorption profiles can get very complicated as we can see in figure (4.4), presenting a set of Na I absorption lines, we detected during our observations.

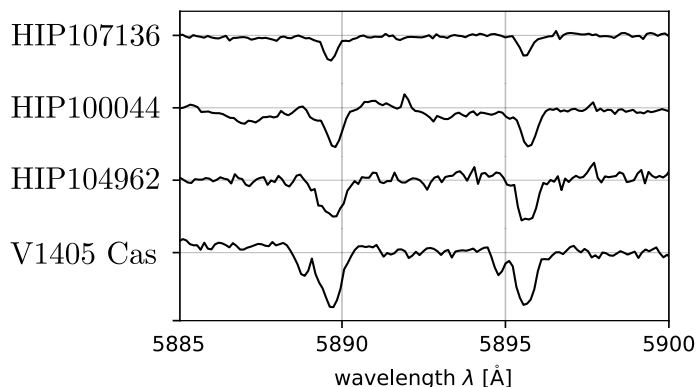


Figure 4.4: In this figure, we can see a stack of absorption spectra covering the spectral range of the sodium doublet and exhibiting unique features for different stars. All spectra represent data that we acquired in the scope of this thesis. One can see, how all line shapes differ with respect to their intensity profile.

In fact, they are, even in the most general case, more complex than just a Gaussian or a Lorentzian, solely. As we will see later, even two or more independent clouds absorbing light may cause the resulting absorption features to blend, and form a truly complex line pattern (like it can be seen in figure (10.2) as part of the data discussion in the end, for instance).

To still enable us reasonable interpretations in as many cases as possible, we must discuss how different phenomena are affecting the absorption line's shapes.

Of course, this all is only possible if we understand the most fundamental principles behind that.

4.5.1 Natural Line Width

Every quantum mechanical transition between the upper energy level k , and the lower ground state level i comes with a certain lifetime. This phenomenon is due to the quantum mechanical oscillator model, and Heisenberg's uncertainty principle. It states that one can know *either* the energy *or* time precisely. Therefore, every spectral line (referring to two levels of energy) comes with a definite natural line width. The absorption profile, caused by the natural broadening, furthermore, follows a Lorentzian profile [22, p. 107], which can be written in the following way:

$$L_\nu(\nu) d\nu = \frac{\Gamma d\nu}{4\pi^2 (\nu - \nu_0)^2 + \Gamma^2/4} .$$

Here, Γ is the damping coefficient, corresponding to the quantum state's lifetime. Furthermore, ν_0 names the center frequency of the transition. The half-width at half maximum can be expressed through

$$\nu_{1/2} = \frac{\Gamma}{4\pi} ,$$

which is usually less than a single mÅ for allowed quantum mechanical transitions. Given the central frequency of the transition ν_0 , we can convert the distribution's abscissa into a wavelength, yielding us

$$L_\lambda(\lambda) = \frac{\Gamma_\lambda}{\Gamma_\lambda^2 + (\lambda - \lambda_0)^2} \quad (2)$$

with the respective Γ value, converted into the wavelength frame $\Gamma_\lambda = \Gamma\lambda^2/c$.

We later will see that the effect of natural broadening is, in general, several magnitudes smaller than thermal Doppler broadening, which we are just about to discuss in the following paragraph.

4.5.2 Thermal Doppler Broadening

From classical thermodynamics we know, particles, forming a medium in its thermal equilibrium state, follow a Maxwellian velocity statistic. Therefore, their intrinsically randomized velocity vectors exhibit a Gaussian distribution along any line of sight. Assuming the transition would take place at a very certain frequency ν_0 (i.e. specific wavelength λ_0), we would observe a thermally Doppler broadened line as many of the particles contribute to the flux of the absorption (or emission, respectively). The velocity profile of the transition could be described as a Maxwell-Boltzmann velocity distribution in the following way

$$G_v(v) dv = \frac{1}{\sqrt{\pi}b} e^{-\frac{v^2}{b^2}} dv \quad (3)$$

with the physical interpretation of b as

$$b = \sqrt{\frac{2k_{\text{B}}T}{m}},$$

also referred to as the so-called Doppler Parameter.

Just like $L_v(v)$, $G_v(v)$ is normalized through its pre-factor $1/\sqrt{\pi}b$ and describes a *probability distribution*, telling us how likely it is to observe a moving particle in the velocity interval $[v, v + dv]$, but not an absolute absorption or emission intensity.

4.5.3 Other Doppler Broadening Effects

In addition to the effects we just mentioned, causing the spectral lines to smear out to some scale, there are far more other phenomena, leading the stellar absorption lines to blur.

We distinguish between *large-scale* motions and *small-scale* chaotic motions. The latter one can be described as Gaussians in good approximation according to [32, p. 7], whereas large scale motion, such as the stellar rotational broadening, causes other line shapes. Luckily, this easy-to-model local velocity dispersion commonly plays the dominant role, and is, therefore, treated predominantly in the discussion of the ISM's absorption line shapes later in the discussion part.

4.5.4 The Voigt Line Profile

As mentioned in the chapters before, there are many effects, having an impact on the shape of the spectral intensity profiles. The *Voigt profile* describes a superposition of the Gaussian G_λ and the Lorentzian L_λ , as the curve arises from the convolution of both.

$$\phi_\lambda(\lambda; b, \Gamma) = G_v(v; b) * L_\lambda(v; \Gamma) \quad (4)$$

A convolution of two distributions (if they are normalized) *always* represents the floating mean, weighted with respect to a given distribution. In this very context, it would be the Gaussian velocity distribution $G_v(v; b)$ averaged over the intrinsic natural broadening $L_\lambda(v; \Gamma)$ of every emitting species at any point on the Gaussian. Applying equation (4), and inserting the transformed distributions (2) and (3), leads to the following integral expression, that we need to evaluate.

$$\phi_\lambda(\lambda) = \int_{-\infty}^{\infty} \frac{\Gamma_\lambda}{\sqrt{\pi}b} \cdot \frac{e^{-\frac{v^2}{b^2}} dv}{\Gamma_\lambda^2 + [\lambda - \lambda_0 (1 + \frac{v}{c})]^2} \quad (5)$$

In the upper formula, we can see how we shift the natural broadening distribution, following the Lorentzian, through the space of velocities, and convolve it with the Gaussian, utilizing the non-relativistic Doppler equation.

Since we cannot solve the upper integral by analytic means, we must proceed numerically from this point. Therefore, we are particularly interested in reducing the size of the formula and re-scale

the velocity scale onto a unitless quantity. For this purpose, we introduce the two parameters α and y both defined as follows:

$$\alpha(\lambda) = \frac{\lambda_0 \Gamma}{b} = \frac{c \lambda_0 \Gamma_\lambda}{b \lambda^2}$$

$$y = \frac{v}{b} .$$

Hence, easing equation (5):

$$\phi_\lambda(\lambda) = \int_{-\infty}^{\infty} \frac{1}{\sqrt{\pi} b} \cdot \frac{\alpha e^{-y^2} dy}{\alpha^2 + (v - y)^2} .$$

Since we integrate over the velocity space, the result becomes independent of the velocity v . The absorption profile in this frame becomes a function of wavelength (or energy, frequency, respectively). For an arbitrary set of parameters, the curve shape is shown in figure (4.5).

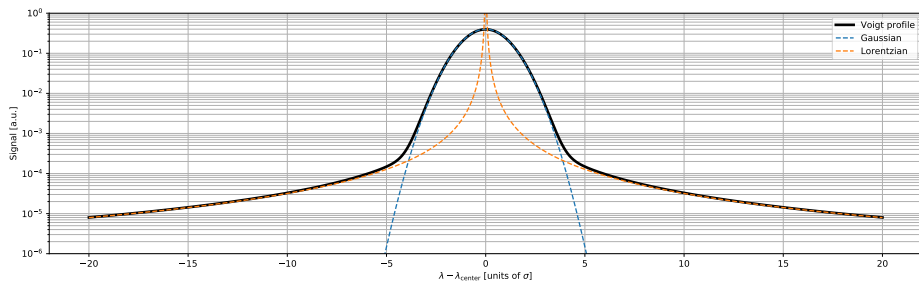


Figure 4.5: The logarithmic y -axis scaling allows us to see how there are two regimes within the Voigt profile. One can make out the Gaussian-like Doppler broadened core with rapid fall-off to the sides. Furthermore, we can see the Lorentzian wings on the very edges, gaining importance beyond the, in this very case, 5σ limit. Again, this emphasizes, how the natural line broadening only plays a role for truly strong absorption lines. For this example we chose $\gamma = \sigma/10$.

What we can learn from the upper figures is that Voigt profiles usually exhibit a Gaussian-dominated core, whereas the profile's wings are dominated by the Lorentzian. This concept plays an important role as one moves forward to the *curve of growth*, discussed in chapter 4.5.6.

4.5.5 Equivalent Width

The equivalent width W_λ is a useful measure to characterize the normalized strength of absorption features. It is primarily defined for absorption features in the following way

$$W_\lambda = \int_0^\infty d\lambda \left(1 - \frac{I_\lambda(\lambda)}{I_C(\lambda)} \right) , \quad (6)$$

where I_λ is the intensity at wavelength λ , and I_C the continuum signal. Of course W_λ can also be converted into a frequency frame, denoted as W_ν respectively, and vice versa. The easy conversion becomes $W_\lambda = \lambda^2/c \cdot W_\nu$.

Generally spoken, the higher the value of W_λ , and W_ν respectively, is, the stronger the absorption takes place. The advantage of the equivalent width: Thanks to the integral within its definition, only the area i.e. the flux's "missing" part matters, regardless of the actual absorption profile itself. The spectra we observe are always a convolution of the actual signal, emitted by the star, and the instrument's intrinsic broadening function like a Gaussian, for instance. The equivalent width is a conserved quantity to a convolution, making it a neat number to characterize the absorption strength. Figure (4.6) should demonstrate, how the equivalent width is independent on the actual

absorption line profile. Although all curves exhibit different shapes, they all cut the same area out of the normalized continuum, i.e. the equivalent width is equal for all of them.

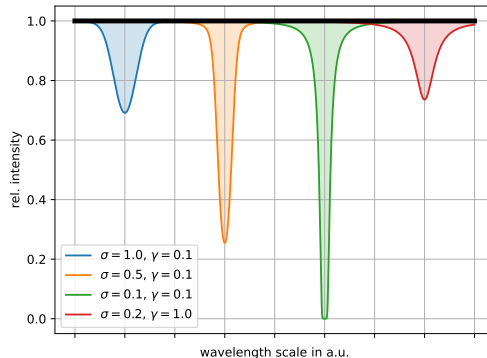


Figure 4.6: Comparison of four absorption line profiles. Note their different shapes, but equal W_λ values. The latter we conclude from the equally shaded regions under these curves.

4.5.6 Computation of Column Densities

In the previous chapter, we coarsely introduced the equivalent width W_λ as an important observational quantity. As we take a step further, we are interested in the respective column densities N . This quantity is rather obtained by theoretical models. We try to reconstruct what amount of absorbent per unit area it would need to absorb the lacking amount of light, we see within the absorption spectra.

As light with intensity I_0 travels through a thin (with thickness dr) sheet of absorbing material, some photons may get absorbed and emitted in a direction that differs from the initial one. Hence, they are not being observed, as they do not go through the aperture of our telescope anymore. Let us assume a certain, and fixed amount dI of light gets redirected on its way through the material per unit of length within the absorbent/emittent. The resulting intensity then can be determined with the *radiation transfer equation* [11, p. 8],

$$dI(r) = -I(r) \kappa(r) dr + \epsilon(r) dr ,$$

where κ describes the absorption’s “efficiency” per unit length, and ϵ the emittance’s one. Since the probability, of some atoms in the ISM to re-emit directly towards Earth is negligible, we can move forward, and approximate $\epsilon(r) \approx 0$. Therefore, the radiation transfer equation eases and becomes a differential equation at its easiest with the exponential as its solution

$$dI(r) = -I(r) \kappa dr \iff \frac{dI(r)}{I(r)} \equiv (\ln I(r))' = -\kappa(r) dr \iff I(r) = e^{-\int_0^d \kappa(r) dr} .$$

Here, we integrate along the way from the observer up to the distance where we can the observational subject. Furthermore, we introduce a new quantity here: The *optical depth* τ , defined as the integral in the exponent [11, p. 8]

$$\tau := \int_0^d \kappa(r) dr . \quad (7)$$

Here, we can see how τ emerges from the integration over infinitesimal thin layers of absorbent, regardless of their actual distance r in first-order approximation. Hence, it does not matter, whether the absorbing clump of ISM material lays in the far distance or closer to the observer. Not even the spatial distribution of it is relevant as long as the integral is fixed. This concept will lead us to the idea of the column density very soon.

Given the distance d to the background illumination source, we can merely calculate the *mean* volumetric particle density \bar{n} along the line of sight up the star's distance.

The very fundamental problem is that we sum up and project all absorbent particles along the respective line of sight, and, therefore, lose a geometric dimension.

Because of this, we cannot describe the ISM's density like a function of distance, without further, extensive observations. However, in the scope of this thesis, we are not interested in the particular three-dimensional ISM distribution. This allows us to now *define* another important quantity, which we already used earlier in this context, from its first principle: The *column density*

$$N := \int_0^d n(r) dr, \quad (8)$$

where n denotes the classic particle density, given as particles per unit volume. N yields information about how many particles per unit area are stacked on top of each other. It can be derived from theoretical models, taking the observed equivalent width into account. Let us think about the absorbents as quantum mechanical oscillators being excited with a certain efficiency. Intuitively, τ is proportional to the amount of material-presence in the ISM. Hence, the optical depth τ can be written as a product of some absorption efficiency coefficient a , we assume not being dependent on the r -coordinate, and the column density N

$$\tau_\nu(\nu) = \int_0^d a_\nu(\nu) \cdot n(r) dr \stackrel{(8)}{=} aN.$$

The subscript ν in τ_ν and a_ν refers to the frequency scale, since both parameters depend on frequency, and change in their units or values according to the abscissa's unit (either wavelength λ or frequency ν in general). In the general case, we can re-formulate both, so they become functions of wavelength λ . In a further step, we can insert the upper result into the equivalent width's definition (see equation (6))

$$W_\lambda = \frac{\lambda^2}{c} W_\nu = \frac{\lambda^2}{c} \int_0^\infty (1 - e^{-\tau_\nu}) d\nu = \frac{\lambda^2}{c} \int_0^\infty (1 - e^{-a_\nu N}) d\nu; \quad (9)$$

a_ν is an agglomerate of natural constants, as well as the broadening function, as introduced in chapter 4.5.4.

$$a_\nu = \frac{\pi e_0^2}{m_e c} f_{lu} \phi_\nu N$$

where we stick to the following notation:

e_0	the elementary charge,
m_e	the electron mass,
c	the speed of light,
N	the column density,
f_{lu}	the oscillator strength between state l and u , as well as
ϕ_ν	the absorption profile on the frequency scale.

Graphically said, the connection between both quantities is the so-called *curve of growth*, linking observational and physical quantities in a plot.

As we can see, the integral definition for W_λ , in general, is highly non-trivial, and can not be calculated analytically. In addition to that, it also requires integration over two dimensions⁵. However, there are different regimes in which we can approximate this integral, making it a little easier to handle.

⁵One, for the evaluation of the Voigt profile itself, and one another to sum up all exponents of the optical depth along the wavelength or frequency scale, respectively.

4.5.7 Saturated vs. Non-Saturated Features

In the most recent chapter, we have seen that the process of obtaining the equivalent widths from absorption profiles can be tricky. Indeed, there is an analytical approach for this problem by introducing different regimes on the curve of growth. In each, we can make some approximations. We distinguish between *non-saturated* and *saturated* and *damped* absorption lines.

For non-saturated absorption, the optical depth τ never ascends dramatically, making it possible to approximate the exponential in a first-order Taylor series $e^{-\tau} \approx 1 - \tau$. In this regime, the expression for the equivalent width eases to

$$W_\lambda = \int_0^\infty \frac{\pi e_0^2 \lambda^2 N f_{lu} \phi_\nu}{m_e c^2} d\nu .$$

The result of this equation is the fact that the equivalent width W_λ is directly proportional to the column density N . Here, all quantities are constants, with the exception of ϕ_ν merely describing the *normalized* distribution. As we, therefore, can conclude:

$$W_\lambda \propto N .$$

As we approach values for τ large enough, we leave this linear regime and enter the region, where the saturation of these lines plays a significant role:

As we double the column density, for instance, we do not multiply the equivalent width with two anymore. Instead, this value increases *more slowly*, since the line intensity minimum can not decent below zero flux, leading the intensity at a minimum wavelength to converge towards zero. The absorption feature's nose⁶ flattens out somewhat (see figure (4.7) for visualization), resulting in a rather boxed-shaped intensity minimum. We entered the regime of *saturated* absorption lines. If we did not take this into account, we would severely underestimate the respective column densities. In this regime, the curve of growth, therefore, flattens drastically. Mathematics show, here, the equivalent with W_λ is proportional to the column density in good approximation

$$W_\lambda \propto \sqrt{\ln N} .$$

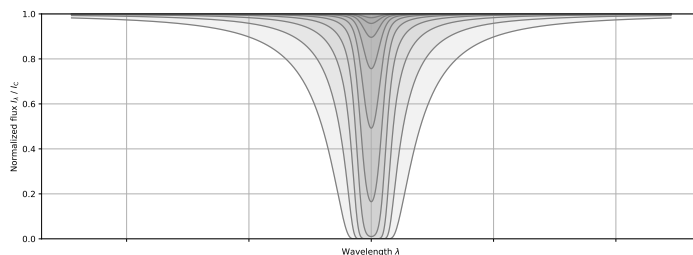


Figure 4.7: Comparison between intensity profiles assuming Voigt absorption profiles. The shape of all ϕ_λ stays the same, but different column densities N are probed through.

In the regime of *damped* absorption lines, we can approximate the integral, given in equation (9), in another way. For extraordinary strong absorption, the profile flattens out in a way, that also the descending Lorentz wings on both sides gain importance. We can figure this in the most recent plot in figure (4.7). In this regime, the equivalent W_λ with is proportional to the column density's square root $W_\lambda \propto \sqrt{N}$.

Taking all three regimes together, we can print the curve of growth for those. For a specific equivalent width, we can retrieve the respective column density (and vice versa) for a specific

⁶namely the Gaussian Doppler-broadened absorption core

material this way. An exemplary plot, assuming a Voigt profile, like it would be the result of equation (4), can be found in figure (4.8) for the Na I D-line transition and different Doppler parameters b .

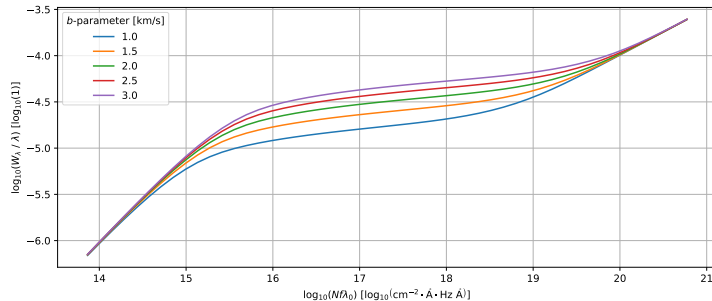


Figure 4.8: Curves of growth, visualizing the three different regimes. Both axes are scaled logarithmically so that we can identify the proportionality in the respective regimes. For the so-called *curve of growth analysis*, usually, one plots the relative equivalent width W_λ/λ over the product of $N f_{lu} \lambda$. The different lines emerge from Doppler parameters b , assumed differently for every curve. Thanks to the calculation rules for logarithms, we can split the product $\log N f_{lu} \lambda = \log N + \log f_{lu} \lambda$. The advantage of this: We can (horizontally) shift the curves of growth accordingly to make them match our data point as well as possible. Both, f_{lu} and λ , are naturally fixed quantities. Therefore, allowing us to change the column densities N only. This example plot was created with the help of the python program PySPAN, which enables us to perform the curve of growth analysis in our observations. We will further comment on its working principle in the chapters 4.5.6 and 12.2.

The saturation of absorption lines is a crucial issue when it comes to the interpretation of ISM equivalent widths and their conversion into column densities. Since its absorption usually exhibits extraordinary narrow features, our setup could not provide us the necessary resolution to identify such saturated line profiles. The problem is that even though a line might be saturated, it appears not to be. They would smear out that even in the flux minimum, as, due to the non-sufficient spectral resolution, some light from adjacent wavelengths contributes to the flux, flattening the line profile. We, therefore, could misinterpret an already saturated (or even damped) line as an unsaturated one, potentially causing misleading results during the conversion from equivalent widths W_λ into column densities N . We see that we must make use of another method to identify and treat saturated ISM absorption features.

In our specific case here, we take advantage of the fact that the Na I doublet consists of two absorption lines with absorption strengths, being intrinsically different. In fact, Na I $\lambda 5890$ (FRAUNHOFER D₂ line) has roughly double the strength of the Na I $\lambda 5896$ (FRAUNHOFER D₁ line) line. According to the curve of growth, this results in respective equivalent widths. Evaluating the ratio of these also may hint us towards certain saturation regimes, in consequence, leading us to a specific column density N . Again, we want to emphasize that the lack of flux due to the absorption is a conserved quantity, even with low-resolution spectrometers.

We get an idea of how this ratio looks like for the three regimes in the end, as we assume certain parameters and probe through a wide range of column densities N . Figure (4.9) illustrates the progression of the Na I D line equivalent width ratios $W_{\lambda, D2}/W_{\lambda, D1}$ with varying column density N .

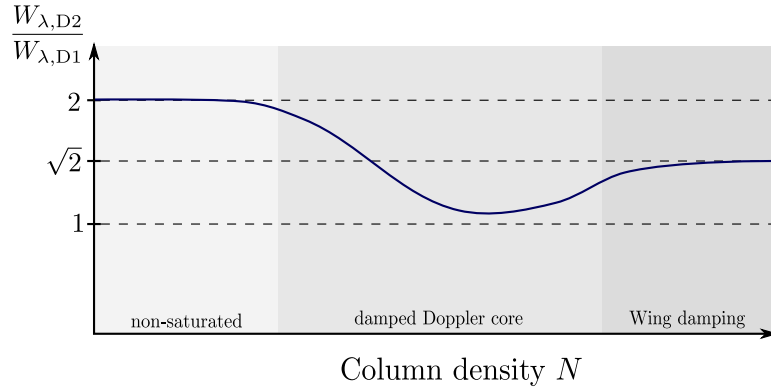


Figure 4.9: A derived “curve of growth”, correlating the mentioned ratio of the sodium equivalent widths $W_{\lambda,D2}/W_{\lambda,D1}$ and the column densities N .

4.5.8 Mean Particle Densities

In equation (8) we introduced the classic particle density n as a quantity, telling us the number of particles per unit volume. Through its definition, we can evaluate the mean particle density if we know the distance and the column density if ISM sodium for a respective star as follows

$$\frac{N}{d} = \frac{1}{d} \int_0^d n(r) dr =: \bar{n} .$$

The formula looks quite similar to what we have seen in equation (8). In fact, if we divide the column density by the star’s distance, we obtain the definition of the, with respect to the distance, averaged particle density itself.

Using data from the Gaia satellite, one usually finds the parallaxes p , with which we can deduce the distance making use simple geometry. Therefore

$$R = d(p) \cdot \tan p .$$

Here, R represents the baseline and d the object’s distance. Since R is fixed for all products, $d \tan p$ must be equal as well. Hence, one can apply the definition of 1 parsec as follows

$$d_0 \tan \pi_0 := 1 \text{ pc} \cdot \tan(1 \text{ arcsec}) \stackrel{*}{\approx} 1 \text{ pc arcsec} \stackrel{!}{=} d(p) \cdot p \iff \frac{d}{\text{pc}} = \left(\frac{p}{\text{arcsec}} \right)^{-1}$$

For *, we utilize the small angle approximation, since parallaxes are usually of magnitude of only a few milliarcseconds (mas). Especially for Gaia data, yielding us parallaxes in this unit, a minutely derived form of the upper equation helps us to convert parallaxes into distances

$$\frac{d}{\text{kpc}} = \left(\frac{p}{\text{mas}} \right)^{-1}$$

Finally, making the conversion from column densities N to mean particles densities \bar{n} directly possible:

$$\left(\frac{\bar{n}}{\text{cm}^{-2} \text{ kpc}} \right) = \left(\frac{N}{\text{cm}^{-2}} \right) \cdot \left(\frac{p}{\text{mas}} \right) \implies \left(\frac{\bar{n}}{\text{cm}^{-3}} \right) \approx 3.241 \cdot 10^{-19} \cdot \left(\frac{N}{\text{cm}^{-2}} \right) \cdot \left(\frac{p}{\text{mas}} \right) \quad (10)$$

4.6 Early Type Stars

Yet, we are familiar with the characterization of absorption lines with respect to their shape and strengths. We can handle the concept of equivalent widths W_{λ} , derive quantities like column densities N , and the mean particle densities \bar{n} with the help of a curve of growth analysis.

It is now time to focus on the actual objects that are being observed in the scope of this thesis:

Hot stars, acting as the sources of illumination for our ISM absorption spectra.

4.6.1 Reference Spectra

For our observations, we focus on hot O and B stars being the illumination sources for our absorption spectra. They exhibit only a few stellar absorption lines and no lines of neutral metals, therefore, providing us an even continuum. It is due to their exceptionally high atmosphere temperatures, causing the metals in their chromosphere to get ionized. In contrast to that, as we would move to lower effective temperatures T_{eff} , neutral metals can exist in the stellar atmosphere and therefore lead to stellar metal absorption.

The following plots in figure (4.10) show reference spectra of canonical O-type and B-type stars, without ISM Na I absorption.

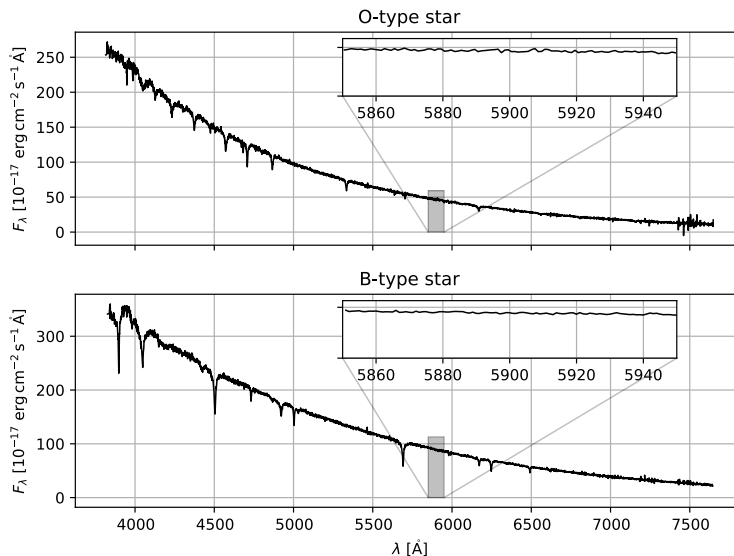


Figure 4.10: Optical spectra of early-type O and B stars. The data for this originates from the SDSS data release 5 and are cross-correlation templates for their respective spectral class. [4]

From a more detailed perspective, the following absorption lines are very characteristic for early-type stars and are also used for the classification of those:

B-type stars

These stars predominantly exhibit strong lines of neutral helium, strong Balmer lines, and lines of highly ionized metals like Si III and Si IV. Lines of neutral metals are almost entirely absent since the high surface temperatures lead to ionization processes in the respective atoms.

O-type stars

Just like B-type stars, O-type stars do not show lines of neutral metals (sodium included). Instead, the presence of ionized helium is one of the general criteria to distinguish B-type stars from O-type stars. The He II absorption strength increases towards higher temperatures, where the Balmer lines become less intense.

Therefore, we do not expect noticeable amounts of Na I, like we would in the sun's (a G-type star) spectrum. However, if we detected strong Na I absorption, it would be an indicator (not proof) for ISM presence in the line of sight towards the respective star.

Imagine a hot star having a disk or an envelope of dust around. As we looked through such a disk, it would also cause the Na I absorption in our spectra, even though the features do not originate from actual ISM among the stars.

However, with a very high-resolution spectrometer, or long-term spectroscopic monitoring, one might be able to distinguish between such stellar system-related lines, and those having their origin actually in the ISM. Indeed, if we assumed vertically (along the star's rotation axis) constrained disk of dust and gas, the ordered motion of the particles around the star would *not* form a Gaussian. At this point, we may recall that the underlying principle of such a profile is a chaotic motion of the particles, which, of course, is not the case for a disk in which the particles smoothly orbit the star in one major direction. Instead, the blending of absorption lines with different Doppler shifts would result in more complicated, and also severely broadened absorption lines.

Unless its constituent particles are not orbiting the star, a whole shell, encasing a star, must expand in order to not fall back onto the star's surface, and remain to remain stable. Indeed, such examples exist and we will even discuss two of them in detail later in chapter 10.

4.7 ISM Absorption Features

Referring to chapter 4.5, we have already discussed the principal line shapes we expect for ISM absorption.

Considering what we have discussed previously, gives us an idea of how the ISM absorption should appear in general. In summary, we expect ISM features to be exceptionally narrow and not to exhibit any dynamics over time like the stellar absorption features of the components of a binary star system would do.

Silently, we assumed the simplest situation possible: A single, structureless cloud, providing particle motions that satisfy the Maxwell-Boltzmann statistic.

In reality, the spatial geometry may be more complicated and we may look through more than one ISM cloud solely. Of course, this has fundamental consequences for the Na I absorption profiles we detect.

In this chapter, we will discuss this concrete issue.

4.7.1 Different Shapes

It applies: The greater the distance to the background star is, the deeper we are probing the ISM. If we assume that we would look through several clouds of ISM, we would identify somewhat odd line shapes.

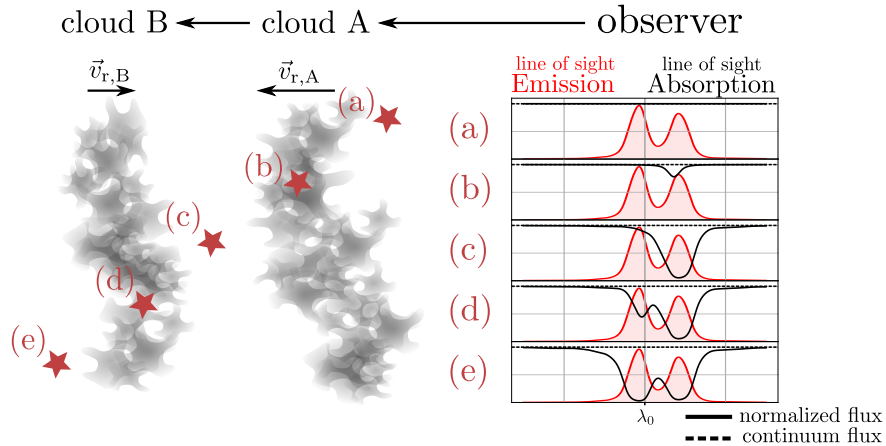


Figure 4.11: This figure illustrates how rather complex emission profiles of e.g. H I, and absorption profiles of e.g. interstellar sodium emerge with respect to the path, the light takes on its way through the ISM. The arbitrary plots show the outcome for the different illumination source's arrangements (a) to (e). We assume the clouds to move with different radial velocities $\vec{v}_{r,A} \neq \vec{v}_{r,B}$. The observer looks from the right to the left.

This is due to the superposition of two or more ISM dust clouds with different radial velocities. Therefore, also the absorption profile would form two or more peaks, according to the number of independent dust clouds with different intrinsic radial velocities⁷, through which the light passes.

4.7.2 The Na I Doublet

Even though the neutral sodium in the ISM is the reason for the strong Na I absorption in the respective spectra, it is far less abundant than other materials like hydrogen, helium, carbon, and oxygen, for example. The reason for its comparably sensitive fingerprint is its high oscillator strength.

Besides sodium, we can also find other substances like ionized calcium, which forms the remarkable Ca II doublet (also known as the Ca H and Ca K lines, discovered by JOSEPH VON FRAUNHOFER in 1814 [22, p. 227]).

Since the only valence electron left in the outermost shell of the ionized calcium has a comparably large ionization potential of 11.871719(4) eV [23], Ca II is more persistent in the ISM, comparing the ionization potential of atomic sodium with 5.13907696(25) eV [23]. UV photons traveling across an ISM cloud randomly sometimes hit atoms in the ISM, and ionize them. Therefore, the higher the ionization potential is, the harder it is to ionize the atoms. The metal abundances and their ionic forms remain always in an equilibrium state between ionization and de-ionization. One could, therefore, find always a mixture of atomic, as well as ionized sodium.

Nevertheless, sodium acts as a convenient indicator for the presence of ISM as its absorption falls in the mid-optical range of the electromagnetic spectrum. Also, it strongly indicates cold or shielded environments for the ISM, since the presence indicates the sodium to be in its ground state, not harshly excited by the surrounding radiation field.

4.8 Reference Systems

In the following chapter, we want to get familiar with some basic reference systems in the sky, considering a basic understanding of them is crucial for orientation in the sky.

⁷Different radial velocities mainly are the result of the galactic rotation, rather than of the peculiar dust cloud's motion [11, p. 52].

Since we project nearly everything, we observe in astronomy or astrophysics, on the sky, we have to define *two* perpendicular coordinates on the celestial sphere, and another, like the *distance* to the observed object one, to make space finally three-dimensional.

There exist many reference systems, but essentially, only their respective orientations differ. There are different points of interest (north celestial pole, from now NCP) or structures (like the Milky Way's galactic disk) in the sky, to which we could potentially align them.

In the ongoing text, we will refer to three different coordinate frames.

4.8.1 Equatorial Coordinate System

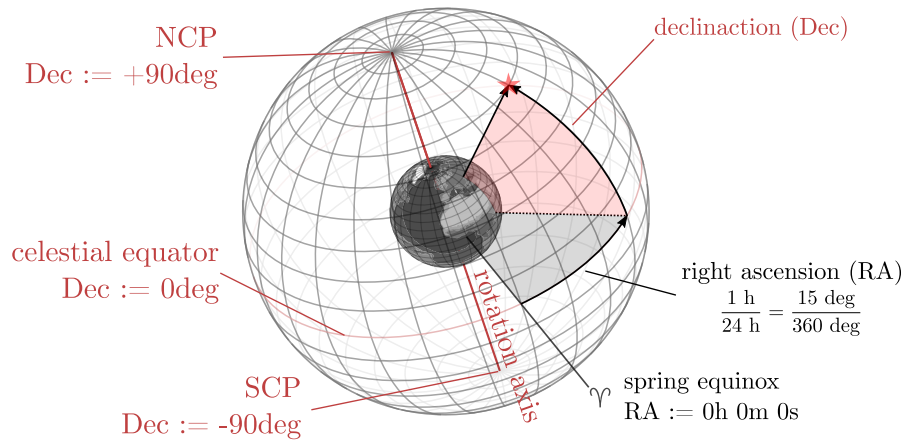


Figure 4.12: A sketch of the celestial equatorial coordinate grid as a wireframe sphere. It illustrates how the equatorial reference frame emerges from given reference directions like Earth's rotation axis and the right ascension reference point. Today, the ICRS frame is no longer constrained to the moving Earth's rotation axis anymore, but aligned to a set of distance quasars, naturally having negligible apparent motions in the sky.

The *equatorial coordinate system* forms a cartesian reference system concerning the Earth's rotation axis. It consists of two perpendicular axes, namely the *right ascension* (hereafter RA) α , and the *declination* (hereafter Dec) δ axis. Since the RA axis points toward the north celestial pole, also Earth spins rotates this axis. Because Earth spins roughly once in 24 hours, the RA value is often given as an hour angle. Here we divide the full circle, made up of 360 degrees, into 24 equal sections, each 15 degrees wide. For a finer scale, we further subdivide these intervals, analog to the scale on a clock. A typical coordinate tuple, therefore, could be looking like the following example (ICRS coordinates for the bright star Sirius⁸):

RA	06h 45m 08.91728s
Dec	-16deg 42m 58.0171s

⁸These values are retrieved from SIMBAD

4.8.2 Altitude-Azimuth Coordinate System

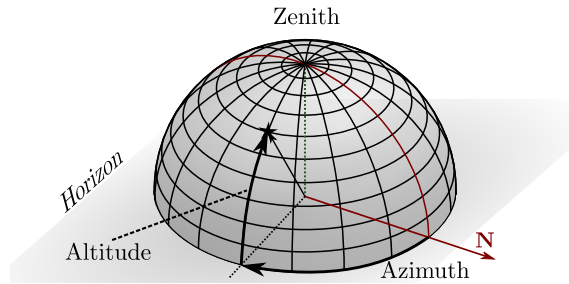


Figure 4.13: A minimalist figure to illustrate the general ideas of the altitude-azimuth coordinate system.

Object's coordinates in the altitude-azimuth (or short AltAz) coordinate system are unlike the ICRS reference frame not meant to stay fixed at all times because the coordinate frame orients itself on Earth's⁹ horizon. The altitude coordinate then tells us the angular separation of an object from the horizon. Thus, an object with altitude zero degrees would directly point toward the horizon, whereas an object with an altitude of 90 degrees pointed toward the zenith.

The second coordinate is the *azimuth angle*. It describes the direction along the horizon. Basically, it stands for the compass direction of the respective object where North gets assigned zero. The azimuth value increases eastwards.

Of course, the coordinates of an object are not fixed in this very frame, since Earth's rotation lets astronomic objects move over the sky during the night. Nevertheless, this reference frame is quite useful when it comes to the planning of observations since we can tell whether an object is potentially observable at a certain time.

The conversion from the ICRS frame into the AltAz system is somewhat tricky since we have to take many parameters into account. Not only does the geographic position on Earth matter, but also the exact observation time. Luckily, certain python routines (within the `astropy` package, for instance) can handle this conversion precisely.

Given the coordinates of the observation site, we can calculate the altitude of any object with respect to observation time. We call such a plot a *visibility plot*, referring to the time-dependency, determining whether an object is observable for us so that it stands reasonably far above the horizon. Such a visibility plot is helping a lot for planning observations.

⁹One could also generalize the idea for other horizons, but because of obvious reasons Earth's horizon is commonly used as reference. However, the same idea is also applicable for other planets or celestial bodies.

4.8.3 Galactic Coordinate System

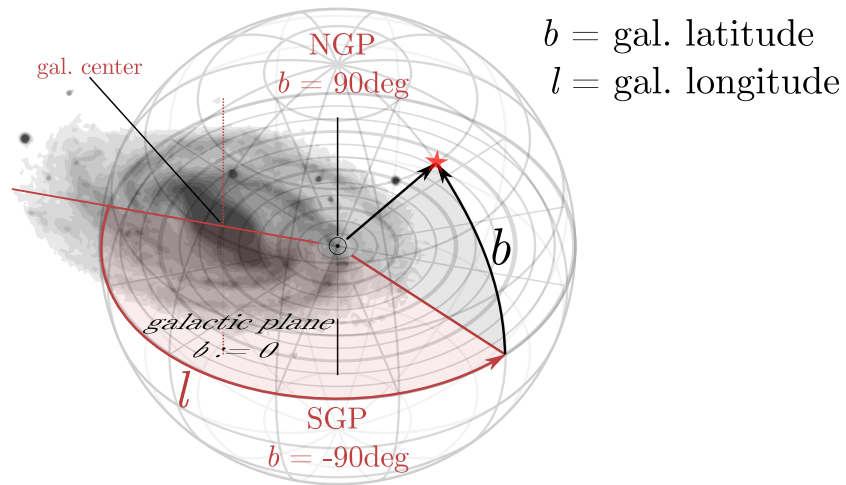


Figure 4.14: This figure depicts the orientation of the galactic coordinate frame with respect to the Milky Way galaxy.

The third reference frame we want to cover is the galactic frame. As the name suggests, it is aligned to the orientation of the Milky Way. Since our galaxy forms a band-like structure surrounding the solar system, we can define an equator along we define the *galactic longitude* l as the pendant to Earth's geographic coordinates. The reference point for this axis is the center of our Milky Way with longitude zero and with ascending longitude value eastwards. Just as we did for the equatorial reference system we define another axis perpendicular to the latter - the *galactic latitude* b . This again defines the angular distance of an object to the galactic plane (equator). Take Sirius, for example, again. Its coordinates in the galactic reference frame are given by

gal. latitude $b \approx -8.9 \text{ deg}$

gal. longitude $l \approx 227.2 \text{ deg}$

Notice the rather small galactic latitude, indicating that Sirius lies close to the band of the Milky Way.

5 Setup

The observations presented here were conducted at the OST observatory situated in Potsdam, Golm. It is part of the Institute for Physics and Astronomy of the University of Potsdam.

In the scope of this thesis, the spectroscopic observations were carried out on our own. An important part of this thesis, hence, is also the acquisition of the data from its very beginning. Regarding the setup that we used to conduct the observations, we present the OST's setup with all its crucial components in this chapter.



(a) The observatory from the outside. The image has been taken in the vicinity of building 28 (the building in golden tint)



(b) The inside of the dome with the CDK20 on top of the 10Micron mount in the center. (The image has been taken from the OST Wiki page)

Figure 5.1: Pictures of the OST from different perspectives revealing the in- and outside.

The observations took place at the OST (*overwhelmingly small telescope*) observatory (see the previous figure), situated in Potsdam, Golm on top of building 28, also known as the *Institut für Physik und Astronomie*. Its geographic coordinates, taken from the Wiki website¹⁰ are:

Latitude $52^{\circ} 24' 33''$ N

Longitude $12^{\circ} 58' 23''$ O

Height above msl $39 \text{ m} \pm 5 \text{ m}$

¹⁰<https://polaris.astro.physik.uni-potsdam.de/wiki/doku.php?id=en:ost:telescope:grunddaten>, accessed on the 12.07.2021

Since the observation site is directly on campus, one cannot avoid major light pollution. Potsdam as a densely populated area with its center in the southeast direction also contributes a lot to the local light pollution. As another source of stray light, Berlin, not farther away than a few kilometers, also radiates a lot of artificial light into the sky. On the Bortle scale that quantifies light pollution to some extent, the observatory shows a 5 with a mean sky brightness of roughly $20.21 \text{ mag arcsec}^{-2}$. This means that the overall observation conditions are not the best, but reasonable for spectroscopy.

There are a lot of sodium lamps standing in the vicinity, potentially causing artificial spectral features in our data in the end. However, their effect should be negligible. As we point the telescope towards the desired star, it should provide us sufficient flux to neglect other light sources. To enter the telescope, the artificial would have to be reflected almost directly along the line of sight of the star. Since the stray light is coming from almost any direction, its angular intensity is small, respectively.

A rough estimate supports this: As we have seen, artificial lighting provides us a sky brightness of at least $20.21 \text{ mag arcsec}^{-2}$, whereas we concentrate on stars with confidently not more than 10^{mag} . For our observations, we will make use of the $25 \mu\text{m} \times 135 \mu\text{m}$ slit. Therefore, according to formula (11) which we will formally introduce in chapter 5.1, the slit covers a total area of $1.49 \text{ arcsec} \times 8.06 \text{ arcsec}$ converting into a total solid angle of roughly $\sim 12 \text{ arcsec}^2$. Hence, the amount of terrestrial light, entering the spectrograph's slit, will be in the order of $\sim 17.5^{\text{mag}}$. We can see how there is still a difference of at least 7.5 magnitudes in brightness, converting itself to a natural-to-artificial light ratio of at least ~ 1000 . Even with this rather pessimistic¹¹ calculation, we can see how this ratio is still sufficient to exclude the possibility of artificial sodium doublets in our spectra.

The OST itself is an observatory being built for remote control, too. To protect the equipment against dew, harsh weather, and high temperatures, a 5-meter movable dome covers the whole setup. A slit in the roof enables us to look through it in the desired direction. Automatically, it slaves to the mount's orientation, being moved by motors sitting on the junction between the static side part of the dome, and the rotating dome itself.

Interestingly, the dome, even though it works with AltAz coordinates, usually does not match with the current object's respective AltAz coordinates. This has to do with the type of mount being used. As we will see in chapter 5.2, the telescope tube itself is towering on a German equatorial mount as shown in figure (5.1b). Even though the mount's base remains centered in the dome, the telescope tube is *not*, depending on the mount's position in the sky, which would lead to misalignment of the dome's window in general¹² case without any further corrections. Fortunately, the operating software *Maxim DL* corrects its orientation accordingly, to ensure the telescope is not looking onto the dome's wall blocking the star's light.

The software mainly used for data acquisition is *Maxim DL*. It provides us an environment in which one can control nearly all OST components at once. This includes full control of cameras, the optics, the mount, and the spectrograph with its calibration lamps, of course.

5.1 Corrected Dall Kirkham Telescope

The telescope used for the observation is a *corrected Dall Kirkham reflector* with an aperture of $20''$ (508 mm), and a focal length of 3454 mm. According to these specifications, one abbreviates the instrument as CDK20. Compared to the human eye pupil, adapted to total darkness with an aperture of 7 mm, the optic collects approximately 5 200 times more light per given unit time. This

¹¹Pessimistic, because we assumed *the absolute lower brightness limit* for the stars we can observe (even 10^{mag} is chosen very optimistically in this regard), as well as the assumption all light pollution originates from sodium lamps. Indeed, LED lamps also contribute to light pollution, but these lamps usually do not exhibit sharp absorption lines acting as potential sources of misinterpretation. In the worst case, they would, therefore, merely give us a hard time fitting the spectral continuum as black bodies, which we do not deal with in the scope of our observations.

¹²Responsible for this issue are the different reference points for the coordinates. The dome's origin of the internal AltAz coordinate system sits centered, while the telescope's altitude and azimuth, as a conversion result from ICRS coordinates, naturally refer to the position of its aperture.

is necessary to provide a gentle amount of flux hitting the detector to provide moderate exposure times for the spectra.

The working principle of a reflector telescope, like the CDK20, takes advantage of the mirrors, that reflect light instead of refracting it. Two advantages are immediately emerging from that principle:

The mirror system allows a compact construction of the tube itself, folding the beams of light inside the tube several times, before reaching the focal point. Therefore, the large focal length of more than three meters fits into the compact telescope tube.

Another important advantage we making use of is the absence of dominant chromatic aberration. For telescopes with only refracting elements, the focal length is usually wavelength-dependent. Therefore, unless the spectrograph would take this aberration into account, the collimation quality of the light, necessary for well-defined diffraction on the grating, would probably suffer. Indeed, there are several solutions to minimize these effects. Apochromatic or achromatic refractors can correct this aberration somewhat, using an arrangement of lenses with different refractive indices. However, even these constructions cannot make them vanish completely.

The CDK20, as we use it at the OST, is constructed openly. In contrast to other full-cased aluminum telescope tubes, this open construction allows the mirrors to cool down to the environment temperatures quickly¹³, which is a significant step to ensure the best imaging quality. Materials expand and shrink depending on their temperatures. Of course, so does the mirror. If the primary mirror then contains a temperature gradient, it can even change its shape, which is, of course, crucial for the telescope’s working principle. Therefore, it should be evenly tempered.

Since the telescope has such a large focal length, the resulting fields of view are quite little. From the simple geometry of focusing optics one can show that

$$\tan \frac{\alpha_{\text{FOV}}}{2} = \frac{d}{2f} \xrightarrow[\text{angles}]{\text{small}} \alpha_{\text{FOV}} \approx \frac{d}{f} \quad (11)$$

where d is the chip size in the respective direction, f the telescope focal length and α_{FOV} the angular field of view. Given the spectrometer’s slit diameter of 25 μm , we obtain a resolution of roughly 1.5 arcseconds. This number is coarsely the size of the normal seeing value for the observation site, making a further decrease of the slit diameter unreasonable, given the overall observation site conditions.

5.2 German Equatorial Mount

The telescope is mounted on a 10Micron GM 4000 QCI German equatorial mount on which it can precisely slew to any desired point in the sky. Image (5.2b) shows an actual picture of the mount, as it is assembled in the OST observatory and used for our observations, along with an minimalist sketch depicting the mount’s orientation in the sky¹⁴.

¹³We achieve an even faster cool-down with the fans sitting right in the back of the primary mirror.

¹⁴Figure (5.2a) was created with the help of real images of the mount and the telescope which can be found at <https://www.planewave.eu/en/products/telescopes/cdk20-astrograph-f/68-with-fused-silica-optics> and <https://10micron.de/de/products/gm-4000-hps/gm-4000-hps-montierung-1454010/> (both accessed on 28.09.2021)

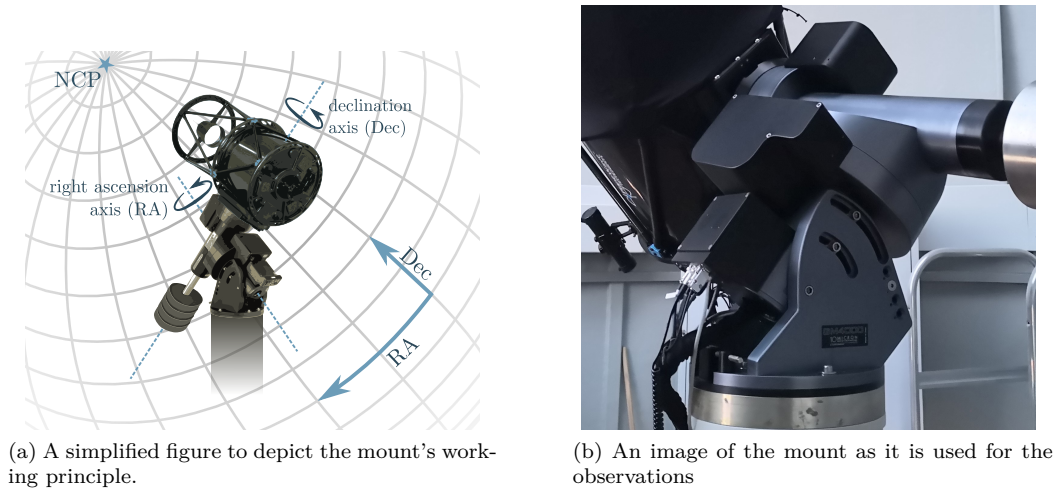


Figure 5.2: The mount, on which the telescope tube is fixed.

In this regard, we may recall the principle of the equatorial coordinate frame, discussed in chapter 4.8.1 in further detail. Earth spins around its rotation axis once in slightly less than 24 hours, making the sky seem to rotate as well within the same amount of time. The rotation axis, projected into the sky, then defines the two celestial poles - the NCP and SCP. As we align the two rotation axes to the celestial reference frame (see figure (5.2a)), we need to compensate for this rotation on the RA axis solely. Meanwhile, the position on the Dec axis remains stationary during the whole observation process. Tracking errors, caused by the mount's internal mechanics can, therefore, be eliminated at least in one direction.

The computerized mount also makes it possible to point the telescope in the desired direction either by inserting the object's coordinates directly or, in case the Object is listed in a specific catalog, its name can also be associated with a tuple of sky coordinates. This also ensures no misinterpretation of the target occurs as star-like objects somewhat look all the same.

5.3 Working Principle of BACHES - an Echelle Spectrometer



Figure 5.3: An image of BACHES - The high resolution echelle spectrometer, utilized to perform this observation, with the SBIG St8 camera attached to it. This image has been taken from the OST Wiki page.

The central device in this observation series is, indeed, the spectrometer. We make use of an *echelle spectrometer* in this regard.

The advantage of such a spectrometer is its comparatively high resolving power, covering the whole spectrum of visual light.

Understanding its working principle is crucial for our knowledge of how we extract the intensity profiles later in the data reduction. Figure (5.4) schematically presents the path which the light takes to form a so-called *echellogram*.

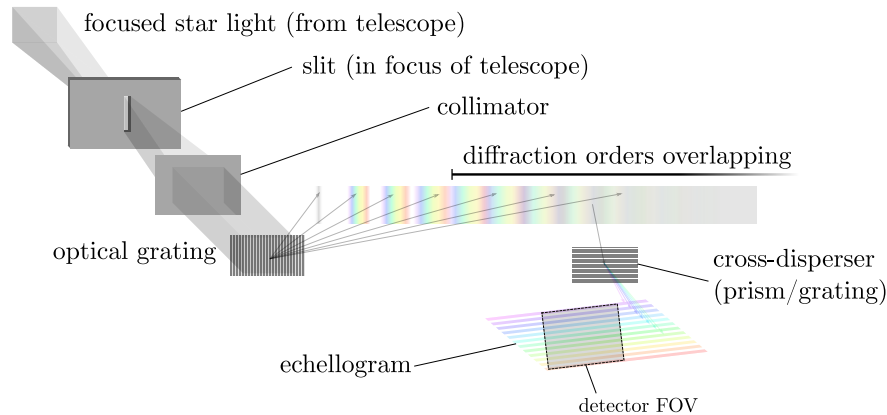


Figure 5.4: In order to create an echellogram, the light has to pass two dispersive elements, arranged in a way that their dispersion directions are oriented perpendicularly. Therefore, the spectrum becomes two-dimensional in the end.

The echelle spectrometer, depicted in the upper figure, makes use of two energy-dispersive elements. It could either consist of a combination of two gratings or a diffraction grating and a prism. In either way, the optical parts are oriented in a way, that the light gets diffracted and refracted perpendicularly. For the result, it is irrelevant whether the light passes the echelle grating and then the cross-disperser¹⁵ or vice versa.

Let us understand the way the light goes along in the spectrometer.

First, a slit only allows light from a very certain direction to enter. It is achieved by moving the star or light source of interest in general, onto the slit which sits in the focus of the telescope. Behind the focus, the beam of light naturally diverges again. Therefore, the next step is to collimate the light again as it gets diffracted on an optical grating afterward. In the case of the BACHES, the collimation is done with a doublet of lenses to minimize chromatic aberrations¹⁶.

The parallel beam of light then hits an echelle grating¹⁷ in the next step, where it gets diffracted. Now, the most fundamental idea comes into action:

Regular high-resolution spectrometers are usually only optimized for a narrow wavelength interval within the visual part of the spectrum. It is a trade-off between getting high resolution and a broad spectrum, and being able to cover a large spectral range. For one-dimensional intensity spectra (like just a spectral order of a diffraction grating, for instance), the problem occurs that

¹⁵One calls the secondary dispersive element the cross-disperser. So it is either the secondary grating or the prism, but not the echelle grating.

¹⁶According to the BACHES description manual from Baader Planetarium, which can be found online at the following web page:

https://www.baader-planetarium.com/en/downloads/dl/file/id/1342/product/2876/eos_messenger_129_sept_2007_baches_a_compact_light_weight_echelle_spectrograph_for_amateur_astronomy.pdf
(last accessed 13.09.2021)

¹⁷according to the BACHES description manual from Baader Planetarium (source URL can be found in footnote 16) the specifications of the echelle grating in case of the BACHES are 79 lines per mm and a blaze angle of 63 degrees.

the spectrum's measures surpass the sensor's dimensions at high resolving powers. This is due to the higher wavelength dispersion $d\lambda/d\varphi$ where φ denotes the dispersion angle of the respective wavelength.

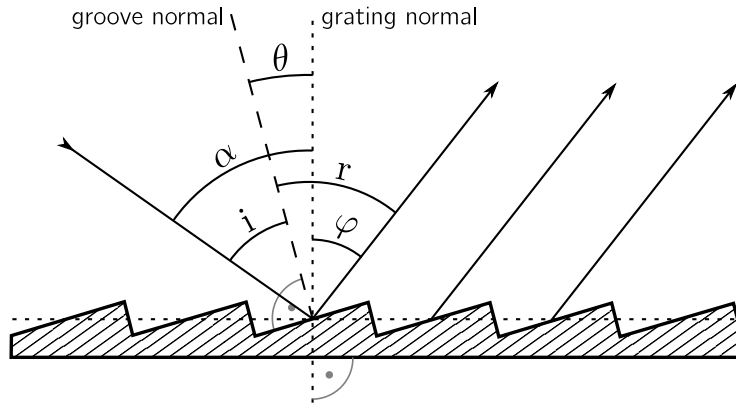


Figure 5.5: Geometry of a blazed reflection grating

For the special case of echelle gratings, we make use of the higher grating's diffraction orders, like it can be seen in figure (5.4) again. According to the grating equation, telling us at which angles the wavelengths are being diffracted most efficiently, i.e. the angular position of the diffraction maxima for certain wavelengths (see figure (5.5) for further visual assistance), we have

$$n\lambda = g(\sin \varphi_n - \sin \alpha) . \quad (12)$$

As we can see here, the maxima n with their positions φ_n do not depend on the blaze angle θ , but on the incident angle α and the wavelength, of course. Indeed, the idea to manufacture a blazed grating has the reason that we want to reflect the majority of the light intensity toward very high orders. However, their angular positions remain unchanged in this process. Considering we aim for a high resolving spectrometer, we are interested in the higher diffraction orders since RAYLEIGH wave optics tell us that for higher orders, the spectral resolution $R = Nn$, where N is the number of illuminated lines and n again the order index. We can therefore conclude for higher diffraction orders, we get to reach higher values for R .

Keeping in mind the points just mentioned previously, echelle gratings, usually, can be characterized with the following two characteristic specifications:

- Echelle gratings have low line densities (i.e. comparably large line spacing). These are in the range of $10 \sim 100$ lines per mm so that the order's overlap is reasonable on the camera chip.
- Such (reflective) gratings are built with extraordinary high blaze angles θ to reflect the peak intensity to high diffraction orders.

Unfortunately, another issue arises in this region: Orders begin to overlap, as they become broader for increasing order index. (see figure (5.4)) Looking onto such overlapping orders would result in looking onto a white stripe of light again. Because only a fixed number of orders overlap, one can separate these orders again by application of a secondary disperser - the cross-disperser. After the beams of light are focused again, a two-dimensional spectrum, called an echellogram, forms after all. See figure (5.6) for an example how such a spectrum looks like.



Figure 5.6: An echellogram, like it forms on a camera sensor (brightness inverted). This is a spectrum of V1405 Cas. It is a stack of 3 images, each exposed for 2000 s, taken on the 10.05.2021 at the OST as part of our observations.

One can see here, how the whole visual spectrum is projected on the camera chip but split up in many sections each covering the whole sensor from left to right. Furthermore one can identify intervals within the orders which represent the overlap. These are regions, where the same pattern¹⁸ appears on the image's left and right edge in adjacent orders. A further step in the data reduction finally stitches the diffraction orders together to recreate the whole visual spectrum in very high resolution, like it would not be possible just for a setup with a single grating or prism.

¹⁸Hereby meant is a sequence of distinct spectral lines.

6 The Observations

The most essential parts of this thesis are the conducted observations, for sure. The whole process of getting, from the very beginning - the planning of an observation night itself - to the final data product and its interpretation, requires us to go through many steps in between. The following flow chart (see figure (6.1)) should give us an idea of how this whole process looks like. Due to its complexity, the more detailed description of the data reduction process is distributed over the following few chapters. We will refer to this figure in the ongoing text from time to time as it somewhat *defines* the structure from now on.

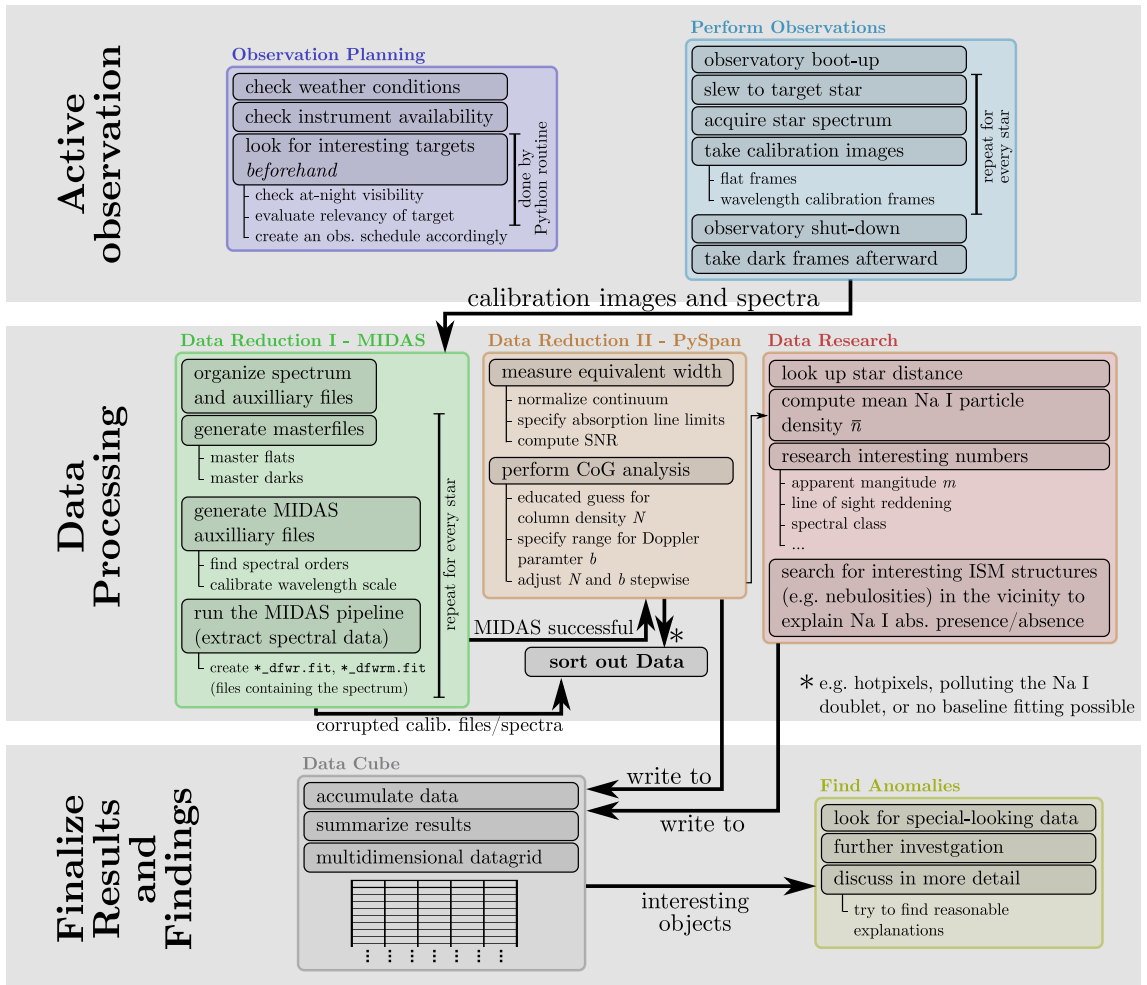


Figure 6.1: A flow chart, depicting the whole management of data acquisition and the data processing and reduction.

6.1 Active Observations

To evaluate data, we first must acquire it. This part should describe how the actual observations were made, and what we have to consider during them. Referring to the flow chart in figure (6.1), we start in the uppermost box with the observation planning.

6.1.1 Preselection of Promising Stars

The night sky is crowded with stars, potentially observable with our medium-sized telescope in conjunction with the equipped spectrograph. Assuming we could observe stars with magnitudes

up to 8th magnitude, we would end up with roughly $\sim 40\,000$ observable candidates¹⁹. This shows us that we need to filter this list concerning some criteria, beforehand. The job is carried out with a python script querying the Hipparcos star catalog as the fundamental set of stars. The specific selection criteria are discussed in the following chapter. The exact working principle of the program is explained and shown in the thesis’s appendix.

6.1.2 Selection Criteria

To select potential promising candidates, we sort stars according to their

apparent magnitude

To provide sufficient counts in our spectra within reasonable exposure times, we need to ensure that the stars we are about to observe are bright enough. Experiences show, that stars brighter than $7^{\text{mag}} \sim 9^{\text{mag}}$ are sources, good enough for providing reasonable count rates.

surface temperature

As discussed in the theory part of this thesis, we require the stars to provide a spectrum with as few stellar absorption lines as possible. We then take advantage of the missing stellar Na I doublet, as well as the well-defined star spectrum continuum. The latter allows us to better distinguish between actual absorption features from noise.

visibility

Of course, we also have to ensure the star’s visibility on a respective observation night. Visibility, in this case, does not only mean “just above the horizon” equivalently, but to rise as high as possible to have a reasonably small air mass, the starlight is going through. Our atmosphere can affect the spectrum’s quality negatively since it can refract, absorb or scatter starlight.

line of sight reddening

Since we are interested in the identification of ISM features, we predominantly want to observe stars in directions with noticeable interstellar reddening. These are the directions where we would expect the respective stars to provide ISM absorption features in their spectra most likely. Hence, we query the respective extinction coefficient E_{B-V} for every star that has met all the previously mentioned conditions, and set a certain threshold for E_{B-V} that an arbitrary line of sight’s one must overpass, so the respective star is not getting sorted out.

Applying all these steps for an observation night, one usually ends up with just a hand full of stars, depending on the strictness of the selection requirements. The following graph shows how many objects have been sorted out (for an arbitrary observation night) after every filter step and how many stars made it to the end in this example.²⁰

¹⁹This number arises from a quick query of the Hipparcos star catalog (accessed through the Gaia data archive), filtered stars up to 8th magnitude.

²⁰**The following parameters were chosen in this case:** *observation site:* Earth location coordinates of the OST observatory; *date/time of observation:* 2021-08-01 22:00 CEST; *minimum altitude above the horizon:* 20 degree; *max apparent star magnitude:* 7^{mag} ; *maximum observed B-V color index:* -0.1^{mag} ; *minimum reddening:* 0.4^{mag}

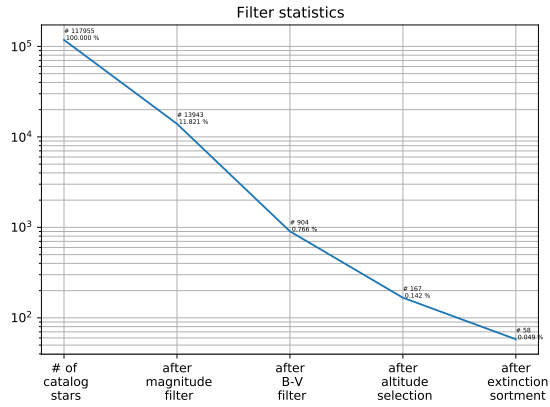


Figure 6.2: Filter history plot, showing the conditions after which we sorted out the stars. One can see how we started with the whole Hipparcos catalog and decimated the amount of potential interesting stars after every step. The plot assumes a time of observation at 2021-08-01 22:00 CEST. Here, the galactic equator stands high above the horizon in mid-European skies, leading to a high amount of remaining stars after the final filter step.

6.1.3 Regions of General Interest

Even though the brightest stars are scattered all over the sky evenly in first-order approximation, there is some particularly interesting region in the sky with a general interest. In the scope of this thesis, we observed a few of these regions more thoroughly than others. As we take a look at a reddening all-sky map (see figure (9.1), for instance), one can easily see where the interstellar extinction is especially high. Particularly at low galactic latitudes a lot of ISM compiles along the lines of sight since star formation predominantly takes place here. Figure (6.3) illustrates the reddening in direction of the brightest stars on the night sky.

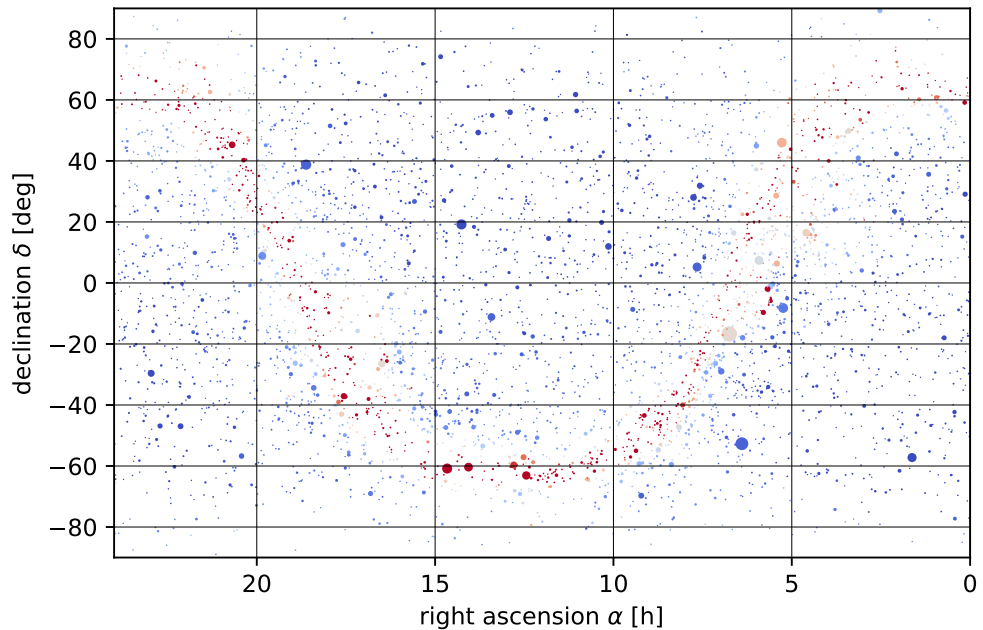


Figure 6.3: An all-sky map of stars, visible to the human eye (up to 6^{mag} apparent magnitude). The colors refer to the extinction value in the respective line of sight. Here, red stands for high extinction and blue for only a little. One can easily make out the position of the galactic band. It is the red stripe going from the left to the right, looking like a cosine oscillation pattern.

As an unfortunate coincidence, the majority of the presented observations are being conducted during the spring season, where the Milky Way sets close to the horizon at night. Instead, the galactic north pole (situated in the constellation Coma Berenices) rises high up in the night sky. Because of this, we look perpendicular out of the galactic plane, where we could expect the least ISM abundances, and, therefore, find stars, less likely to exhibit ISM absorption features. However, during dusk and dawn, the Milky Way ascends gently high up above the horizon, enabling us to observe at least a few interesting regions within the galactic disk.

A nice example is the constellation Cygnus, floating fairly centered towards the galactic disk and providing particular interesting regions filled with a lot of nebulosities like H II regions, reflection nebulae, and dark nebulae. We therefore also concentrated on that direction, even though other parts of the sky were covered in this compilation of observations.

Along the galactic equator, constellations like Cepheus and Cassiopeia row up, but due to their higher right ascension coordinates, they only rise late in the morning. At this time, also parts of the galactic center rise above the horizon, making stellar spectroscopy possible on its very northernmost tip.

Other canonical regions, well known for the high abundances of ISM, are the constellations Orion and Taurus. Unfortunately, both are already set very early during dusk, making them hard to observe in this kind of manner. Nevertheless, a few stars have been monitored.

6.1.4 The Python Routine

For the selection of stars we made beforehand, we wrote a Python script, performing the filter process and helping us to obtain potential promising candidates in this regard, taking the previously mentioned criteria into account.

Because of the code's complexity, we just want to focus on the principal ideas for this code. However, one can find a rather detailed description of the code in its wholeness in the appendix in chapter 12.1.

The principal idea for the Python routine is to filter stars for which the requirements discussed in chapter 6.1.2 are met and sort the remaining candidates accordingly.

Important note: The code utilizes the Python package `dustmaps` for which only a Linux version is available yet. One, therefore, has to run the script either on Linux OS or a virtual environment like the Linux subsystem for Windows, for instance.

As the initial, unfiltered set of stars, the program takes the Hipparcos catalog. It contains more than 100 000 stars, which are scattered across the whole sky. Additionally, the catalog is complete up to an apparent magnitude of $m_V = 7.3^{\text{mag}} \sim 9.0^{\text{mag}}$ in the V-band [1]. Since we are truly not interested in stars dimmer than this, the catalog’s completeness in this range just meets our requirements to contain all stars in this brightness range. The catalog itself lists individual stars with their positions on the sky, their apparent magnitudes, and their respective $B - V$ color indices.

The first filtering step is taken with respect to the star’s apparent magnitude. This step should throw out the majority of the stars, not being observable at all due to their faintness. Depending on the optics used and the performance of the setup, the user is able to set brightness cut-off individually. Since fainter stars are far more abundant, applying a brightness cut-off at roughly $8^{\text{mag}} \sim 9^{\text{mag}}$, like it was commonly used for the planning of the observations, filters out nearly half the stars in the whole catalog (see the filter statistics shown in figure 6.2).

The second step is the exclusion of stars, not providing us sufficient high surface temperatures. We filter for the $B - V$ color index in this regard, since a lower $B - V$ index represents a bluer black body spectrum, resulting in stars with higher effective temperatures.

Note: These $B - V$ indices are observational quantities. Also, very hot stars may appear redder than intrinsically are. This *can* be due to the extinction of the ISM. One has to keep in mind, to set especially this threshold not too strict, to not throw away hot, but severely reddened stars.

In order to reduce computation time, we applied the latter two filter steps first, since these simply compare entries in a list, rather than starting actual calculations. The following step requires (partly a lot) of internal math to transfer all the remaining star’s coordinates into another coordinate frame. Therefore, it is just logical to reduce the number of stars and therefore the number of calculations that have to be done beforehand.

The next step is to further reduce a large number of simply not observable stars, by converting their ICRS coordinates, as listed in the catalog, into the AltAz observatory frame. After this, the program filters out any star with an altitude angle less than a certain threshold, as given by the user. This step should leave a shortened list with at most a third the length of the number of unfiltered stars.

The last filter we apply is the filter for the line-of-sight extinction. This step is carried out with a query of the Schlegel, Finkbeiner & Davis (SFD) [34] all-sky extinction map with the help of a Python API provided with the `dustmaps` package. Insertion of a list of coordinates as arguments of the respective Python function returns the line of sight extinction values.

Of course, we are particularly interested in rather high extinction values because we expect the most prominent presence of ISM in these very directions. As we have seen in figures (6.3) and (9.1), the largest area of interest is the band of the Milky Way itself, concentrating the majority of dust and interstellar gas in it. This is also the reason why the output length severely depends on the observation time and season of the year. In winter, stars with a high line of sight reddening standing above the horizon are far more abundant than in spring, for instance. This has to do with the orientation of the galactic equator in mid-European night skies. All prominent constellations along the galactic horizon (e.g. Cassiopeia, Taurus, Orion, Cygnus, etc.) are canonical fall- to winter-constellation rising high up above the horizon in that very time of the year. In contrast to that, the galactic north pole rises closer to the zenith during spring, making it hard to observe stars close to the galactic disk during that period.

Depending on how strict the conditions are set, one ends up with a certain amount of stars. Of course, the thresholds can be varied accordingly to end up with a reasonable list length of potential interesting candidates for one observation night.

6.1.5 The Observational Process

In this chapter, we discuss the steps that we are going through in order to assure reasonable and calibrated data output for our observations, starting with the discussion of what weather conditions it needs to perform spectroscopy on stars in general.

Observation Conditions As we do spectroscopy, we are interested in the wavelength composition of the light that we are observing. Our primary goal for these observations is the identification of ISM absorption features in spectra of hot stars. To detect these line features, we do not strictly require perfect observation conditions, meaning that also a very slight cloud coverage is sufficient. Since we do not take wide-field images of parts of the sky, we do not need a homogeneously illuminated field of view of the sky. Hence, clouds temporarily blocking out starlight will only result in a lower signal to noise ratio here, but will not make the data output useless. To compute the equivalent widths, later on, we are not even interested in the shape of the continuum as we normalize to that value. If any obstruction lowers our signal during our observations, it will luckily do so for all wavelengths in a certain range by the same amount. Normalization then leads to the same idealized result.

If we were interested in Photometry, it would be different. There, we measure the quantitative flux of light and would assume the sources to radiate at a constant rate, not taking any intensity-blocking effects into account. Therefore, we would indeed require the sky to be crystal clear in this regard.

Calibration Images In addition to the actual star's spectrum, we need to take some calibration spectra beforehand. In the ongoing text, we will discuss the purpose of the respective calibration images, and what we have to keep in mind while capturing them.

dark frames

Due to the CCD sensor's internal electric architecture, some pixels might show a signal, not belonging to the source of light we want to observe. Of course, this is a signal we are willed to correct afterward. The solution is to take an image, where we ensure, that no natural light or stray light hits the detector. We then expect an absolute dark image as the result of this process. Indeed, it will most likely not be dark everywhere. Certain pixels, also known as *hot pixels*, show a noticeable amount of signal, even though there is no light to detect. We assume this dark current to show up in the same way as in the actual image of the spectrum, too. Therefore, for *every* exposure with a different exposure time, we take we have to take a respective dark frame to correct this noise.

For a usable dark frame, we must ensure the dark frame is being taken under the same conditions as the light frame. This is because the dark noise varies with temperature, exposure times, and of course the model of the sensor. This way, we ensure not to over-, or under-correct our images in the end.

flat frames

In any optical/imaging setup occurs the phenomenon of vignetting. Usually, certain areas on the camera chip array are illuminated differently. This can be due to the way of the optics' construction and results in darker image edges and corners, with those areas lacking flux. But also dust grains and other pollution might cause some shade on the sensor, leading to a locally reduced sensitivity. By taking a flat frame, we, therefore, correct the overall image illumination gradient and dust shadows.

Assuming the optics and the cameras were working perfectly, and we used a flat field lamp²¹ with an even spectrum, we would also expect to see homogeneously illuminated spectral order on the image. Every deviation from this is then being corrected by dividing the light frame

²¹One has to choose a reasonable light source for the flat field lamp. We should not make use of lamps intrinsically containing sharp absorption, or emission lines in their spectra. In this case, we would severely over-, or under-correct the actual spectrum at these wavelength positions, and virtual emission peaks would emerge in the flat-calibrated light frames. In this observation, we equip a halogen lamp as the flat-field source.

by the flat-field image. This way, areas naturally less illuminated will be divided by a smaller value and, hence, becoming corrected in a way that we scale every pixel value accordingly. Flat-frames are crucial since localized dust shadows could be otherwise misinterpreted as spectral absorption lines in the data reduction by accident.

In the special case of spectroscopy with the BACHES spectrograph, such exposures are also important to identify the spectral orders in the image, considering the program initially has to find their positions to get the information where to read out the fluxes in the image.

dark flats

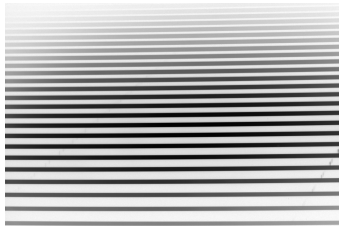
Indeed, also the flat frame, since it is an image taken by our camera sensor, needs to be dark corrected. Hot pixels in the flat frame would cause intensity dips in the light frame, as we would locally divide by a very large pixel value. This deviation is caused by the setup, for which reason we need to correct this. In fact, for the so-called dark-flat frame we have to pay attention to the same prerequisites as for regular dark frames, mentioned before.

wavelength-calibration spectrum

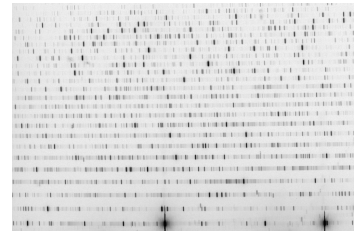
With the calibration steps taken, we can correct the respective flux values thoroughly. Still, this is not enough to provide us a spectrum in the end. The abscissa - the wavelength scale - needs to be calibrated as well. This step is carried out with the use of a spectrum consisting of many distinct emission²² lines. Given the absolute wavelengths of the detected emission lines, the pipeline compares their position on the chip array. Furthermore, it performs a linear regression for every spectral order to construct a wavelength scale for each order on the sensor. As it reads out the signal, it can assign the respective wavelengths to it. As a result, we have detected a spectrum for every order with a calibrated wavelength scale.



(a) This is an arbitrary (brightness inverted) dark frame (1000 s exposure time at -20°C camera chip temperature).



(b) This is an arbitrary (brightness inverted) flat frame (5 s exposure time at -20°C camera chip temperature).



(c) This is an arbitrary (brightness inverted) wavelength calibration frame (30 s exposure time at -20°C camera chip temperature).

Figure 6.4: A set of arbitrary calibration images, demonstrating how the results commonly look like. All images were taken with the SBIG STF8300 CCD camera in conjunction with the BACHES.

Obtaining the Echellogram As we gather the data, later being the basis of our data discussion, by ourselves, a crucial and certainly most time-consuming part of the observations will be the process in which we acquire the echellograms (the spectral data) themselves. In order to end up with spectra, providing us a reasonable SNR²³ requires a lot of exposure time because many stars that we observe in this regard are relatively faint.

In general, there is an upper limit to what time we can expose for, too. It is the maximum exposure time before the sensor gets saturated. As mentioned, the stars that are going to be observed are generally faint. Hence, we would not enter this saturation limit even if we were exposing them for several hours. As long as the sensor's thermal noise is small enough in comparison to the signal that the star provides us, the longer we expose the image, the higher the SNR becomes, and as a consequence, the better the quality of our data will be.

²²In principle, also absorption lamps would work for wavelength calibration. However, in this regard we use a Thorium-Argon (ThAr) arc lamp, producing a lot of emission features.

²³signal to noise ratio

Another decisive point is the cooling of the camera. Since the detector is a source of (infrared) radiation, we can lower thermal noise as we cool the camera as low as possible during the imaging session. Of course, we have to adjust the temperature at which we take the dark frames accordingly. It applies: The cooler the camera chip, the lower the thermal noise, and therefore the higher the SNR becomes.

Observatory Handling (with Maxim DL) For the observations to be carried out, the control of the whole OST observatory is indeed an essential part of the process. In the ongoing text, we want to cover the most important points, describing the handling of the OST with its controlling software Maxim DL. Let us have a brief go-through of a canonical observation night:

Attach the camera to BACHES

At the very beginning, one has to mechanically connect the camera to the BACHES. The latter is usually stored in a separate hard-shell case, stuffed with foam, preventing it to suffer from stress during transportation.

Assemble BACHES (+ Camera) on the back-side of the Telescope

Before the observations can take place, we need to attach BACHES on the back-side of the telescope where the eyepiece usually sits. With the appropriate adaption, the spectrograph can be fastened in the focuser shaft directly.

Boot-up the observatory

Next, we have to boot-up the observatory and all its components. As of spring 2021, this has to be done by logging into the *observatory management system* (OMS) with the respective credentials. Once connected, we have to power the telescope mount²⁴ and the power connectors for the camera. After Maxim DL has been started, we also have to connect the dome and the cameras (generally the guiding- and the imaging camera). At this point, we have to decide to what temperature the imaging camera needs to be cooled down to, as the coolers are activated, and the desired sensor temperature has to be set to a fixed value. A reasonable cool-down temperature depends on the air temperature, being usually 30 K to 40 K higher.

Optimize the focus

First, we have to assure the guiding camera produces sharp images of the spectrograph's entrance slit. The focus can be optimized by carefully shifting the guiding camera in or out in its respective tube. It is recommended to go through this process while the flat field lamp is activated and the reference mode enabled to let in light, providing us contrast to determine the slit's position on the image. The focus adjustment of the whole BACHES on the telescope now follows. Only at this very position, the spectrum's quality maximizes, and we specifically cut out the region of interest on the sky. For this purpose, one should slew to a sufficiently bright star, and check whether its image appears sharp and well-defined on the aperture plate. If this is not the case, we have to adjust the telescope's focus position until it is. At the end of this step, the setup is aligned and ready to perform well for spectroscopy.

From now on, the following points have to be redone for every single object to be observed.

Slew to the target star

We have to enter the ICRS coordinates in the Maxim DL's mount control panel so the telescope can slew to the desired object. The respective coordinates can be obtained either by a query of Maxim DL's internal database of astronomical objects or a SIMBAD query, for instance. It might be also necessary to manually do the fine adjustments and to center the star on the slit. During the exposure, we might have to guide the mount manually, using the **N**, **S**, **E**, and **W** buttons on the hand terminal, as the position of the star may shift during that time. This can be due to internal tracking errors of the mount, for example.

²⁴As part of the boot up process, we have to make sure the internal clock (as it appears on the mount's hand terminal) of the telescope is synchronous to real-time. Minimal shifts in order of seconds affect the preciseness of the mount's pointing.

This process can also be done electronically assisted. In this case, before we center the stars on the slit, we have to go through a brief calibration process in Maxim DL's guiding panel. Only then, we can guide the telescope. During this process, Maxim DL makes the mount move along the two motorized axes and recognizes its response, as the star's position moves across the field of view.

Take the calibration images

Just before we expose the camera sensor to the starlight, we take the calibration images to ensure the spectrograph's mechanics do not flex between the time at which we take the calibration images and the actual spectrum. This would, indeed, lead to useless calibration frames and would make our data impossible to interpret afterward. In principle, it is irrelevant in which order the calibration images are being taken. Concretely speaking: The chronological order of flat frames and wavelength calibration image acquisition does not matter. For both, we have to activate the reference mode once again. For the flat frames, we usually acquire several ones to optimize the SNR, whereas, for the wavelength calibration images, the SNR is generally good enough for just one single image.

Exposing the spectrum

The crucial-most part takes place now: The obtainment of the actual star spectrum. For this purpose, we have to leave the reference mode again. Within a well-chosen exposure time, the star now has to be kept centered on the slit (manually or automatically). If there is a cloud crossing the line of sight during that time, it will just reduce the overall flux of the star, principally not affecting the spectrum's local structures in the end.

If we desire to observe other targets during the same observation night, we should repeat the last three steps, respectively. Otherwise, we can proceed with the shut-down process as mentioned in the ongoing text.

Shut down the mount/Close the hatch

After the last exposure is complete, the observatory must be shut down properly. The telescope has to be moved to its park position (pointing towards the western horizon) first. After the slewing has been completed, the mount can be shut down in the main OMS main panel. Meanwhile, the hatch can be closed, using Maxim DL and disconnected afterward.

Take darkframes

By now, the only devices, that are still active, are the cameras. Only the camera that has taken the spectra is of further need, for which reason the guiding camera can be shut down and disconnected, too. The imaging camera has to be kept at temperatures, matching those used during the actual exposures for the spectra. For a better statistic, one should take a set of dark frames, having the exposure times of the spectra images, and the flat frames. As discussed previously, for the dark frames, we have to avoid any stray light from hitting the sensor. Usually, the closed observatory dome provides us sufficient darkness to ensure a sufficient dark frame quality.

Shut down the cameras

All necessary auxiliary images have been taken so far and, therefore, the imaging camera can be warmed up to ambient temperatures, disconnected from Maxim DL, shut down, as well as being detached from the spectrograph.

Detach BACHES

The last step of observation is the detachment of the spectrograph itself from the telescope. Here, we also have to properly disconnect the cable connections, and store loose parts in their designated places. We have to mind that especially optical surfaces vulnerable to dust pollution have to be covered with their respective dust caps.

6.2 Data Processing

This chapter describes the steps we have gone through in order to get the data set, as it is presented in table (2) later on.

Referring to the flow chat in figure (6.1) again, we now have reached the second large gray box, mainly dealing with the data reduction.

6.2.1 Data Reduction I - MIDAS

As of now, we discussed how to obtain the raw data (the echellograms, as well as the respective calibration frames, for instance). Obviously, there are more steps that have to be taken in order to get to the numbers and quantities we are interested in, in the end. Therefore, in this chapter, we want to cover the principal ideas of the MIDAS data reduction pipeline²⁵ and what steps it needs to obtain a one-dimensional intensity profile for the whole visual spectrum and a go-through of the data reduction process itself using MIDAS.

In the chapters 6.1.5 and 6.1.5, we already discussed the necessity of different calibration frames. As we have taken a set of files (flat frames and dark frames, for instance), we are interested in combining the signal, providing a better statistic in those images, and, hence, an accurate calibration afterward. This step is done with a python script called `1_masterimages.py`, as one can find in the file archive of the astrophysics lab course at the University of Potsdam. The code for this file is attached in the appendix for more transparency.

In principle, the script produces a statistic for every image pixel in the set of the calibration frames, given in a certain file directory. Assume we took a collection of n calibration images for every pixel. Then, we have n (different) intensity values out of which we can compute the mean or median. The stacked images then contain more information as they have been exposed n times longer than a single calibration frame. Hence, the SNR improves accordingly.

Another step for the flat frames, particularly carried out by the script, is the dark-flat subtraction from the calibrated flat frames.

The resulting images after this step are automatically named `master_flat.fit`, and `master_dark.fit` if not explicitly changed this in the respective Python script.

To identify the spectral orders in the echellogram, MIDAS needs to recognize them in the image. Therefore, the flats provide widely illuminated orders, easy for identification as the light of the flat-field source covers the whole visual spectrum's wavelengths and makes them visible to the camera. Given a few parameters (order count, order separation, and order width) by the user, MIDAS does a polynomial positional fit on the chip array to remember the order's positions in the following (calibration) spectra. This step is necessary because this way, the program knows where to extract the spectral data in the images later.

Knowing where the signal can be found, MIDAS moves on to the wavelengths calibration. As said, this is done with the Thorium-Argon spectrum, providing us many spectral features with given wavelengths. Based on this, MIDAS can interpolate a wavelength scale along the orders and can associate a wavelength to any pixel within every spectral order.

After this step, MIDAS already created a bunch of auxiliary files, containing the calibration parameters. These are used for the extraction of the signal in the stellar spectra.

After starting the actual data extraction pipeline for the stellar spectra with its respective command, MIDAS creates files, containing the data in different formatting. However, we are only interested in the `starXYZ_dfwrn.fit` file as it includes the merged²⁶ spectrum of the star, whereas `starXYZ_dfwr.fit` comprises the signal separated for every order.

What we end up with is a dark-subtracted, intensity normalized, and merged visual spectrum of the respective star that we can now interpret accordingly.

²⁵An even more detailed description of the data reduction process can be found on the OST wiki page.

²⁶In fact, this is what the `m` in the file name indicates.

6.2.2 Data Reduction II - PySPAN

Already at the beginning of the data reduction, it was concluded, the data reduction process itself is a highly non-trivial and multi-step process, requiring us to organize the code in a certain way.

The idea to code a Python Program, usable for data reduction, seems promising in this regard. It contains many important, as well as convenient routines, and directly interacts with the user, enabling us a quick data reduction for any star spectrum.

The Python Program itself is inspired by the SPAN program, provided by Prof. Dr. Philipp Richter, that uses the MIDAS programming language. However, PySPAN is not intended to be the converted version of SPAN into Python language solely, but also should be enhanced with some more features.

Note: The program will be also a *work in progress throughout* the finalization of this thesis, and, of course, will remain a subject of further development afterward.

In the following chapters, we want to discuss and understand the most essential routines and respectively taken steps, as well as the major ideas on how to extract certain parameters out of our spectra.

Fitting the Baselines Particularly interesting is the fitting of the baseline. Since we are particularly interested in the ISM absorption's equivalent width, we have to normalize the signal to the continuum, which the user, yet, needs to do by hand. For this purpose, the user marks the baseline with a set of coordinate tuples directly in the diagram. With this given set, the pipeline tries to fit a polynomial through the specified coordinates, representing the local continuum flux.

At the end of this process, one achieves an approximated baseline, with which we can normalize the spectrum. Of course, the baseline is only valid in the respective wavelength range, where the coordinate tuples are specified. For spectral region lying out of this range, the baseline will be an extrapolation, most likely not representing the continuum flux sufficiently.

Radial Velocity Essential for the comparison of the radial velocity profiles is, most certainly, the radial velocity itself. With the non-relativistic Doppler formula

$$\frac{\Delta\lambda}{\lambda_0} = \frac{v_r}{c}$$

we can extract the wavelength shift as we strictly measure $\Delta\lambda + \lambda_0$ during our observations and take the literature value for the rest wavelength as given in the NIST Database. Therefore, the radial velocity becomes a function of observables and constants

$$v_r = \frac{\Delta\lambda}{\lambda_0}c + v_{\text{bvc}}$$

Here, we may introduce the *barycentric radial-velocity correction* (commonly abbreviated as BVC). Since Earth orbits the solar system's barycenter, our measurements include Earth's motion along the line of sight towards the target of interest. The BVC then converts the measured radial velocity v_r into another reference frame that is independent of the observer's intrinsic movement within the solar system. It somewhat generalizes the radial velocities in a way that independent measurements at different observation times are easier to compare. This quantity is, like many others, obtained by a Python function, taking the geographic coordinates on Earth, the observation time, and, of course, the sky coordinates into account, to compute the respective BVC value, which eventually needs to be added to the observation-based radial velocity.

Equivalent Width Technically, the primary goal is to perform the easy integration, given in formula (6), to obtain W_λ . As written in this equation, for W_λ , we need to know the continuum flux, which we have already determined with the method, described in the most recent paragraph. With the help of a computer, it is now easy to calculate the equivalent width as we have to integrate over all the "missing" flux in the spectrum. The user specifies the integration limits, yielding the interval over which the program adds up the signal according to equation (6).

7 Overview on the Data

We have now reached the third large gray box in the flow chart (see figure(6.1)). The idea of this chapter is now to give a brief overview of the data product of this observation.

In total (as of 23.08.2021), there have been 39 different stars/star systems observed. Thereof, for 2 stars systems, archival data was used. In the scope of this thesis, 48 single exposures (excluding calibration exposures) have been taken, compiling a total exposure time of roughly 915 minutes, or $15\frac{1}{4}$ hours respectively, for all stars together. The following figure (7.2) illustrates the distribution of the observation subjects in the sky.

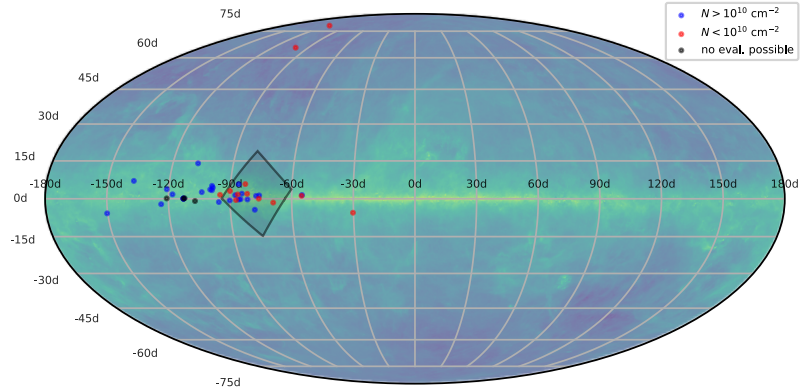


Figure 7.1: The figure shows an all-sky view (in galactic coordinates) in the Mollweide projection, indicating the positions of the stars that were observed during our observations. Also, the stars of which the data was accessed from OST archival spectra are listed in this diagram. One can see a bunch of stars, concentrated in the region Cygnus-Cassiopeia, close to the galactic equator. The gray rectangle depicts the area, covered by the wide-field as seen in figure 7.2.

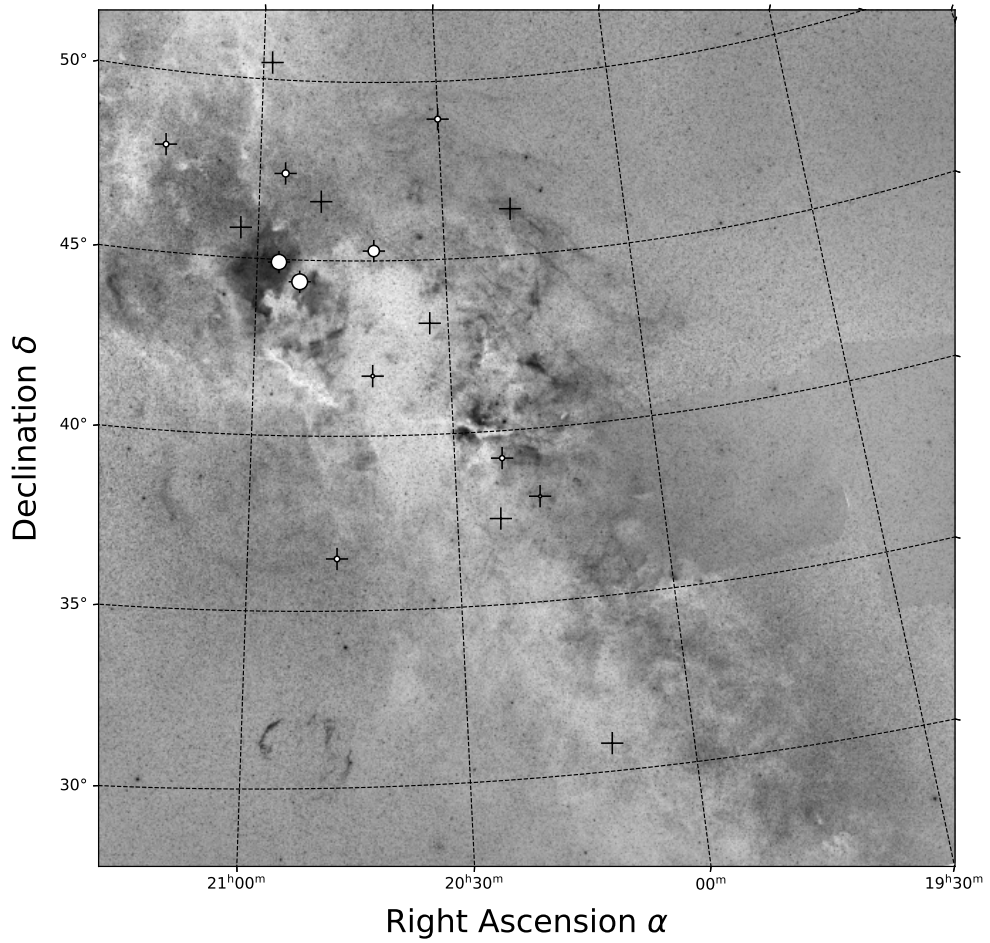


Figure 7.2: A wide field of the constellation Cygnus, with the stars, observed in this context, and their respective Na I line of sight mean particle densities n .

Listed in the following chart are the most important facts and comments on the respective candidates, covered by our observation.

Table 2: Two tables, listing briefly the most important numbers, retrieved from the observed stellar spectra and researched from SIMBAD. All spectra have been taken at the OST observatory. If not specified differently, the parallaxes were retrieved from the Gaia DR2 and EDR3. [14, 13] All apparent magnitude values for V1405 Cas were taken from the AAVSO database. Screenshots of the AAVSO star V-band photometry curve, showing the respective archival observation results, can be found in the appendix.

#	HIP identifier	Object name	Spectral class	RA deg	Dec deg	m_V	Parallax mas
1	HIP102589	λ Cyg	B5V [37]	311.852	36.491	4.54 [12]	4.24(43) [41]
2	HIP103312		B8Ia [20]	313.958	47.418	5.64 [12]	0.319(68)
3	HIP106186		A0	322.609	58.316	8.86 [18]	3.204(35)
4	HIP106285		B0Ib [15]	322.910	57.503	7.43 [18]	0.932(30)
5	HIP106843		O9.5IV-V [40]	324.610	56.974	7.41 ²⁷	0.957(33)
6	HIP107164		B0V:pe	325.601	57.736	6.87 [12]	1.044(27)
7	HIP109556	λ Cep	O6.5I(n)fp [40]	332.877	59.414	5.05 [12]	1.62(13)
8	HIP112470		O5.5V((f))+O6V((f)) [39]	341.725	58.084	8.629(18) [24]	0.308(35)
9	HIP17358	δ Per	B5III	55.731	47.788	3.01 [12]	6.32(47)
10	HIP531	10 Cas	B9IIIe	1.611	64.196	5.59 [12]	3.293(89)
11	HIP95700		B3IIe	291.975	20.247	6.87(10) [18]	1.593(93)
12	HIP95818	7 Vul	B5Vn	292.337	20.280	6.326(10) [18]	3.473(48)
13		V1405Cas		351.199	61.187	7.406(11)	0.578(26)
14	HIP93805	λ Aql	B8.5V [16]	286.562	-4.883	3.43 [12]	27.06(51)
15	HIP99431		B9 [8]	302.727	30.790	6.96(1) [18]	2.89(17)
16	HIP100044	P Cyg	B1-2Ia-0ep [36]	304.447	38.033	4.82 [12]	0.32(16) [41]
17	HIP101138	ω^1 Cyg	B2.5IV	307.515	48.952	4.936(9) [18]	2.59(17)
18	HIP102155		B8II-III	310.485	41.717	5.664(9) [18]	2.383(93)
19	HIP103530		B7IVn+B7IV	314.625	50.462	5.90(99) [2]	3.02(50) [41]
20	HIP103871		B3Vn	315.703	45.849	6.486(10) [18]	2.458(58)
21	HIP105891		B7III [19]	321.687	52.899	5.987(9) [18]	6.061(56)
22	HIP2474	13 Cas	B6V	7.855	66.520	6.165(10) [18]	3.773(55)

²⁷No source given in SIMBAD

#	HIP identifier	Object name	Spectral class	RA deg	Dec deg	m_V	Parallax mas
23	HIP15520		B2.5Vn(e) [25]	49.997	65.652	4.85 [12]	6.07(36)
24	HIP100142		B2V	304.707	46.322	6.443(10) [18]	1.177(49)
25	HIP100518		B8V	305.740	39.211	6.733(10) [18]	1.663(58)
26	HIP100574		B2IIIe [38]	305.935	37.476	5.90 [12]	2.656(80)
27	HIP103089	57 Cyg	B5V	313.311	44.387	4.77 [12]	6.21(22) [41]
28	HIP103371		O6.5V((f)z) [40]	314.145	44.925	5.96 [12]	1.063(59)
29	HIP104962		B4IV	318.905	47.974	6.441(9) [18]	2.362(42)
30	HIP107136	π^1 Cyg	B3III [10]	325.524	51.190	4.66 ²⁸	1.89(15) [41]
31	HIP106032	β Cep	B0.5III _s [2]	322.165	70.561	3.23 [12]	4.76(30) [41]
32	HIP2599	κ Cas	B1Ia [25]	8.250	62.932	4.16 [12]	0.73(17) [41]
33	HIP102098 (archive)	α Cyg	A2Ia [27]	310.358	45.280	1.25 [12]	2.31(0.32) [41]
34	HIP4427 (archive)	γ Cas	B0.5IVpe[35]	14.177	60.717	2.39 [12]	5.32(56) [31]
35	HIP63125	α^2 CVn	A0VpSiEu [3]	194.007	38.318	2.88 [12]	28.41(90) [41]
36	HIP67301	η UMa	B3V [26]	206.885	49.313	1.86 [12]	31.38(24) [41]
37		V1405Cas		351.199	61.187	7.073(5)	0.578(26)
38	HIP101383		B4III	308.218	43.192	6.589(9) [18]	1.921(40)
39	HIP102827		B4Ve	312.478	46.661	6.333(10) [18]	2.226(46)
40	HIP115198		B5 [7]	350.003	61.150	6.944(10) [18]	2.552(37)
41		V1405Cas		351.199	61.187	7.967(15)	0.578(26)
42		V1405Cas		351.199	61.187	5.331(6)	0.578(26)

²⁸No source given in SIMBAD

#	Observation Date (UTC time)	$\frac{\text{Int.time}}{\text{s}}$	Airmass	Altitude.	$\frac{b}{\text{km/s}}$	SNR	$\frac{W_{\lambda,D1}}{\text{m\AA}}$	$\frac{W_{\lambda,D2}}{\text{m\AA}}$	$\frac{W_{\lambda,D2}}{W_{\lambda,D1}}$	$\frac{N}{10^{10} \text{ cm}^{-2}}$	$\frac{n}{10^{-3} \# \text{ m}^{-3}}$	Comment
1	2021-04-28	1×1000	1.37	49.4	6.8	32	86(32)	152(45)	1.77(84)	90	1.24(13)	
2	2021-04-27	1×1000	1.82	35.4	5.0	28	326(55)	350(52)	1.07(24)	2000	2.07(44)	
3	2021-04-27	1×1000	1.94	33.1	2.8	36	163(30)	193(27)	1.18(27)	500	5.192(58)	
4	2021-04-27	1×1000	2.48	24.5	ambig.	12	38(31)	64(37)	1.7(1.7)	34	0.1027(45)	
5	2021-04-27	1×1000	2.27	28.3	8.5	8	$4.20(1.2) \cdot 10^2$	$5.1(1.9) \cdot 10^2$	1.21(56)	950	2.95(10)	
6	2021-04-27	1×1000	2.39	25.5	2.0	20	46(45)	70(56)	1.5(1.9)	55	0.1861(59)	
7	2021-04-27	1×1000	2.54	23.5	4.2	36	361(57)	383(43)	1.06(21)	7000	6.8(2.9)	
8	2021-04-28	1×2000	1.77	37.5	---	---	---	---	---	---	---	neg. fluxes
9	2021-04-27	1×1000	2.20	25.1	ambig.	50	19(19)	24(33)	1.3(2.1)	15	0.307(31)	
10	2021-04-27	1×1000	2.03	30.0	≥ 9	22	75(41)	149(44)	2.0(1.2)	75	0.800(24)	
11	2021-04-28	1×1000	1.54	42.6	---	---	---	---	---	---	---	no abs.
12	2021-04-28	1×1000	1.46	45.5	---	---	---	---	---	---	---	no abs.
13	2021-04-28	1×1500	1.44	46.4	---	---	---	---	---	---	---	neg. fluxes
14	2021-04-27	1×1000	2.22	28.1	---	---	---	---	---	---	---	no abs.
15	2021-04-26	1×1000	1.97	32.8	---	---	---	---	---	---	---	no abs.
16	2021-04-26	1×1000	2.55	25.1	11.0	16	261(80)	$4.1(1.1) \cdot 10^2$	1.55(64)	315	0.33(16)	
17	2021-04-27	1×1000	1.45	45.6	4.0	39	126(27)	179(31)	1.42(39)	170	1.427(94)	
18	2021-04-27	1×1000	1.51	44.0	1.95	21	52(32)	78(31)	1.5(1.1)	68	0.525(22)	
19	2021-04-26	1×1000	2.35	26.6	---	---	---	---	---	---	---	no abs.
20	2021-04-26	1×1000	1.97	32.4	---	---	---	---	---	---	---	no abs.
21	2021-04-27	1×1000	1.40	47.7	---	---	---	---	---	---	---	no abs.
22	2021-04-25	1×500	2.04	29.1	ambig.	17	48(43)	114(57)	2.4(2.4)	50	0.611(15)	
23	2021-04-25	1×1000	1.88	31.3	ambig.	46	40(18)	82(19)	2.0(1.0)	38	0.748(49)	

#	Observation Date (UTC time)	$\frac{\text{Int.time}}{\text{s}}$	Airmass	Altitude.	$\frac{b}{\text{km/s}}$	SNR	$\frac{W_{\lambda,D1}}{\text{m\AA}}$	$\frac{W_{\lambda,D2}}{\text{m\AA}}$	$\frac{W_{\lambda,D2}}{W_{\lambda,D1}}$	$\frac{N}{10^{10} \text{ cm}^{-2}}$	$\frac{n}{10^{-3} \# \text{ m}^{-3}}$	Comment
24	2021-04-26	1×1000	1.11	67.2	---	---	---	---	---	---	---	no abs.
25	2021-04-26	1×1000	1.49	44.5	5	12	$1.9(1.0) \cdot 10^2$	$2.1(1.2)e+02$	1.08(85)	200.0	1.078(38)	
26	2021-04-26	1×1000	1.21	58.3	---	---	---	---	---	---	---	no abs.
27	2021-04-26	1×1000	1.41	47.7	22.5	9	$4.5(3.3) \cdot 10^2$	$7.3(5.1)e+02$	1.6(1.6)	510.0	10.26(36)	
28	2021-04-26	1×1000	1.65	39.5	6.8	18	466(96)	$5.0(1.0)e+02$	1.08(31)	2800.0	9.65(54)	
29	2021-04-26	1×1000	1.29	53.3	3.75	11	121(80)	$1.7(1.1)e+02$	1.4(1.3)	170.0	1.301(23)	
30	2021-04-26	1×1000	1.39	48.3	3.7	45	144(31)	195(36)	1.36(39)	230.0	1.41(11)	
31	2021-04-22	1×577	1.36	47.8	ambig.	106	14.2(9.7)	65(11)	4.6(3.2)	30.0	0.463(29)	
32	2020-11-07	1×900	1.07	66.9	---	---	---	---	---	---	---	calib. issue
33	2020-08-31	1×300	1.09	66.3	8.5	54	375(41)	479(32)	1.28(16)	700.0	5.24(73)	
34	2020-09-01	1×300	1.02	78.4	---	61	34(15)	137(24)	4.1(2.0)	70.0	1.21(13)	complic.
35	2021-05-08	1×1000	1.39	43.5	---	---	---	---	---	---	---	no abs.
36	2021-05-07	1×600	1.02	77.9	---	---	---	---	---	---	---	no abs.
37	2021-06-02	5×1200	1.66	38.7	10.5	18	557(99)	662(94)	1.19(27)	1430.0	2.68(12)	
38	2021-04-25	1×1000	2.40	26.3	---	---	---	---	---	---	---	no abs.
39	2021-04-25	1×1000	1.94	32.9	---	---	---	---	---	---	---	no abs.
40	2021-04-27	1×2000	2.20	28.5	---	---	---	---	---	---	---	file not usable
41	2021-04-14	3×1600	2.32	24.6	11.8	21	$5.9(1.0) \cdot 10^2$	$7.2(1.0)e+02$	1.21(27)	1350.0	2.53(11)	
42	2021-05-10	3×2000	2.25	27.7	12.5	18	$6.3(1.0) \cdot 10^2$	$7.6(1.1)e+02$	1.21(26)	1450.0	2.72(12)	

To ensure that the data comes with a certain level of quality, we have gone through the whole data set several times, checking whether the calculated values here make sense, like as if the respective Na I intensity ratios make sense, for instance.

8 Discussion

By now, we discussed which steps it took us to obtain the echellograms and discussed how we extract the spectra out of them. Furthermore, we explained what it takes us to measure the equivalent width W_λ and other, simple observational parameters.

Now, taking the data set, we can deduce some more numbers, like the column density N , and as a step further, the mean particle densities \bar{n} . The resulting data cube as its whole also forms an essential part of this thesis.

In the following chapters, we will interpret some of the results and numbers, presented in the most recent chapter (see table 2).

8.1 Calculation of Column Densities

As we have discussed in the theory part, we can compute the line of sight column densities N , given the measured equivalent widths. Application of the curve of growth analysis, as it is discussed in chapter 4.5.6, on every single pair of sodium absorption leads us to the respective column density.

In this regard, one must not forget that this is a theoretically derived quantity, considering that it can not be measured directly like the equivalent width W_λ . Therefore, the results rely on assumptions and idealizations, mentioned in the theoretical background part.

The following figure shows a histogram, depicting the distribution of column densities for the observed set of stars²⁹.

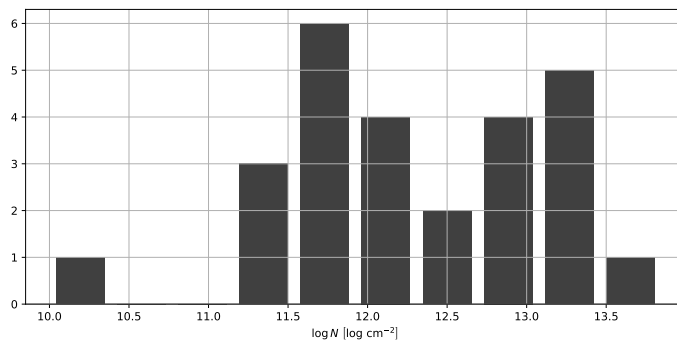


Figure 8.1: A histogram, presenting the distribution of the column densities N for the observed stars.

In fact, it is hard to correlate the column densities for stars, all scattered across the whole sky. However, the distribution should give us an idea, of which magnitude one can expect the values. Additionally, and concerning the whole data set, we indeed can conclude a detection limit of about $\sim 10^{10} \text{ cm}^{-2}$ for the column densities, we achieved with our observations. We want to mention, this number represents a statistical finding and has no analytical reasoning in this context.

Of course, the exact value differs and depends on many quantities like the SNR, the spectrograph's resolving power, and the intrinsic absorption width³⁰, for instance.

²⁹Due to the logarithmic scale, only the data for stars with a non-zero equivalent width is included.

³⁰As mentioned in the theory, for the ISM absorption the Doppler parameter b is normally very small, making the absorption lines comparably easy to detect and to measure. However, the broader the line gets, the larger the impact of the continuum level's noise becomes.

8.2 Computation of Mean Particle Densities

The column densities N of Na I along the line of sight of stars is certainly an interesting quantity. However, it is not normalized to the distance of the illumination sources. A nice and descriptive quantity is the average line of sight particle density \bar{n} .

With the help of equation (10), we are able to convert the column densities N into \bar{n} . The parallaxes, as given in table (2), were used to compute the \bar{n} values, also to be found in table (2).

Referring to figure (7.2), in which the marker sizes illustrate the respective line of sight particle densities, we can see how stars, particularly close to some nebulosities, show intensely high \bar{n} values.

In the very framing of figure (7.2), we can identify a region³¹ with dense ISM, close enough, enabling us to observe some bright stars, and using them as probes in this very ISM cloud.

In our observations, the stars in the line of sight of the Milky Way's "Great Rift"³² predominantly did not show strong ISM features. This allows two possible explanations:

1. The major and the densest parts of the cloud are located beyond the stars we observed here.
2. The observed stars lie within the clouds but do not contain any neutral sodium that can absorb light in the spectra of the respective stars.

The latter conclusion seems a little drastic since other, because more advanced, all-sky observations show similar results regarding the ISM's composition so that we can assume, in first-order approximation, an even mixture of neutral sodium in the ISM. However, its fraction with approximately ~ 0.22 ppm [22, p. 340]³³ is almost negligible.

They are large-scale structures, which we can also see from exceptionally large distances. We can compare this to the largest-scale intragalactic dust clouds as shown in the picture (4.1b) of the Triangulum Galaxy (Messier 33). The figure can be found at the very beginning of this thesis. We can make these dust clouds even visible in other galaxies, giving us an idea, how large they are, and what order of magnitude the spacing between them can be.

Therefore, there could also be a large void between the solar system and the dust cloud, making almost no Na I absorption visible up to that point. Furthermore, the brightest of the stars, visible in our skies, are usually close to the solar system, having not more than a couple of kiloparsecs distance.

As an outlook in this regard, it would be interesting to probe along the line of sight with a row of stars to determine the boundaries of this cloud.

³¹namely the North America Nebula (NGC 7000) and its vicinity

³²The large and dusty region with only a very little amount of stars visible.

³³For this number, the source refers to the interstellar clouds in the ζ Oph region. However, we assume this number to be representative to some extent for the whole galactic ISM.

9 General Scientific Context

Now, that we have reduced our data set far enough, we can compare our results to literature values. In this chapter, we aim to find correlations between our data and data sets, provided by external sources.

9.1 Extinction Maps and their use for Intra-/Intergalactic Observations

As already discussed in the theoretical background, the presence of ISM affects several photometric, as well as spectroscopic measurements of distant objects. Therefore, a map showing the distribution of ISM surrounding us is of great interest. With an expected value for reddening and extinction, one can either correct or explain misleading results or unexpected phenomena.

Yet, not only two but also three dimensional ISM distribution models are available. These are compiled of thousands or millions of single measurements. By measuring the color index of stars, and comparison of their expected values, one can reconstruct the distribution of interstellar dust and gas in a first-order approximation, even though there exists always a certain uncertainty. The enormous amount of data, released with Gaia DR2, enables us, furthermore, to also probe along the lines of sight, taking the star's distances into account.

A highly cited paper in this regard is the all-sky extinction map, published by Schlegel, Finkbeiner & Davis [34]. They managed to create a relatively high resolution (\sim arcmin) all-sky map, filled with the respective extinction at any coordinate on the sky. They combined data of the IRAS satellite and COBE/DIBRE. The following figure presents a glance at the resulting all-sky map in galactic coordinates, making the Milky Way visible as the bright source as the equator in this projection.

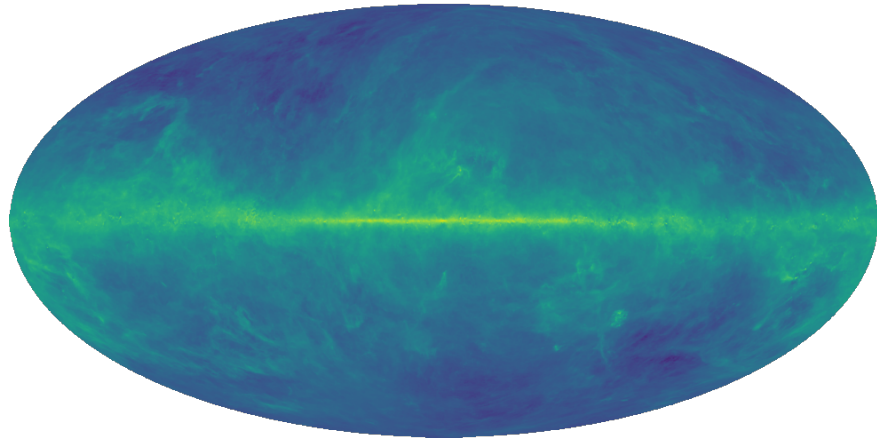


Figure 9.1: The SFD all-sky extinction map in Mollweide projection. One can see the overabundance of ISM, causing the most intense reddening along the galactic equator. The map arises from the data compiled by [34] and is being accessed through the LAMBDA-Data Products web service, provided by NASA. [29]

9.2 H I 21cm All-Sky Map

A different way to estimate the abundance of ISM and interstellar dust is to figure out where the most interstellar hydrogen abundance is to expect. If we assume an almost constant gas to dust

ratio in the ISM, the abundance of dust increases as the amount of hydrogen increases. Therefore, as we detect strong emission of atomic hydrogen, we expect dense regions of ISM in this specific direction. Just like one can do for the extinction, one can also compile a map of H I emission in this regard, which is presented in figure (9.2).

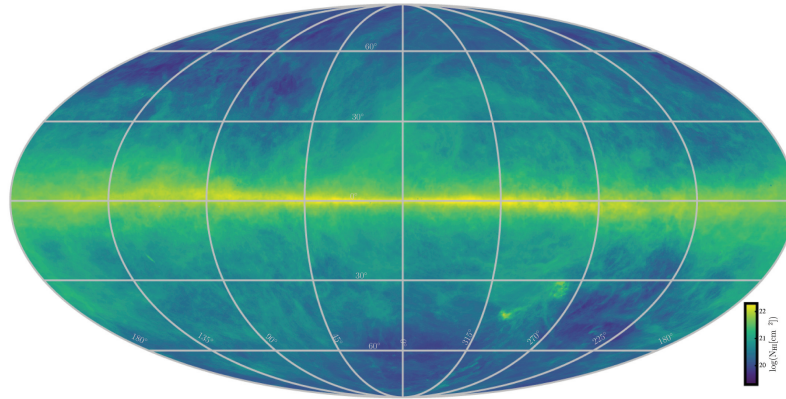


Figure 9.2: Mollweide projection in the galactic frame, depicting the distribution of the H I 21 cm radiation, emitted by the ISM. The image was taken from source [6].

The data refers to the signal intensity at the 21 cm line of neutral hydrogen. This line emerges from the hyperfine transition³⁴ of the atomic hydrogen.

Another beneficial tool that we will later make use of is the *HI Profile Search*³⁵, provided by the ARGELANDER INSTITUTE OF THE BONN UNIVERSITY. By inserting the respective sky coordinates, either in the equatorial or galactic frame, we can query the radial velocity profiles of the H I signal.

As mentioned, we use neutral hydrogen as an indicator for interstellar dust. Therefore, if we observe ISM absorption in Na I, we should be able to discover a similar line profile as for the H I in the same line of sight. The following figure shows an arbitrary line H I line profile for low galactic latitudes.

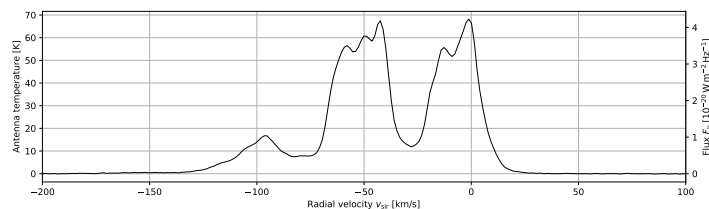


Figure 9.3: The H I 21 cm line profile for the ICRS sky coordinates RA: 23h 24m 48s; DEC: +61deg 11m 15s (the direction of V1405 Cas). The data were retrieved from the H I profile search

Here, we can see that those line profiles can, indeed, get comparably complex, which may be due to the superposition of independent interstellar clouds along the same line of sight as we have already discussed and visualized with figure (4.11).

9.3 Comparison of ISM Absorption Lines with H I Line profiles

As we already discussed in the most recent chapter, the abundance of cold interstellar hydrogen can act as a tracer for ISM Na I presence. As we compare the radial velocity profile of the H I

³⁴A spin-flip of the hydrogen's only shell electron causes the emission at this specific wavelength.

³⁵The data basis of this online tool is the data from the HI4PI survey [6]. It is a concatenation of two data sets, taken as part of the EBHIS (Effelsberg Bonn H-I Survey) [43] and GASS (Galactic All-Sky Survey), covering complementary parts of the sky. [21]

radio emission with the respective radial velocity-dependent absorption of the Na I, we might be able to correlate these two quantities.

Since we did not gather H I radio emission data during the presented observation, we access some archival data from the “H I Profile Search” provided by the ARGELANDER INSTITUTE OF THE BONN UNIVERSITY. The principal ideas for this tool were already laid out in chapter 9.2.

With the help of a Python script, we can superimpose the H I emission data with the Na I Absorption profile, for which we have taken the data from this observation. For instance, a respective output can look the following way, as shown in figure (9.4).

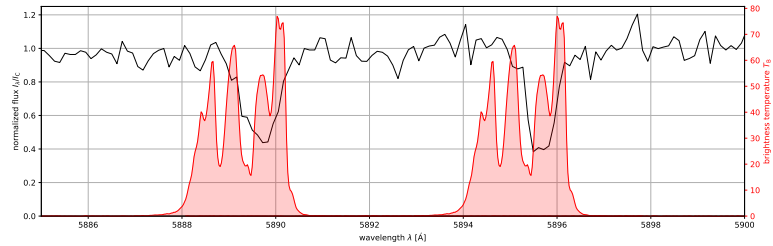


Figure 9.4: Given a reference wavelength, with the help of the Doppler Formula, we can convert any wavelength into a radial velocity. In a second step, we can, therefore, compare the radial velocity H I intensity profile with the Doppler-shifted absorption profile of the Na I absorption. In this figure, such an example plot is shown for the star HIP 103371.

A compilation of all H I plots can be found in the appendix on the plot sheets. They are attached to the very end of this thesis.

10 Peculiar Spectra

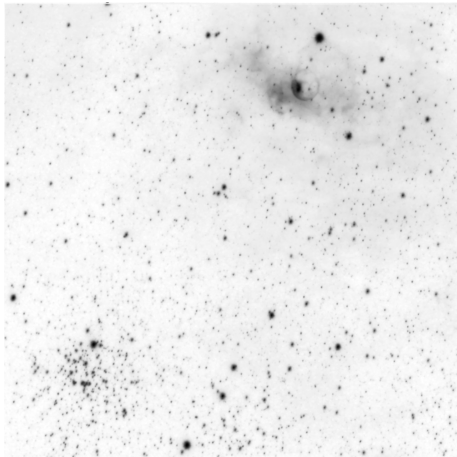
In the recent chapters, we have seen that a lot of different stellar systems were observed. We found that some of these systems show peculiarities in their spectra, which we want to discuss in more detail in this chapter.

10.1 V1405 Cas

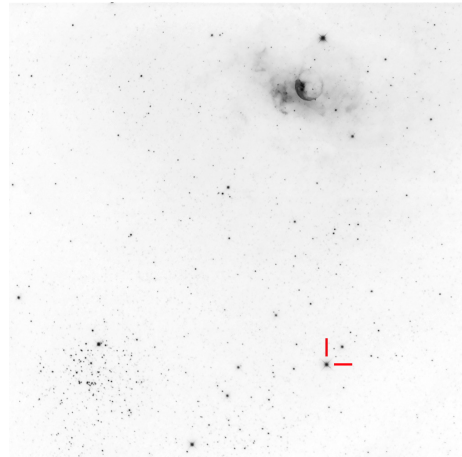
Among all observed targets, the certainly most interesting one is the variable star system V1405 Cas which particularly became interesting as of March 18, 2021; It is the date of discovery for it being a nova.

Lying in the constellation Cassiopeia, and positioned almost perfectly on the galactic equator at exceptional low galactic latitude $b \approx 0\text{deg } 03\text{m } 04\text{s}$, it allows us a deep insight into the galactic disk and the ISM in between. The respective multiple star system can be found close to the open cluster³⁶ Messier 52 and the H II region NGC 7635³⁷ in the sky.

The nova itself was discovered by the Japanese astrophotographer Yuji Nakamura in four images, taken on March 18, 2021. Each was exposed for just 15 seconds with a standard camera lens at a focal length of 135 mm. [9] As he compared his images to past ones, he discovered a new source of light with 9.6^{mag} [30]. It later turned out to be the nova Cas 2021. The following images show the same field of view but at different dates and have been taken by ourselves.



(a) 2020-08-19: This image has been taken with an 80 mm apochromatic refractor telescope with a focal length of 380 mm. To match the other picture's field of view, this image has been cropped and stretched, leading to slightly blurred stars in the image itself. It is a stack of 20 images, each with an exposure time of 3 minutes, resulting in an integration time of one hour in total.



(b) 2021-07-12: This image was taken with an 8" Ritchey Chretien reflector telescope at a focal length of ~ 1100 mm. This image is the result of a stack of 94×3 min exposures, compiling to a total integration time of 4.7 hours. The bright point source in the lower right is the nova.

Figure 10.1: Comparison of two images, both covering the same field of view, containing the nova. By coincidence, this field of view was imaged multiple times. Initially because of the other adjacent deep-sky objects M 52 and NGC 7635. One can clearly see the difference between both images: The nova is flaring in the second of these images only. The second picture was taken after the nova's ignition.

One can see the flaring star (actually the Nova) in the right image as it brightened dramatically over a couple of days.

³⁶For a further visual description, one can find a finder chart, generated with the AAVSO web tool in the appendix of this thesis.

³⁷It is also listed as Caldwell 11, and known under its trivial name: The "Bubble Nebula"

Coincidentally, the star system also has been listed by the Gaia astrometry satellite as the source **Gaia EDR3 2015451512907540480**, which also measured a parallax of the star system of (0.578 ± 0.026) mas³⁸, therefore, leading to a distance of (1730 ± 78) pc. This means, as we observe the stars spectrum, we automatically probe roughly 2 kpc deep into the Milky Way's interior.

As V1405 Cas erupted as a nova, it automatically shows us to be a highly dynamic star system. Of course, the spectral fingerprint of the system, therefore, evolves, and changes over time, as the white dwarf in the system ejects dominant parts of its hydrogen shell into space. As the ejecta cools down, some optical transitions of elements become visible, and observable to astronomers on Earth.

These dynamics help us to better distinguish between spectral features belonging to the star system, also showing morphological dynamics over time, and absorption of the ISM mostly unaffected by the system dynamics.

In the scope of this thesis, many spectra of this star system have been taken with particular interest to the Na I doublet. We compiled a grid of spectra³⁹, covering the same spectral region, over months. During May, a heavily blue-shifted new pair of sodium lines appeared, making it identifiable as part of the star system itself. It was also about the same time, when the nova's brightness reached its absolute maximum, yet. As the star system's expanding shell cools down, it might have enabled neutral sodium to form so that we can observe its absorption in front of the illumination source.

Interestingly enough, the initial sodium absorption (almost unshifted in this regard), which has been found since the first observation, remained stable in its shape and position, suggesting it may originate from the ISM. To further support this assumption, we can, as described in chapter 9.2, compare the H I radio emission profile along the line of sight, as it has been done in figure (10.2).

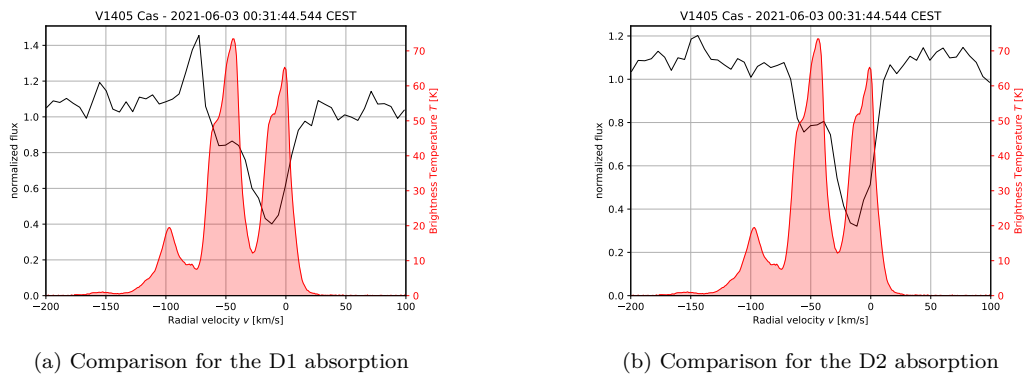


Figure 10.2: Comparison plot between the H I radial emission profile (data taken from the H I profile search), and the Na I absorption, measured with our setup.

We can see how the emission and absorption match towards higher velocities to some extent. We can also make out a region with H I emission, where no absorption of Na I is measured. However, emission of H I without Na I absorption is explainable in this regard and can have different reasons:

1. There are several independent ISM clouds along the line of sight, and the nova itself is too close so that its finite distance does not allow us to probe through all of them. This explanation is in harmony with what we already have discussed in a previous chapter, dealing with the formation of complex line profiles, and particularly in figure (4.11).
2. The H I side emission peaks are far smaller, and, therefore, the Na I absorption could be too light to be detected with our setup.

³⁸as given in the Gaia archive

³⁹These can be found in the appendix in chapter 15.

Of course, this peculiar object provides us much more room for scientific investigations than what we could cover here in the scope of this thesis and is indeed a promising subject to further and deeper research.

10.2 P Cygni - HIP 100044

P CYGNI is a luminous blue variable (LBV) star in the constellation CYGNUS. LBV stars are among the most massive and hot known stars in their last stages, before they end up as supernovae. In P CYGNI's spectrum, we can find its characteristic spectral features, following the so-called *P Cygni profiles*, as we can see in figure (10.3).

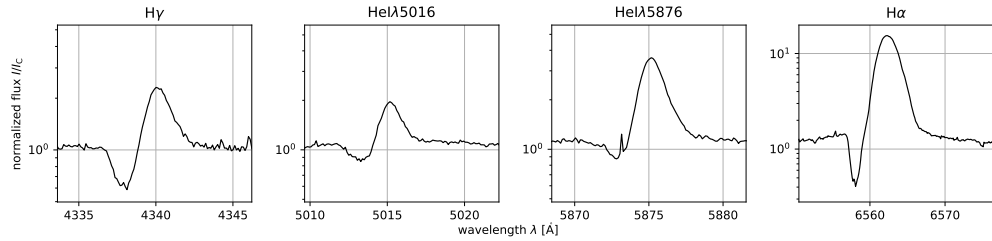


Figure 10.3: Extraction of some dominant P Cygni lines in the spectrum of P Cygni. All of these plots are made of data that was taken with the OST.

They define the prototype for many of their kind. Since they emerge from the absorption and re-emission of light in an expanding shell of material (see figure 10.4 for visual guidance), such features can also be found in a variety of other star systems, similar in that manner. In the case of LBV stars, the strong material outflows are caused by the severe stellar winds of those stars.

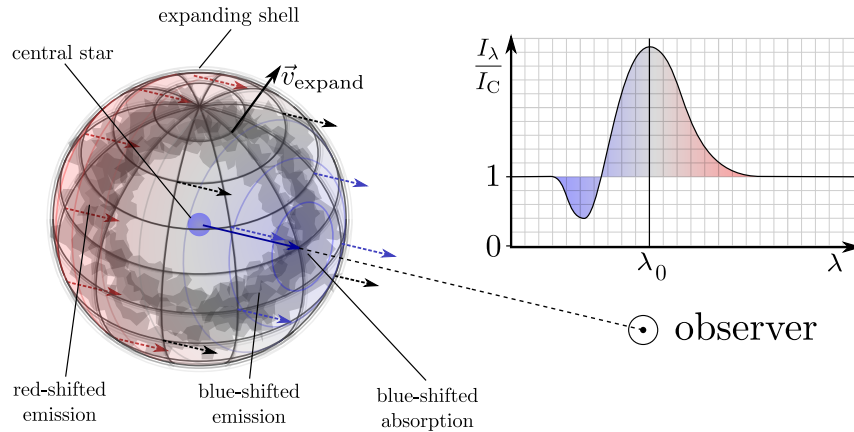


Figure 10.4: This sketch depicts the principle of how P Cygni profiles come into existence when from expanding shells surrounding an illumination source. The material flow along the line of sight toward the observer causes a blue-shifted absorption. The rest of the shell redirects some light to the observer, re-emitted by itself, whereas the light we receive this way has many radial velocities mixed. Due to the large star's distance, we usually cannot resolve its shell spatially. This leads the emission peak to appear severely Doppler broadened, as our sensor collects all the incoming light.

Since their origins are of a rather general nature, P Cygni profiles, therefore, can be found in non-LBV star systems too. A very fitting example is V1405 Cas, which we have covered a chapter before more in detail. A look on its spectrum also lets us see these profiles, telling us, how the outer shells of its host star violently get ejected into space.

Besides the specific P CYGNI peculiarity, it also shows strong ISM absorption. Due to its high luminosity, we can observe stars like this, even though they lie far away from our solar system. This allows us to probe deep into space and detect noticeable amounts of Na I absorption. In the case of P CYGNI, we measured Na I absorption equivalent widths of (261 ± 80) mÅ for the D1 line, and (410 ± 110) mÅ for the D2 line, respectively [table 2]. The Line profiles are shown in figure (10.5).

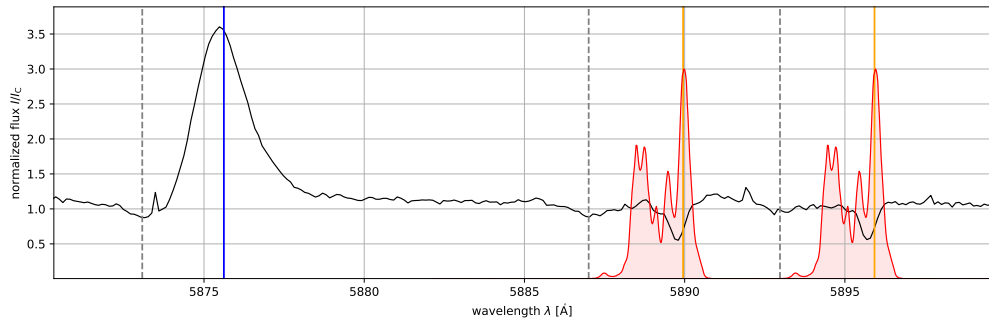


Figure 10.5: Close-up of the Na I absorption in P Cygni's spectrum, most likely caused by interstellar Na I. A comparison plot (red curve) for the neutral hydrogen 21 cm emission is superimposed. Along with some markers for the rest-wavelengths of D1 and D2 (orange), and He I (blue), also markers for their blue-shifted siblings are drawn. We believe those features to be a product of the star's expanding shell, as these lines appear widely broadened. We can even suspect another pair of Na I lines, exhibiting P Cygni profiles. However, their broadening and weakness make them hard to even identify. Nevertheless, we can see, how the ISM Na I absorption is embedded in such P Cygni profiles (most distinct for the D2 line, because it is intrinsically stronger than the D1 line). Interestingly, the Doppler shift matches for both Na I absorption lines, where each is blue-shifted with (-150 ± 10) km/s, with respect to the rest frame, whereas the He I absorption is shifted with (-130 ± 10) km/s.

With the help of a curve of growth analysis, we determined a column density of roughly $3.15 \cdot 10^{12}$ particles/cm² [table 2] for the ISM absorption part. Also taking the stars distance into account, we conclude a mean particle density along the line of sight of about $(0.33 \pm 0.16) \cdot 10^{-9}$ particles/cm³ [table 2]. Again, one must not forget, even though we cannot give an accurate uncertainty for the column density, its relative error should be at least in the same order of magnitude as those for the equivalent widths which is about $\sim 25\%$.

11 Conclusion

In the scope of this thesis, we took a set of spectra from 37 different star systems. We retrieved the data through spectroscopic observations with the OST and the BACHES spectrograph on the one hand and used archival data for two more stars on the other hand.

Due to the time of the year, where these observations took place, the visibility of the galactic equator was rather sub-optimal and did not rise high up in the sky during the night. Therefore, most of these can be found in the constellation Cygnus as the respective portion of the sky that rose up high during late-spring nights.

In the end, we were able to compile a catalog of stars, with some of them exhibiting ISM absorption features. Out of the 39 stars we observed, 22 stars have shown measurable amounts of interstellar sodium. However, the real number could also be higher, if we consider that for some stars, the observation data turned out to be unusable because of corrupted calibration data, or spectra files.

Also, one must not forget, we chose some stars intentionally at high galactic latitudes to have comparison spectra for stars, not expected to show ISM features, which they, indeed, did not, but belonging to the same spectral type.

Nevertheless, a large fraction of stars *do* show ISM features in their spectra, telling us, the line of sight reddening, as we set it as a condition for potentially promising stars in this regard, is a good indicator for expectable ISM absorption in the spectra of stars. As just another requirement, they have to be positioned far enough, to let us probe along enough path through the ISM, and to cause detectable absorption.

Furthermore, we can conclude, for observations like these, the OST observatory provides an observational setup, just powerful enough, to provide us spectra of the brightest stars with reasonable SNR, enabling us the identification of ISM absorption. In our case, the SNR of usable spectra was in the range of about $10 \sim 30$ with a few outliers in both directions. We found out that even though the resolving power of BACHES with barely $R \approx 20\,000$ is not sufficient to fully resolve the ISM absorption lines, with a dedicated curve of growth analysis we were able to deduce the respective column densities.

Nevertheless, with the data we were dealing with, many of the column density's values N became imprecise and vague due to large uncertainties in the equivalent widths W_λ , forming an essential part to perform the curve of growth analysis.

As the very result of this thesis, we can present a generous catalog of stars with and without ISM absorption in their spectra, ATTITUDE - a Python routine, suitable to plan observation nights on observing ISM absorption affected stars, and another Python program (PySPAN) with a complex user interface to measure equivalent widths, along with performing the respective curve of growth analysis for the Na I doublet.

With the preparatory work in the scope of this thesis, we now have convenient tools for additional and extended surveys like this one. Furthermore, it encourages us, if the time and weather permits, to perform further investigations, also covering other promising parts in the sky, like the parts of the winter Milky Way in the region Orion and Taurus. It might be also a good idea to extend, or even improve the catalog, presented here. We have seen, how some large value uncertainties are the result of noisy spectra, even though they partially show very interesting results.

There are, most certainly, many discoveries to be made even with our Overwhelmingly Small Telescope in Golm in the future, and this thesis should give us an idea of what our setup is capable of. However, here, we are just grazing the surface of what is possible, and there is a lot more to come. - For sure.

Acknowledgments

First of all, I want to thank PROF. DR. PHILIPP RICHTER and DR. MARTIN WENDT for their time and effort that it took them to supervise me during the writing process of this thesis. I am grateful they took the time to proofread this - rather lengthy - thesis, several times.

In addition, I am grateful for their recommendation of this topic which allowed me the chance to conduct astrophysical observations at our local OST observatory.

Additionally, I want to particularly thank DR. RAINER HAINICH for being available at literally *any* time. This also includes assistance during the middle of the night, whenever problems occurred in the observatory.

Finally, I would like to thank my family for helping and motivating me during the writing process of this thesis.

Appendix

12 Python Code

12.1 ATTITUDE (Automatized Tool To Identify Tons of Usable Stars with D-line absorption and Extinction) [v0.1.1]

The preselection of stars, suitable for our observations, was partly automatized and carried out with the help of a Python routine that has been written and fully developed by us. It started as a little script that was written on the fly but turned out to become a handy tool as we have gone through more and more observation runs.

This very routine will be presented in more detail in this chapter. It should give us an overview, as well as an insight into the internal concepts, also from a technical perspective.

In the scope to establish such an observation like it is presented here, as a possible observation for the master lab course at the University of Potsdam, among some others, a convenient user interface is favorable. It should stay in continuous “contact” with the user and inform them if any input is mistakenly formatted or does not make any sense. A comprehensive exception handling is also included with a respective user communication interaction.

In the ongoing text, we will break down the working principle including the most important subroutines of the program to a very basic level.

As a reminder: The principal idea is laid out in more detail in chapter 6.1.4. Nonetheless, we want to mention this here once again briefly:

Given a set of stars, the idea is to filter some potentially promising candidates, most likely to show interstellar extinction features in their spectra with respect to certain selection criteria already justified in section 6.1.4. Yet, different distances of the stars themselves are not considered as a filter criterion, even though more distant stars are more likely to show ISM absorption since the integration distance is longer, respectively. However, this helper tool can be extended and adjusted with more filter steps, like this, accordingly.

At the very beginning, the user can find a section in which they can set certain parameters, referring to the selection criteria, and therefore adjust the strictness of these. Adjustments might become necessary, as either no stars at all or an overwhelming large set of stars is suggested by the program. The meaning of each is described in the comments immediately following the code. Also, some formatting examples are given. As we comment on the code in the ongoing text, we do not want to include the actual comment lines in the code snippets.

```
obs_site = [  
    +52.409184,      # latitude (north is positive)  
    +12.973185,      # longitude (east is positive)  
    39               # height (in m)  
]  
obs_time = ''  
  
min_alt = 20  
max_mag = 7  
max_b_v = -0.1  
min_E_b_v = 0.4  
stars_catalog_file = 'hip_newred.fits'  
all_sky_extinction_plot_filename = 'all_sky_plot.pdf'
```

The following quantities are defined in the upper code lines

<code>obs_time</code>	<hr/> This variable defines the time of observation. It should be given as a string, containing the time in ISO-Format that later can be converted into an <code>astropy.time.Time</code> instance. The time value itself should be given as UT+0. If the string is left empty, the current system time is taken.
<code>min_alt</code>	<hr/> Defines an object's minimum altitude above the horizon to get considered in the end.
<code>max_mag</code>	<hr/> Defines the lower brightness limit, a star must have, to be considered as sufficiently bright enough to provide a reasonable amount of flux.
<code>max_b_v</code>	<hr/> Defines the maximum observed $B - V$ color index a star can have. This criterion identifies stars, being not how enough to ionize all neutral sodium in their stellar atmosphere, and, hence, to let the intrinsic Na I absorption vanish.
<code>min_E_b_v</code>	<hr/> Defines a threshold, characterizing the line of sight color excess. Since neutral sodium is a characteristic element in interstellar dust, its presence can be indicated by the interstellar reddening, suggesting the presence of Na I.
<code>stars_catalog_file</code>	<hr/> This is a path to the (in our case) Hipparcos catalog. In general, it is not necessary to adjust the filename here, as long as the <code>*.py</code> script file is located in the same directory as the catalog file. It provides us the list of stars up to an apparent magnitude of $\sim 11^{\text{mag}}$.
<code>all_sky_extinction_plot_filename</code>	<hr/> This variable defines the filename of an output file. By default, after every run through the program, it creates an all-sky plot with all remaining stars before the reddening filter is applied. If the string is left empty, no plot will be created.
<code>all_sky_extinction_plot_filename</code>	<hr/> This variable defines the filename of another output file. By default, after every run through the program, it creates a graph, showing the filter history, and how many stars are filtered out after every step. Here, the user can identify, whether any of the specified thresholds are too strict and can change is accordingly. Just as for its predecessor: If the string is left empty, no plot will be created.

```
import matplotlib.pyplot as plt
from matplotlib
import cm import numpy as np
from astropy.io import fits
import astropy.coordinates as coord
from astropy import units as u
from astropy.table import Table
from astropy.time import Time
from dustmaps.sfd import SFDWebQuery
```

This code section includes all packages, necessary to run the script.

NOTE: A dependency of the `dustmaps` package is `healpy`, of which currently a pre-compiled version only exists for Linux OS.

```
class bcolors:
    HEADER          = '\033[95m'
    OKBLUE          = '\033[94m'
```

```

OKGREEN           = '\033[92m'
WARNING           = '\033[93m'
FAIL              = '\033[91m'
GRAY              = '\033[90m'
ENDC              = '\033[0m'
BOLD              = '\033[1m'
UNDERLINE         = '\033[4m'

```

This section defines a class, containing ANSI color strings, utilized to recolor the terminal's output. In fact, this is just a convenience feature to make the user interface more appealing.

```

star_list_len = []
if obs_time == '':
    obs_time = Time.now()

try:
    Time(obs_time, format='iso')
except:
    print(
        ... error message ...
    )

```

In this step, the program starts to read and interpret some user inputs, starting with the time string. If the time string is left empty, it assumes to work with the current system time. It further checks for every input, whether a reasonable has been entered, and prompts the user with an error message if this is not the case. Because the error prompts can get somewhat lengthy, we abbreviate the `print` command in this regard. In the very first line of the upper code block, a variable `star_list_len` is being initialized. This is an empty standard python `list` instance, later containing the star list's lengths, after every filter step. This way, we can keep track of how many stars are excluded after any filter iteration.

```

try:
    AltAz = coord.AltAz(
        location = coord.EarthLocation(
            lat = obs_site[0],
            lon = obs_site[1],
            height = obs_site[2]
        ),
        obstime = Time(obs_time)
    )
except:
    print(
        ... error message ...
    )

```

Here, an `astropy.AltAz` coordinate instance is being created, later helpful to transfer the respective ICRS coordinates, as given in the catalog file, into the altitude-azimuth frame, interesting for the observation planning.

```

try:
    allstars = Table(fits.open(stars_catalog_file)[1].data)
except:
    print(
        ... error message ...
    )
try:

```

```

    allstars.remove_columns(['ic', 'ra_rad', 'de_rad', 'pm_ra', 'pm_de', \
'e_ra_rad', 'e_de_rad', 'e_pm_ra', 'e_pm_de', 'f1', 'f2', 'nc', 'ntr', \
'u3', 'u4', 'u5', 'u6', 'u7', 'u8', 'u9', 'sn', 'so', 'var', 'u1', 'u2', \
'u10', 'u11', 'u12', 'u13', 'u14', 'u15', 'v_i', 's_hp', 'va'])
except:
    print(
        ... error message ...
    )
...

```

Here, the catalog file's content is being extracted and forwarded to an `astropy.table.Table` instance. The respective file, initially, contains a lot of columns, not necessary in this context. Hence, they are deleted from the table. This also shrinks the output drastically in the end.

```

star_list_len.append(len(allstars))

```

In this simple step, the first entry is appended to the `star_list_len` list. Yet, it solely contains the length of the whole Hipparcos catalog or the respective length as provided by the unfiltered star catalog.

```

...
filter_mag = allstars['hp_mag'] <= max_mag
allstars_filtered = allstars[filter_mag]
print(
    ... info message ...
)
star_list_len.append(len(allstars_filtered))
...

```

In this snippet, we can see how the filter with respect to the maximum allowed apparent magnitude is applied. It creates a list `filter_mag`, containing Boolean entries only, acting as some mask to sort for matching entries in the `allstars` table. After this step, a new list is being created, now, only filled with stars, meeting the minimum brightness requirement.

```

filter_b_v = allstars_filtered['b_v'] <= max_b_v
allstars_filtered = allstars_filtered[filter_b_v]
print(
    ... info message ...
)
star_list_len.append(len(allstars_filtered))

```

In the same manner, as the step before, the color filter is applied to the remaining stars.

```

list_alt_az = coord.SkyCoord(
    ra = allstars_filtered['ra']*u.deg,
    dec = allstars_filtered['dec']*u.deg,
    frame = 'icrs'
).transform_to(AltAz)

allstars_filtered.add_columns(
    [list_alt_az.alt, list_alt_az.az],
    names = ['alt', 'az']
)

```

Now, that the program already sorted out many uninteresting candidates, it can proceed with the star coordinates transformation into the altitude-azimuth frame. The values of these coordinate tuples are then saved in two lists and eventually added as two new columns to the main data grid `allstars_filtered`.

```

filter_alt          = allstars_filtered [ 'alt ' ] >= min_alt
allstars_filtered  = allstars_filtered [ filter_alt ]
print(
    ... info message ...
)

star_list_len.append(len(allstars_filtered))

```

Given the respective altitudes, the next filter step can take place: Sorting out stars with too little altitudes, not making it possible for an observer to do spectroscopy on them. The routine checks for all stars, whether their altitudes exceed the threshold value, specified by the user in the beginning. Again, a new entry to `star_len_list` is appended.

```

try:
    allstars_filtered.add_column(SFDWebQuery()(coord.SkyCoord(
ra=allstars_filtered [ 'ra ' ]*u.deg ,
    dec=allstars_filtered [ 'dec ' ]*u.deg ,
    frame='icrs')),
    name='E_b_v'
)
except:
    print(
        ... error message ...
    )

```

In the next step, the line of sight extinction data is obtained through a web query, made possible with a Python API provided by the `dustmaps` package. By inserting the coordinates of interest, the program queries the SFD ([34]) data cube and returns a list of extinctions, which are then added as a new column to the data table.

```

try:
    allstars_filtered.add_column(
        coord.get_constellation(
            coord.SkyCoord(
                ra      = allstars_filtered [ 'ra ' ]*u.deg ,
                dec     = allstars_filtered [ 'dec ' ]*u.deg ,
                frame   = 'icrs'
            ),
            short_name = True
        ),
        name='constellation'
    )
except:
    print(
        ... warning message ...
    )

```

As an additional convenience feature, `astropy` is also capable of identifying the constellation, where the respective entries in the star list are located in the sky. This helps for orientation, since all stars in the catalog are primarily just numbers without any reference, even though one could coarsely think of their positions on the sky using their ICRS coordinate tuples.

```

plt.figure(dpi=100)
plt.scatter(
    allstars_filtered [ 'ra ' ]/15 ,
    allstars_filtered [ 'dec ' ] ,

```

```

c=cm.get_cmap('coolwarm', 20)(allstars_filtered['E_b_v']),
s=20*0.5**allstars_filtered['hp_mag'],
linewidths=0,
cmap='coolwarm'
)

```

The upper code block creates an all-sky plot of the remaining stars up to this moment. They are color-coded with respect to their line of sight reddening E_{B-V} . However, no stars are being filtered after according to this quantity yet.

```

plt.xlim(24,0)
plt.xlabel('right ascension [h]')
plt.ylim(-90,90)
plt.ylabel('declination [deg]')
plt.grid(True, linewidth=0.25, c='black')
plt.title('Filtered stars before extinction')
plt.tight_layout()

```

These lines provide reasonable formatting for the mentioned all-sky plot. In this regard, the RA angles are converted into the hour-angle scale, leading to an x -range from 0 to 24. Furthermore, the x -limits are switched, beginning with the upper, and ending with 0 as the lower limit. In order to map the sky correctly, the RA values need to descent from left to right, which is achieved with this.

```

try:
    plt.savefig(all_sky_extinction_plot_filename)
    plt.show()
    print(
        ... info message ...
    )
except:
    plt.close()
    print(
        ... warning message ...
    )

```

After the plot has been created, a new file with the filename `all_sky_extinction_plot_filename` is created at the beginning of this section.

```

filter_E_b_v = allstars_filtered['E_b_v'] >= min_E_b_v
allstars_filtered = allstars_filtered[filter_E_b_v]
print(
    ... info message ...
)

star_list_len.append(len(allstars_filtered))

```

Once more, the data goes through another filter: This last time, the stars are being sorted with respect to their line of sight reddening. Only stars, showing E_{B-V} values higher than the minimum value `min_E_b_v`, specified by the user, at the beginning, will be considered at the very end.

```

try:
    plt.figure()
    plt.plot(
        [ ... x labels ... ],
        star_list_len
    )

```

```

for i in range(len(star_list_len)):
    plt.text(i, star_list_len[i],
             '# {0}\n {1:.3f} %'.format(star_list_len[i],
             100*star_list_len[i]/star_list_len[0]),
             fontsize=5
            )

plt.yscale('log')
plt.grid(True, which='both')
plt.title('Filter statistics')
plt.tight_layout()
plt.savefig('filter_history.pdf')
plt.show()
print(
    ... info message ...
)
except:
    print(
    ... warning message ...
)

```

As another informative feature, a plot is being generated, containing the logged statistics about the respective filter step. After all, the program creates a plot, visualizing statistics about how many stars are thrown away after any filter step is applied.

```

allstars_filtered.add_index('hip')
allstars_filtered.show_in_notebook(show_row_index=False)

```

Finally, the routine ends with printing the list of the stars, that meet all conditions. In the end, this list can then be utilized to help with the planning of observations.

12.2 PySPAN - Proceedings of a routine written in MIDAS language

As mentioned in the main body of this thesis, PySPAN is a helper tool to measure equivalent widths and perform the curve of growth analysis for the sodium doublet. The idea has been derived from a tool called SPAN, former in use for the astrophysical lab course at the Institute for physics and astronomy of the University of Potsdam, and programmed by Prof. Dr. Philipp Richter.

In fact, PySPAN is more a product of the conversion of SPAN into Python 3 language. However, a few more features are included. PySPAN as itself is still a work in progress and is not intended to get finished with the end of this thesis. Yet, the program only works for the purpose of reducing data, regarding the absorption of the Na I doublet. It is intended to be modified in a way, making it more universal and applicable for a more general context (e.g. CoG analysis with other series of lines).

For sure, also a variety of optimizations, regarding the computation efficiency, can and should be made in the future. However, we do without a detailed code discussion of the program like we did in the most recent chapter. The code is just too large, in order to be discussed in the scope of this bachelor thesis. Because of this, we want to refer to the respective GitHub page, where the most up-to-date version of this program will be available, along with a more detailed description, and user manual.

13 Comments on Spectra/Observation Log

The following section contains a few comments on each observation subject, including the respective observation session, as well as some general comments on the observation conditions themselves. To maintain the brevity of this chapter, we comment on the spectra themselves with bullet points.

13.1 Archival Data (31.08./01.09.2020)

For two stars (namely α Cyg and γ Cas), spectra were available in the OST archive from previous observations. Both have surface temperatures, high enough, to let their atmospheric Na I absorption vanish, making them suitable for our survey. In addition, both can be found at exceptionally low galactic latitudes, also increasing the likeliness of finding ISM absorption lines in their spectra. During the obtainment process of both stars, the guiding was performed by hand, which should not affect the spectra's quality. The SNR of both exposures is very high because each star has a high apparent brightness.

HIP102098 - α Cyg

RA: 20H 41M 26S

DEC: +45DEG 16M 49S

Observation Modalities

<i>observation begins at:</i>	01:25:36.00 CEST (23:25:36.00 UT)
<i>altitude above horizon:</i>	66.3 deg
<i>resulting air mass:</i>	1.09
<i>total integration time:</i>	300 s \approx 5 min
<i>sub-exposures:</i>	1 \times 300 s

Comments on the resulting echellogram

<i>overall SNR:</i>	very high
<i>Na I feature:</i>	very strong Na I doublet

Comments on the further data reduction

<i>MIDAS:</i>	data reduction went OK without any problems
---------------	---

HIP4427 - γ Cas

RA: 00H 56M 46S

DEC: +60DEG 43M 00S

Observation Modalities

<i>observation begins at:</i>	02:22:05.00 CEST (00:22:05.00 UT)
<i>altitude above horizon:</i>	78.4 deg
<i>resulting air mass:</i>	1.02
<i>total integration time:</i>	300 s \approx 5 min
<i>sub-exposures:</i>	1 \times 300 s

Comments on the resulting echellogram

<i>overall SNR:</i>	very high
<i>Na I feature:</i>	minute Na I absorption visible; many more noticeable absorption lines within the Na I region

The star shows very strong Balmer emission, in conjunction with absorption, forming complex absorption line profiles.

Comments on the further data reduction

<i>MIDAS:</i>	data reduction went OK without any problems
---------------	---

13.2 Archival Data (07./08.11.2020)

HIP2599 - κ Cas

RA: 00H 33M 00s

DEC: +62DEG 55M 54s

Observation Modalities

observation begins at: 23:54:35.00 CET (22:54:35.00 UT)
altitude above horizon: 66.9 deg
resulting air mass: 1.07
total integration time: 900 s \approx 15 min
sub-exposures: 1 \times 900 s

Comments on the resulting echellogram

overall SNR: high
Na I feature: very strong and most certainly saturated Na I absorption

Comments on the further data reduction

MIDAS: The calibration of the echellogram leads to a chaotic spectrum with many discontinuities. Maybe the dark frames are not proper?

13.3 V1405 Cas (14./15.04.2021)

After a longer bad-weather period, the opportunity was taken to observe the recently discovered nova in Cassiopeia (with the star identifier V1405 Cas). This observation was initially not intended to be included in this thesis. However, and coincidentally, the nova is located at exceptionally low galactic latitudes, making it a promising target for potential ISM line of sight absorption.

V1405 Cas

RA: 23H 24M 48s

DEC: +61DEG 11M 15s⁴⁰

Observation Modalities

observation begins at: 21:22:24.57 CEST (19:22:24.57 UT)
altitude above horizon: 24.6 deg
resulting air mass: 2.32
total integration time: 4 800 s = 80 min
sub-exposures: 3 \times 1 600 s

Comments on the resulting echellogram

overall SNR: good (referring to the stack of all sub-exposures)
Na I feature: strong Na I absorption and features are distinctly split up

Comments on the further data reduction

MIDAS: data reduction went OK without any problems; darkframes had to be redone since the resulting data contained negative fluxes

13.4 Initial Observation Trial (21./22.04.2021)

Even though the weather turned bad as of midnight, the observation time was sufficient for taking at least one usable spectrum.

⁴⁰ICRS coordinates were taken from the AAVSO Database

HIP106032 - β Cep

RA: 21^H 28^M 40^S

DEC: +70^{DEG} 33^M 39^S

Observation Modalities

<i>observation begins at:</i>	02:18:00.38 CEST (00:18:00.38 UT)
<i>altitude above horizon:</i>	47.8 deg
<i>resulting air mass:</i>	1.36
<i>total integration time:</i>	577 s \approx 9.5 min
<i>sub-exposures:</i>	1 \times 577 s

Comments on the resulting echellogram

<i>overall SNR:</i>	high
<i>Na I feature:</i>	no Na I absorption visible

Comments on the further data reduction

<i>MIDAS:</i>	data reduction went OK without any problems
---------------	---

13.5 First Major Observation Night (25./26.04.2021)

The first actual massive observation session takes place on the night of the 25./26.04.2021. The weather is just optimal for stellar spectroscopy. There are no clouds at all, potentially blocking starlight. Since it is planned to observe a set of at least 10 stars during this night with integration times consequently exceeding a quarter an hour, we want to try computer-assisted with the SBIG St-i guiding camera. We do this by centering the star of interest directly on the slit, and use the remaining light as the “guide star”. It is assumed, that Maxim DL takes the spatially (on the camera chip) weighted average intensity maximum, which would be directly on the slit, where the star of interest should be positioned ideally.

This process is only intended to be a temporary workaround method since the dedicated software “Spec Track” did not work properly at this moment.

In the end, this method led to improvable results. A lot of light flux of the sources has been cut out as we could conclude afterward. Even though we also did spectroscopy on bright stars with reasonable integration times, the final SNR was not as high as expected, compared to a few stars at the beginning, where guiding by hand was utilized.

This can be also due to an improvable starting position of the star on the slit. If it does not sit centered, the guiding will, of course, try to move the star slightly off the slit, and, therefore, consequently cutting off the flux.

There have been 11 Stars observed during this night. The following list is sorted chronologically⁴¹ in ascending order:

HIP2474 - 13 Cas

RA: 00^H 31^M 25^S

DEC: +66^{DEG} 31^M 11^S

Observation Modalities

<i>observation begins at:</i>	22:57:47.91 CEST (20:57:47.91 UT)
<i>altitude above horizon:</i>	29.1 deg
<i>resulting air mass:</i>	2.04
<i>total integration time:</i>	500 s \approx 8 min
<i>sub-exposures:</i>	1 \times 500 s

Comments on the resulting echellogram

<i>overall SNR:</i>	OK
<i>Na I feature:</i>	clearly visible

Comments on the further data reduction

<i>MIDAS:</i>	data reduction went OK without any problems
---------------	---

⁴¹The respective time stamps refer to the value given in the fits header of each exposure.

HIP15520

RA: 03H 19M 59S

DEC: +65DEG 39M 08S

Observation Modalities

observation begins at: 23:33:58.64 CEST (21:33:58.64 UT)
altitude above horizon: 31.3 deg
resulting air mass: 1.88
total integration time: 1 000 s \approx 16.5 min
sub-exposures: 1 \times 1 000 s

Comments on the resulting echellogram

overall SNR: OK
Na I feature: very light doublet visible
There might be some H α emission \implies emission peak in the red

Comments on the further data reduction

MIDAS: data reduction went OK without any problems

HIP101383

RA: 20H 32M 46S

DEC: +43DEG 12M 14S

Observation Modalities

observation begins at: 00:17:38.59 CEST (22:17:38.59 UT)
altitude above horizon: 21.5 deg
resulting air mass: 2.40
total integration time: 1 000 s \approx 16.5 min
sub-exposures: 1 \times 1 000 s

Comments on the resulting echellogram

overall SNR: extremely low
Na I feature: however: Na I absorption visible
The low signal can be due to bad guiding and the high air mass.

Comments on the further data reduction

MIDAS: data reduction went OK without any problems

HIP102827

RA: 20H 49M 55S

DEC: +46DEG 39M 41S

Observation Modalities

observation begins at: 01:06:37.71 CEST (23:06:37.71 UT)
altitude above horizon: 32.9 deg
resulting air mass: 1.94
total integration time: 1 000 s \approx 16.5 min
sub-exposures: 1 \times 1 000 s

Comments on the resulting echellogram

overall SNR: very low
Na I feature: hard to find any absorption features
The low signal is most likely due to bad guiding: After the exposure has been taken the stars was not centered on the slit anymore.

Comments on the further data reduction

MIDAS: data reduction went OK without any problems

HIP103371

RA: 20H 56M 35s

DEC: +44DEG 55M 29s

Observation Modalities

observation begins at: 02:12:13.31 CEST (00:12:13.31 UT)
altitude above horizon: 39.5 deg
resulting air mass: 1.65
total integration time: 1 000 s \approx 16.5 min (+ additional 300 s)
sub-exposures: 1 \times 1 000 s; 1 \times 300 s

Comments on the resulting echellogram

overall SNR: high
Na I feature: very strong Na I doublet

Comments on the further data reduction

MIDAS: data reduction went OK without any problems

HIP100518

RA: 20H 22M 58s

DEC: +39DEG 12M 40s

Observation Modalities

observation begins at: 02:37:46.65 CEST (00:37:46.65 UT)
altitude above horizon: 44.5 deg
resulting air mass: 1.49
total integration time: 1 000 s \approx 16.5 min
sub-exposures: 1 \times 1 000 s

Comments on the resulting echellogram

overall SNR: rather low
Na I feature: distinct Na I doublet

During the exposure the tracking might have been off for a certain time. The slit seems to be illuminated not evenly on its vertical cross section.

Comments on the further data reduction

MIDAS: data reduction went OK without any problems

HIP103089 - 57 Cyg

RA: 20H 53M 15s

DEC: +44DEG 23M 14s

Observation Modalities

observation begins at: 03:09:25.23 CEST (01:09:25.23 UT)
altitude above horizon: 47.7 deg
resulting air mass: 1.41
total integration time: 1 000 s \approx 16.5 min
sub-exposures: 1 \times 1 000 s

Comments on the resulting echellogram

overall SNR: intermediate
Na I feature: broad Na I doublet
 \Rightarrow may originate from a companion star?

A query on SIMBAD shows HIP 103089 to be an eclipsing multiple star system. There the sodium doublet may be a superposition of stellar- as well as ISM absorption. The star lies in direct line of sight of to great nebulosity complex in Cygnus. In vicinity many H II regions, as well as dark nebulae can be found.

Comments on the further data reduction

MIDAS: data reduction went OK without any problems

HIP107136 - π^1 Cyg

RA: 21H 42M 06S

DEC: +51DEG 11M 23S

Observation Modalities

observation begins at: 03:35:48.19 CEST (01:35:48.19 UT)
altitude above horizon: 48.3
resulting air mass: 1.39
total integration time: 1 000 s \approx 16.5 min
sub-exposures: 1 \times 1 000 s

Comments on the resulting echellogram

overall SNR: very high
Na I feature: exceptionally narrow Na I doublet \implies likely for ISM absorption.
Absorption lines seem slightly bend towards the order boundaries. Any structure on the star?

Comments on the further data reduction

MIDAS: data reduction went OK without any problems

HIP104962

RA: 21H 15M 37S

DEC: +47DEG 58M 26S

Observation Modalities

observation begins at: 03:56:21.41 CEST (01:56:21.41 UT)
altitude above horizon: 53.3
resulting air mass: 1.29
total integration time: 1 000 s \approx 16.5 min
sub-exposures: 1 \times 1 000 s

Comments on the resulting echellogram

overall SNR: very high
Na I feature: narrow Na I doublet \implies likely for ISM absorption

Comments on the further data reduction

MIDAS: data reduction went OK without any problems

HIP100574

RA: 20H 23M 44S

DEC: +37DEG 28M 35S

Observation Modalities

observation begins at: 04:16:42.47 CEST (02:16:42.47 UT)
altitude above horizon: 58.3
resulting air mass: 1.21
total integration time: 1 000 s \approx 16.5 min
sub-exposures: 1 \times 1 000 s

Comments on the resulting echellogram

overall SNR: very high
Na I feature: little Na I absorption

Comments on the further data reduction

MIDAS: data reduction went OK without any problems

HIP100142

RA: 20H 18M 50s

DEC: +46DEG 19M 20s

Observation Modalities

observation begins at: 04:36:59.57 CEST (02:36:59.57 UT)
altitude above horizon: 67.2
resulting air mass: 1.11
total integration time: 1 000 s \approx 16.5 min
sub-exposures: 1 \times 1 000 s

Comments on the resulting echellogram

overall SNR: rather low
Na I feature: strong Na I absorption
The SNR is rather low here. This is due to the higher sky brightness, since this spectrum has been taken during dawn.

Comments on the further data reduction

MIDAS: data reduction went OK without any problems

13.6 Second Major Observation Night (26./27.04.2021)

Because of good weather, the second observation night directly proceeds the first one. Just like the night before, the weather turned out to be reasonably fine for another stellar spectroscopy session.

In the beginning of the observations, an issue occurred: The telescope mount did not start properly. This can be due to an incorrect shutdown of the mount from the night before.

In the end, the solution was to turn the observatory's emergency-stop lever that interrupts the power feed to the mount, and the whole observatory management system, causing a shutdown. After the power transfer has been enabled again, all systems started up successfully.

This night, there have been taken additional 11 spectra, from which only 10 could be used due to a misfortune during the save process of the spectrum. Accidentally, instead of the actual star spectrum, the last auto guider image has been saved. Of course, such an image is not usable for us, making the data taken for the star HIP 103732 obsolete, unfortunately.

HIP103530

RA: 20H 58M 30s

DEC: +50DEG 27M 42s

Observation Modalities

observation begins at: 23:50:12.94 CEST (21:50:12.94 UT)
altitude above horizon: 26.6
resulting air mass: 2.35
total integration time: 1 000 s \approx 16.5 min (+1 000 s unusable)
sub-exposures: 2 \times 1 000 s

Comments on the resulting echellogram

overall SNR: very high
Na I feature: no Na I absorption
The spectrum exhibits only a very little amount of absorption features. There have been taken two exposures of this object. The first one was unluckily not usable, as BACHES orientation changed without remark between last, and this observation night. This issue was not identified until the first spectrum has been taken.

Comments on the further data reduction

MIDAS: data reduction went OK without any problems

HIP100044 - P Cyg

RA: 20H 17M 47s

DEC: +38DEG 01M 59s

Observation Modalities

observation begins at: 00:18:11.41 CEST (22:18:11.41 UT)
altitude above horizon: 25.1
resulting air mass: 2.55
total integration time: 1 000 s \approx 16.5 min
sub-exposures: 1 \times 1 000 s

Comments on the resulting echellogram

overall SNR: very strong
Na I feature: a very narrow, but also very deep absorption observed
Many P Cygni absorption/emission profiles scattered across the whole spectrum. Interesting question: Does the Doppler shift of the Na I doublet match with the ones of the other absorption lines? If not, this could be also ISM absorption.

Comments on the further data reduction

MIDAS: data reduction went OK without any problems

HIP103732

RA: 21H 01M 11s

DEC: +46DEG 09M 21s

Observation Modalities

observation begins at: 01:10:17 CEST (23:10:17 UT)
altitude above horizon: 30.1
resulting air mass: 1.99
total integration time: 1 000 s \approx 16.5 min
sub-exposures: 1 \times 1 000 s

Comments on the resulting echellogram

overall SNR: - - -
Na I feature: - - -
Unfortunately, no spectrum has been saved. Instead, the last image of the guiding camera has been saved, providing us no usable spectrum.

Comments on the further data reduction

MIDAS: - - -

HIP103871

RA: 21H 02M 49s

DEC: +45DEG 50M 56s

Observation Modalities

observation begins at: 01:15:47.38 CEST (23:15:47.38 UT)
altitude above horizon: 32.4
resulting air mass: 1.97
total integration time: 1 000 s \approx 16.5 min
sub-exposures: 1 \times 1 000 s

Comments on the resulting echellogram

overall SNR: intermediate
Na I feature: no Na I absorption visible

Comments on the further data reduction

MIDAS: data reduction went OK without any problems

HIP99431

RA: 20H 10M 54S

DEC: +30DEG 47M 23S

Observation Modalities

observation begins at: 01:42:26.12 CEST (23:42:26.12 UT)
altitude above horizon: 32.8
resulting air mass: 1.97
total integration time: 1 000 s \approx 16.5 min
sub-exposures: 1 \times 1 000 s

Comments on the resulting echellogram

overall SNR: rather low
Na I feature: no Na I absorption visible
Among of some absorption features, also emission lines somehow became visible. This can also be due to artificial lighting?

Comments on the further data reduction

MIDAS: data reduction went OK without any problems

HIP101138 - ω^1 Cyg

RA: 20H 30M 04S

DEC: +48DEG 57M 06S

Observation Modalities

observation begins at: 02:08:51.88 CEST (00:08:51.88 UT)
altitude above horizon: 45.6
resulting air mass: 1.45
total integration time: 1 000 s \approx 16.5 min
sub-exposures: 1 \times 1 000 s

Comments on the resulting echellogram

overall SNR: very high
Na I feature: distinct and narrow Na I absorption

Comments on the further data reduction

MIDAS: data reduction went OK without any problems

HIP102155

RA: 20H 41M 57s

DEC: +41DEG 43M 01s

Observation Modalities

observation begins at: 02:38:56.84 CEST (00:38:56.84 UT)
altitude above horizon: 44.0
resulting air mass: 1.51
total integration time: 1 000 s \approx 16.5 min
sub-exposures: 1 \times 1 000 s

Comments on the resulting echellogram

overall SNR: high
Na I feature: strong and narrow Na I absorption
The spectrum exhibits a lot of absorption in the blue, and a strong one in the red \implies could be H α ?

Comments on the further data reduction

MIDAS: data reduction went OK without any problems

HIP105891

RA: 21H 26M 45s

DEC: +52DEG 53M 55s

Observation Modalities

observation begins at: 03:05:11.74 CEST (01:05:11.74 UT)
altitude above horizon: 47.7
resulting air mass: 1.40
total integration time: 1 000 s \approx 16.5 min
sub-exposures: 1 \times 1 000 s

Comments on the resulting echellogram

overall SNR: high
Na I feature: no Na I absorption visible

Comments on the further data reduction

MIDAS: data reduction went OK without any problems

HIP93805 - λ Aql

RA: 19H 06M 15s

DEC: -04DEG 52M 57s

Observation Modalities

observation begins at: 03:46:12.20 CEST (01:46:12.20 UT)
altitude above horizon: 28.1
resulting air mass: 2.22
total integration time: 1 000 s \approx 16.5 min
sub-exposures: 1 \times 1 000 s

Comments on the resulting echellogram

overall SNR: very high
Na I feature: no absorption visible
This star is a high proper motion stars, according to the SIMBAD database.

Comments on the further data reduction

MIDAS: data reduction went OK without any problems

HIP89641

RA: 18H 17M 47S

DEC: -15DEG 25M 51S

Observation Modalities

observation begins at: 04:14:14.49 CEST (02:14:14.49 UT)
altitude above horizon: 21.8
resulting air mass: 2.7
total integration time: 1 000 s \approx 16.5 min
sub-exposures: 1 \times 1 000 s

Comments on the resulting echellogram

overall SNR: intermediate
Na I feature: exceptional strong Na I absorption

The spectrum of this stars could not be processed. This is due to a rotated wavelength calibration image (ThAr exposure). Most likely, the camera cables were too short, and, therefore, were pulling on one camera side. This rotates the camera's field of view and makes a wavelength calibration for this spectrum impossible, unfortunately.

Comments on the further data reduction

MIDAS: data reduction went OK without any problems

HIP90096

RA: 18H 23M 12S

DEC: -12DEG 00M 53S

Observation Modalities

observation begins at: 04:50:52.64 CEST (02:50:52.64 UT)
altitude above horizon: 25.5
resulting air mass: 2.3
total integration time: 577 s \approx 9.5 min
sub-exposures: 1 \times 577 s

Comments on the resulting echellogram

overall SNR: very low
Na I feature: exhibits Na I absorption, next to Na I emission lines

The reason for an exposure of 577 seconds comes from the fact, that at observation time, daybreak (the high sky brightness) already affected the resulting spectrum. As the sky gets brighter, it contributes more and more flux, leading to sunlight-polluted data. Again, the camera probably rotated during the last mount's slew process. \implies The camera's power cable is not long enough in this specific mounts orientation. \longrightarrow low declination and on the right ascension axis close to the meridian flip.

Comments on the further data reduction

MIDAS: data reduction can not be done; the camera's field of view is severely rotated

13.7 Third Major Observation Night (27./28.04.2021)

During this observation night (the third one in a row), no major issues occurred. Compared to the preceding two nights, the automatized guiding was the best. This led to highly illuminated echellograms, resulting in spectra with a high SNR. Unlike the other two nights, the objects

observed here were chosen “by hand”. This includes some interesting targets close to some H II regions, or areas that we expect to be densely filled with ISM.

HIP17358

RA: 03H 42M 56S

DEC: +47DEG 47M 15S

Observation Modalities

observation begins at: 21:45:52.12 CEST (19:45:52.12 UT)
altitude above horizon: 25.1
resulting air mass: 2.20
total integration time: 1 000 s \approx 16.5 min
sub-exposures: 1 \times 1 000 s

Comments on the resulting echellogram

overall SNR: very high
Na I feature: almost no absorption visible at all
sample text

Comments on the further data reduction

MIDAS: data reduction went OK without any problems;
darkframes had to be redone, since the resulting
data contained negative fluxes

HIP109556 - λ Cep

RA: 22H 11M 31S

DEC: +59DEG 24M 52S

Observation Modalities

observation begins at: 22:11:20.91 CEST (20:11:20.91 UT)
altitude above horizon: 23.5
resulting air mass: 2.54
total integration time: 1 000 s \approx 16.5 min
sub-exposures: 1 \times 1 000 s

Comments on the resulting echellogram

overall SNR: very high
Na I feature: strong Na I absorption, complexity in the absorption profile

Comments on the further data reduction

MIDAS: data reduction went OK without any problems;
darkframes had to be redone, since the resulting
data contained negative fluxes

HIP106285

RA: 21H 31M 38S

DEC: +57DEG 30M 09S

Observation Modalities

observation begins at: 22:34:41.57 CEST (20:34:41.57 UT)
altitude above horizon: 24.5
resulting air mass: 2.48
total integration time: 1 000 s \approx 16.5 min
sub-exposures: 1 \times 1 000 s

Comments on the resulting echellogram

overall SNR: rather low
Na I feature: strong Na I absorption

Comments on the further data reduction

MIDAS: data reduction went OK without any problems;
darkframes had to be redone, since the resulting
data contained negative fluxes

HIP107164

RA: 21H 42M 24S

DEC: +57DEG 44M 10S

Observation Modalities

observation begins at: 22:58:36.38 CEST (20:58:36.38 UT)
altitude above horizon: 25.5
resulting air mass: 2.39
total integration time: 1 000 s \approx 16.5 min
sub-exposures: 1 \times 1 000 s

Comments on the resulting echellogram

overall SNR: intermediate
Na I feature: strong Na I absorption
also strong emission in the red \implies maybe H α ?

Comments on the further data reduction

MIDAS: data reduction went OK without any problems;
darkframes had to be redone, since the resulting
data contained negative fluxes

HIP106843

RA: 21H 38M 26s

DEC: +56DEG 58M 25s

Observation Modalities

observation begins at: 22:28:55.48 CEST (21:28:55.48 UT)
altitude above horizon: 28.3
resulting air mass: 2.27
total integration time: 1 000 s \approx 16.5 min
sub-exposures: 1 \times 1 000 s

Comments on the resulting echellogram

overall SNR: intermediate
Na I feature: strong Na I absorption visible
also comparable strong He I absorption close to the Na I doublet

Comments on the further data reduction

MIDAS: data reduction went OK without any problems;
darkframes had to be redone, since the resulting
data contained negative fluxes

HIP115198

RA: 23H 20M 01s

DEC: +61DEG 08M 59s

Observation Modalities

observation begins at: 00:19:18.69 CEST (22:19:18.69 UT)
altitude above horizon: 28.5
resulting air mass: 2.20
total integration time: 2 000 s \approx 33.5 min
sub-exposures: 1 \times 2 000 s

Comments on the resulting echellogram

overall SNR: intermediate
Na I feature: distinct Na I absorption

Comments on the further data reduction

MIDAS: data reduction went OK without any problems;
darkframes had to be redone, since the resulting
data contained negative fluxes

HIP531

RA: 00H 06M 26s

DEC: +64DEG 11M 46s

Observation Modalities

observation begins at: 00:58:34.15 CEST (22:58:34.15 UT)
altitude above horizon: 30
resulting air mass: 2.03
total integration time: 1 000 s \approx 16.5 min
sub-exposures: 1 \times 1 000 s

Comments on the resulting echellogram

overall SNR: high
Na I feature: distinct, but marrow Na I absorption

some light emission in the red \implies maybe from artificial lighting, looks a little unnatural?

Comments on the further data reduction

MIDAS: data reduction went OK without any problems;
darkframes had to be redone, since the resulting
data contained negative fluxes

HIP103312

RA: 20H 55M 50s

DEC: +47DEG 25M 04s

Observation Modalities

observation begins at: 01:20:03.46 CEST (23:20:03.46 UT)
altitude above horizon: 35.4
resulting air mass: 1.82
total integration time: 1 000 s \approx 16.5 min
sub-exposures: 1 \times 1 000 s

Comments on the resulting echellogram

overall SNR: high
Na I feature: very strong Na I absorption; also relative broad

This star lies within a nebulosity.

Comments on the further data reduction

MIDAS: data reduction went OK without any problems;
darkframes had to be redone, since the resulting
data contained negative fluxes

HIP106186

RA: 21H 30M 26s

DEC: +58DEG 18M 58s

Observation Modalities

observation begins at: 00:43:26.40 CEST (23:43:26.40 UT)
altitude above horizon: 33.1
resulting air mass: 1.94
total integration time: 1 000 s \approx 16.5 min
sub-exposures: 1 \times 1 000 s

Comments on the resulting echellogram

overall SNR: high
Na I feature: strong Na I absorption

Comments on the further data reduction

MIDAS: data reduction went OK without any problems;
darkframes had to be redone, since the resulting
data contained negative fluxes

HIP112470

RA: 22H 46M 54s

DEC: +58DEG 05M 04s

Observation Modalities

observation begins at: 02:11:21.19 CEST (00:11:21.19UT)
altitude above horizon: 37.5
resulting air mass: 1.77
total integration time: 1 000 s \approx 33.5 min
sub-exposures: 1 \times 2 000 s

Comments on the resulting echellogram

overall SNR: very low
Na I feature: interesting Na I absorption profile; absorption
lines are split up

even though the sensor was exposed 2000 s, the spectrum is pretty noisy \implies bad tracking quality?

Comments on the further data reduction

MIDAS: data reduction went OK without any problems;
darkframes had to be redone, since the resulting
data contained negative fluxes

HIP95700

RA: 17^H 27^M 54^S

DEC: +20^{DEG} 14^M 51^S

Observation Modalities

observation begins at: 02:54:12.33 CEST (00:54:12.33 UT)
altitude above horizon: 42.6
resulting air mass: 1.54
total integration time: 1 000 s \approx 16.5 min
sub-exposures: 1 \times 1 000 s

Comments on the resulting echellogram

overall SNR: rather low
Na I feature: distinct Na I absorption

According to SIMBAD this is an emission line star.

Comments on the further data reduction

MIDAS: data reduction went OK without any problems;
darkframes had to be redone, since the resulting
data contained negative fluxes

HIP95818

RA: 19^H 29^M 21^S

DEC: +20^{DEG} 16^M 47^S

Observation Modalities

observation begins at: 03:16:28.51 CEST (01:16:28.51 UT)
altitude above horizon: 45.5
resulting air mass: 1.46
total integration time: 1 000 s \approx 16.5 min
sub-exposures: 1 \times 1 000 s

Comments on the resulting echellogram

overall SNR: rather low
Na I feature: no absorption visible

Comments on the further data reduction

MIDAS: data reduction went OK without any problems;
darkframes had to be redone, since the resulting
data contained negative fluxes

HIP102589

RA: 20^H 47^M 25^S

DEC: +36^{DEG} 29^M 27^S

Observation Modalities

observation begins at: 03:38:23.27 CEST (01:38:23.27 UT)
altitude above horizon: 49.4
resulting air mass: 1.37
total integration time: 1 000 s \approx 16.5 min
sub-exposures: 1 \times 1 000 s

Comments on the resulting echellogram

overall SNR: high
Na I feature: light Na I absorption with very narrow features

Comments on the further data reduction

MIDAS: data reduction went OK without any problems;
darkframes had to be redone, since the resulting
data contained negative fluxes

V1405 Cas

RA: 23H 24M 48S

DEC: +61DEG 11M 15S⁴²

Observation Modalities

<i>observation begins at:</i>	04:06:38.29 CEST (02:06:38.29 UT)
<i>altitude above horizon:</i>	46.4
<i>resulting air mass:</i>	1.44
<i>total integration time:</i>	1 500 s = 25 min
<i>sub-exposures:</i>	1 × 1 500 s

Comments on the resulting echellogram

<i>overall SNR:</i>	intermediate
<i>Na I feature:</i>	strong Na I absorption and features are distinctly split up

Comments on the further data reduction

<i>MIDAS:</i>	data reduction went OK without any problems; darkframes had to be redone, since the resulting data contained negative fluxes
---------------	--

13.8 Fourth Observation Night (07./08.05.2021)

The observation, this time, started late in the night because the observatory was occupied for other purposes earlier in the evening. Therefore, only two stars were observed this night, before fog disabled further observations. We focused on targets at *high* galactic latitudes to also have spectra, with potentially *no* ISM absorption in them. This might yield us a neat reference to the other stars, expected to show such ISM absorption.

HIP67301 - η UMa - Alkaid

RA: 13H 47M 32S

DEC: +49DEG 18M 48S

Observation Modalities

<i>observation begins at:</i>	00:56:16.20 CEST (22:56:16.20 UT)
<i>altitude above horizon:</i>	77.9 deg
<i>resulting air mass:</i>	1.02
<i>total integration time:</i>	600 s \approx 10 min
<i>sub-exposures:</i>	1 × 600 s

Comments on the resulting echellogram

<i>overall SNR:</i>	very high
<i>Na I feature:</i>	no Na I absorption visible

Comments on the further data reduction

<i>MIDAS:</i>	data reduction went OK without any problems
---------------	---

⁴²ICRS coordinates were taken from the AAVSO Database

HIP63125 - α^2 CVn - Cor Caroli

RA: 12H 56M 02S

DEC: +38DEG 19M 06S

Observation Modalities

observation begins at: 03:06:31.56 CEST (01:06:31.56 UT)
altitude above horizon: 43.5 deg
resulting air mass: 1.39
total integration time: 1 000 s \approx 16.5 min
sub-exposures: 1 \times 1 000 s

Comments on the resulting echellogram

overall SNR: very high
Na I feature: no Na I absorption visible

Comments on the further data reduction

MIDAS: data reduction went OK without any problems

13.9 V1405 Cas (10./11.05.2021)

Because of its peculiarity and its interesting dynamics, we decided to monitor the nova over many weeks, taking spectra, whenever the weather permitted. This observation night was completely focusing on this very object. In the end, we accumulated over 1.5 hours of integration time for the resulting spectrum. By coincidence, it turned out that V1405 Cas reached its brightness maximum just about that time.

V1405 Cas

RA: 23H 24M 48S

DEC: +61DEG 11M 15s⁴³

Observation Modalities

observation begins at: 23:55:34.91 CEST (21:55:34.91 UT)
altitude above horizon: 29.9 deg
resulting air mass: 2.12
total integration time: 6 000 s = 100 min
sub-exposures: 3 \times 2 000 s

Comments on the resulting echellogram

overall SNR: very good (referring to the stack of all sub-exposures)
Na I feature: strong Na I absorption and features are distinctly split up

Comments on the further data reduction

MIDAS: data reduction went OK without any problems;
darkframes had to be redone, since the resulting data contained negative fluxes

13.10 V1405 Cas (02./03.06.2021)

After the most recent observation of V1405 Cas, another observation on this interesting target was done. The nova's brightness was already declining at this point, also requiring us to expose the detector long enough to achieve a reasonable SNR in our spectra. Therefore, a series of 5 images, each exposed for 20 minutes, was taken.

⁴³ICRS coordinates were taken from the AAVSO Database

V1405 Cas

RA: 23H 24M 48S

DEC: +61DEG 11M 15S⁴⁴

Observation Modalities

<i>observation begins at:</i>	04:06:38.29 CEST (02:06:38.29 UT)
<i>altitude above horizon:</i>	43.6 deg
<i>resulting air mass:</i>	1.50
<i>total integration time:</i>	6 000 s = 100 min
<i>sub-exposures:</i>	5 × 1 200 s

Comments on the resulting echellogram

<i>overall SNR:</i>	high (referring to the stack of all sub-exposures)
<i>Na I feature:</i>	strong Na I absorption and features are distinctly split up

Comments on the further data reduction

<i>MIDAS:</i>	data reduction went OK without any problems; darkframes had to be redone since the resulting data contained negative fluxes
---------------	---

14 V1405 Cas Finder Chart

Many times we referred to the variable star system V1405 Cas in the main body of this document. Considering this stars system was of particular interest for us, we actively observed it for many nights, and more are most certainly to come. We attach a co-called *finder chart*, guiding an observer for follow-up investigations to the star of interest, and to avoid confusion with other stars in the vicinity. This is especially helpful for non-computerized observations, for instance.

⁴⁴ICRS coordinates were taken from the AAVSO Database

V1405 Cas
 $\lambda[5875 - 5915] \text{ \AA}$
(D1 centered)

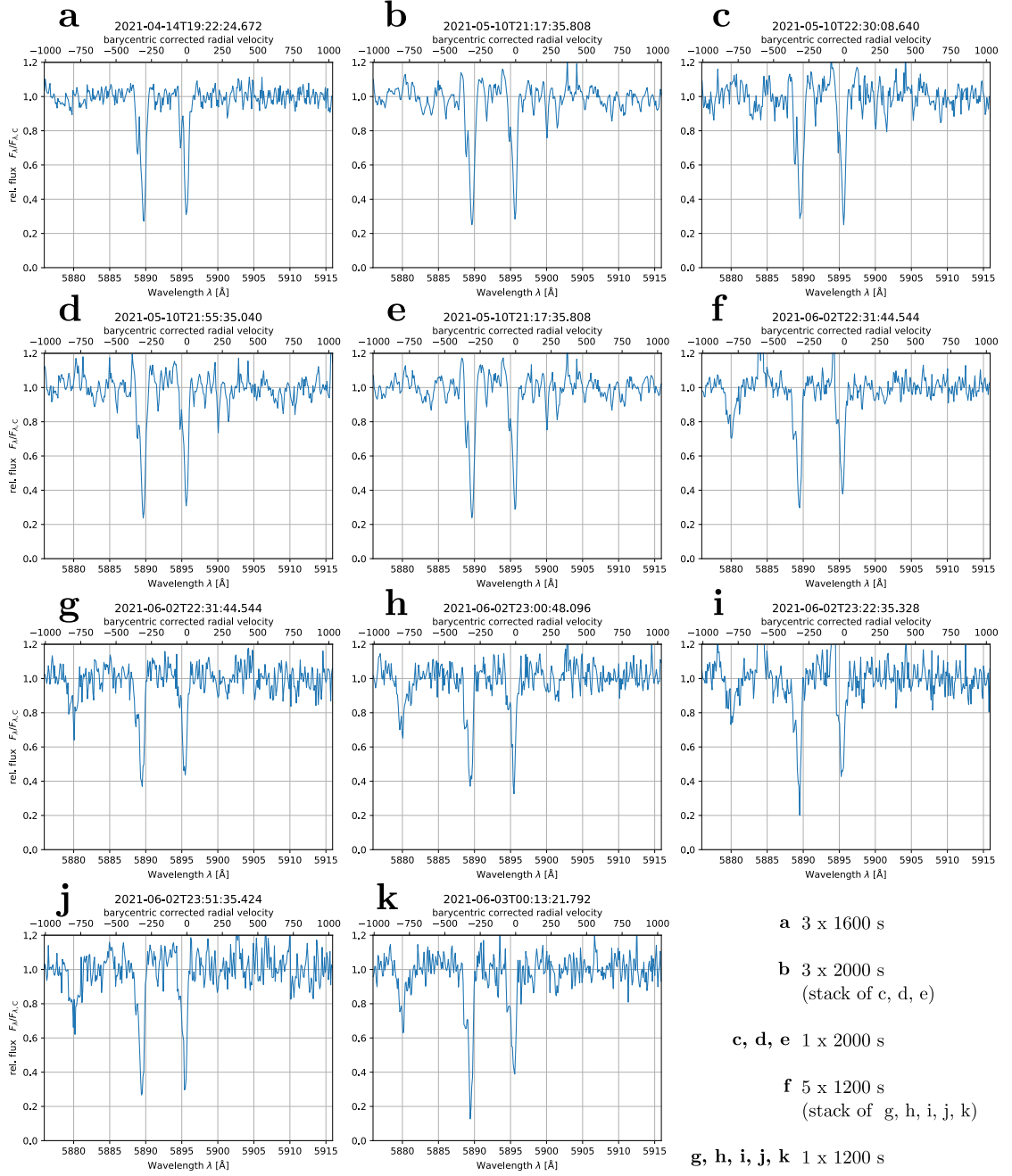


Figure 15.1: A grid of absorption spectra from V1405 Cas, presenting the proximity of the Na I doublet. All spectra in this figure are normalized to their local continuum flux and centered to the rest wavelength of the FRAUNHOFER D1 line. On the top velocity axis, the barycentric velocity correction has been applied.

V1405 Cas
 $\lambda[5869 - 5909] \text{ \AA}$
(D2 centered)

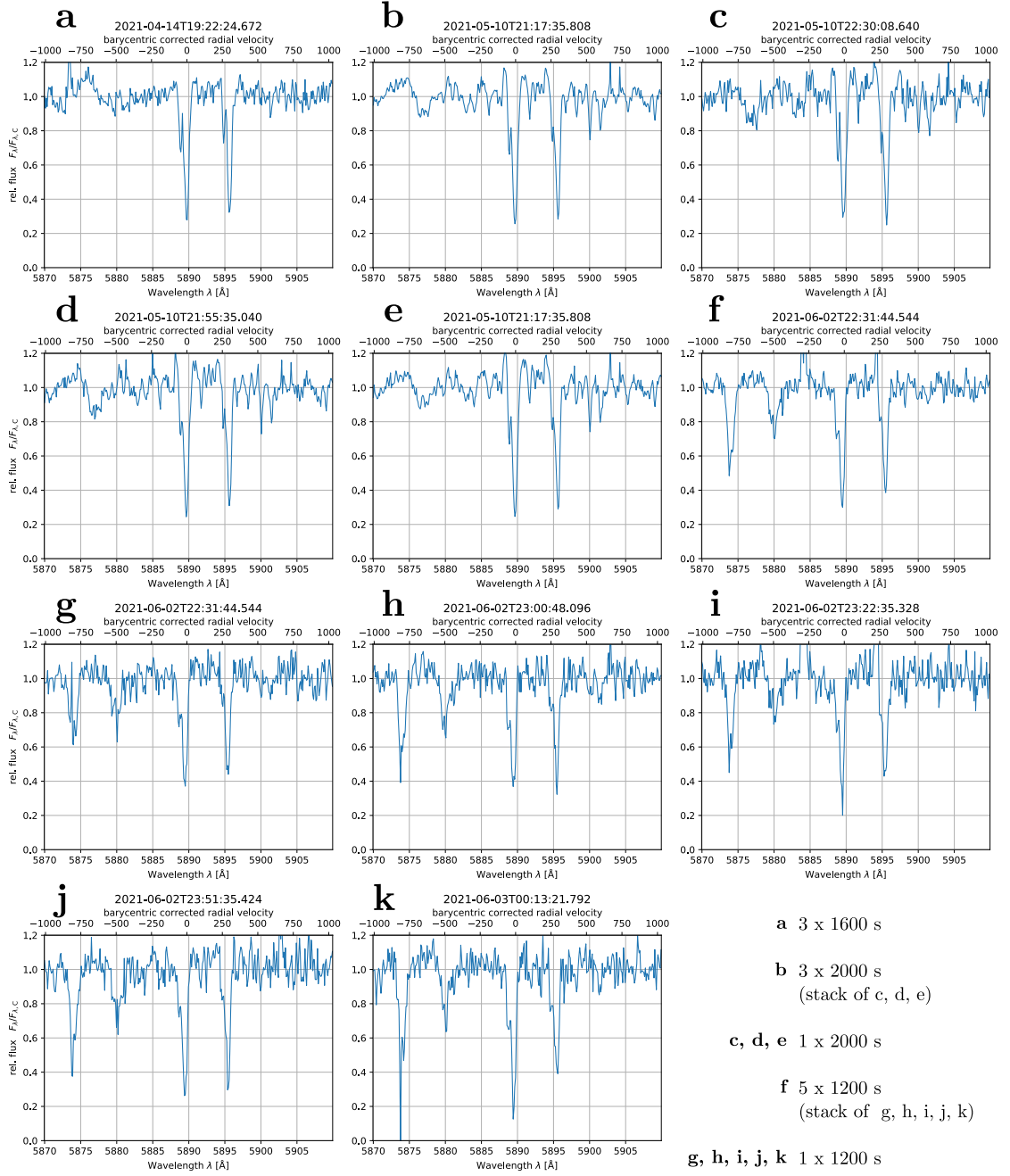


Figure 15.2: A grid of absorption spectra from V1405 Cas, presenting the proximity of the Na I doublet. All spectra in this figure are normalized to their local continuum flux and centered to the rest wavelength of the FRAUNHOFER D2 line. On the top velocity axis, the barycentric velocity correction has been applied.

References

- [1] Summary of the hipparcos and tycho catalogues.
- [2] H. A. Abt and O. Cardona. Confirmation among visual multiples of an increase of AP stars with age. *Astrophysical Journal*, 272:182–189, September 1983.
- [3] Helmut A. Abt and Nidia I. Morrell. The Relation between Rotational Velocities and Spectral Peculiarities among A-Type Stars. *Astrophysical Journal, Supplement*, 99:135, July 1995.
- [4] Jennifer K. Adelman-McCarthy and et. al. Agüeros. The Fourth Data Release of the Sloan Digital Sky Survey. *Astrophysical Journal, Supplement*, 162(1):38–48, January 2006.
- [5] R. Arlt. 100 years ago in Potsdam: Johannes Hartmann discovers interstellar gas. web page, March 2004.
- [6] N. Ben Bekhti, L. Flöer, R. Keller, J. Kerp, D. Lenz, B. Winkel, J. Bailin, M. R. Calabretta, L. Dedes, H. A. Ford, B. K. Gibson, U. Haud, S. Janowiecki, P. M. W. Kalberla, F. J. Lockman, N. M. McClure-Griffiths, T. Murphy, H. Nakanishi, D. J. Pisano, and L. Staveley-Smith. HI4pi: a full-sky hi survey based on EBHIS and GASS. *Astronomy & Astrophysics*, 594:A116, October 2016.
- [7] E. S. Brodskaya. The spectra and magnitudes of 400 stars of spectral class 0-B5 in Milky Way area centered at $\alpha = 23^h 27^m$, $\delta = +61^\circ$. *Izvestiya Ordena Trudovogo Krasnogo Znameni Krymskoj Astrofizicheskoj Observatorii*, 10:104–120, January 1953.
- [8] A. J. Cannon and E. C. Pickering. VizieR Online Data Catalog: Henry Draper Catalogue and Extension (Cannon+ 1918-1924; ADC 1989). *VizieR Online Data Catalog*, page III/135A, October 1993.
- [9] Central Bureau for Astronomical Telegrams. Cbat "transient object followup reports" - pnv j23244760+6111140, March 2021.
- [10] A. Cucchiario, M. Jaschek, C. Jaschek, and D. Macau-Hercot. Spectral classification from the ultraviolet line features of S2/68 spectra. I. Early B-type stars. *Astronomy and Astrophysics, Supplement*, 26:241, November 1976.
- [11] Klaas S. de Boer. *Physics and the interstellar medium*. Argelander-Institut für Astronomie, Universität Bonn, 2007.
- [12] J. R. Ducati. VizieR Online Data Catalog: Catalogue of Stellar Photometry in Johnson's 11-color system. *VizieR Online Data Catalog*, January 2002.
- [13] Gaia Collaboration et. al. Gaia Data Release 1. Summary of the astrometric, photometric, and survey properties. *Astronomy and Astrophysics*, 595:A2, November 2016.
- [14] Gaia Collaboration et. al. The Gaia mission. *Astronomy and Astrophysics*, 595:A1, November 2016.
- [15] R. F. Garrison and J. Kormendy. Some characteristics of the young open cluster Trumpler 37. *Publications of the ASP*, 88:865–869, December 1976.
- [16] R. O. Gray, Q. S. Riggs, C. Koen, S. J. Murphy, I. M. Newsome, C. J. Corbally, K. P. Cheng, and J. E. Neff. The Discovery of λ Bootis Stars: The Southern Survey I. *Astronomical Journal*, 154(1):31, July 2017.
- [17] J. Hartmann. Investigations on the spectrum and orbit of delta orionis. *The Astrophysical Journal*, 19:268–286, may 1904.
- [18] E. Høg, C. Fabricius, V. V. Makarov, S. Urban, T. Corbin, G. Wycoff, U. Bastian, P. Schwekendiek, and A. Wicenec. The Tycho-2 catalogue of the 2.5 million brightest stars. *Astronomy and Astrophysics*, 355:L27–L30, March 2000.

- [19] Douglas P. Hube. The radial velocities of 335 late B-type stars. *Memoirs of the RAS*, 72:233, January 1970.
- [20] H. L. Johnson and W. W. Morgan. Fundamental stellar photometry for standards of spectral type on the revised system of the yerkes spectral atlas. *The Astrophysical Journal*, 117:313, may 1953.
- [21] Kalberla, P. M. W. and Haud, U. Gass: The parkes galactic all-sky survey - update: improved correction for instrumental effects and new data release. *A&A*, 578:A78, 2015.
- [22] Hannu Karttunen, Pekka KrÄ¶ger, Heikki Oja, Markku Poutanen, and Karl Johan Donner. *Fundamental Astronomy* -. Springer, Berlin, Heidelberg, 2016.
- [23] A. Kramida, Yu. Ralchenko, J. Reader, and and NIST ASD Team. NIST Atomic Spectra Database (ver. 5.8), [Online]. Available: <https://physics.nist.gov/asd> [2021, August 23]. National Institute of Standards and Technology, Gaithersburg, MD., 2020.
- [24] Sneh Lata, A. K. Pandey, Neelam Panwar, W. P. Chen, M. R. Samal, and J. C. Pandey. Variable stars in young open star cluster NGC 7380. *Monthly Notices of the RAS*, 456(3):2505–2517, March 2016.
- [25] Janet Rountree Lesh. The Kinematics of the Gould Belt: an Expanding Group? *Astrophysical Journal, Supplement*, 17:371, December 1968.
- [26] W. W. Morgan and P. C. Keenan. Spectral Classification. *Annual Review of Astronomy and Astrophysics*, 11:29, January 1973.
- [27] W. W. Morgan and Nancy G. Roman. Revised Standards for Supergiants on the System of the Yerkes Spectral Atlas. *Astrophysical Journal*, 112:362–364, November 1950.
- [28] Giacomo Mulas, Giuliano Mallocci, Christine Joblin, and Cesare Cecchi-Pestellini. Polycyclic aromatic hydrocarbons and the extinction curve. volume 46, pages 327–340, 03 2011.
- [29] NASA - Goddard Space Flight Center. Lambda - data products, November 2010.
- [30] National Astronomical Observatory of Japan. Japanese amateur astronomer discovers new nova in cassiopeia, March 2021.
- [31] M. A. C. Perryman, L. Lindegren, J. Kovalevsky, E. Hog, U. Bastian, P. L. Bernacca, M. Creze, F. Donati, M. Grenon, M. Grewing, F. van Leeuwen, H. van der Marel, F. Mignard, C. A. Murray, R. S. Le Poole, H. Schrijver, C. Turon, F. Arenou, M. Froeschle, and C. S. Petersen. The Hipparcos Catalogue. *Astronomy and Astrophysics*, 500:501–504, July 1997.
- [32] M. Pettini. Structure and evolution of stars.
- [33] Philipp Richter. Das interstellare medium der milchstra"se. *Sterne und Weltraum*, January 2006.
- [34] David J. Schlegel, Douglas P. Finkbeiner, and Marc Davis. Maps of dust infrared emission for use in estimation of reddening and cosmic microwave background radiation foregrounds. *The Astrophysical Journal*, 500(2):525–553, June 1998.
- [35] V. I. Shenavrin, O. G. Taranova, and A. E. Nadzhip. Search for and study of hot circumstellar dust envelopes. *Astronomy Reports*, 55(1):31–81, January 2011.
- [36] B. A. Skiff. VizieR Online Data Catalog: Catalogue of Stellar Spectral Classifications (Skiff, 2009-). *VizieR Online Data Catalog*, page B/mk, October 2014.
- [37] A. Slettebak. Spectral types and rotational velocities of the brighter be stars and a-f type shell stars. *The Astrophysical Journal Supplement Series*, 50:55, sep 1982.
- [38] A. Slettebak. Spectral types and rotational velocities of the brighter Be stars and A-F type shell stars. *Astrophysical Journal, Supplement*, 50:55–83, September 1982.

- [39] A. Sota, J. Maíz Apellániz, N. I. Morrell, R. H. Barbá, N. R. Walborn, R. C. Gamen, J. I. Arias, and E. J. Alfaro. The Galactic O-Star Spectroscopic Survey (GOSSS). II. Bright Southern Stars. *Astrophysical Journal, Supplement*, 211(1):10, March 2014.
- [40] A. Sota, J. Maíz Apellániz, N. R. Walborn, E. J. Alfaro, R. H. Barbá, N. I. Morrell, R. C. Gamen, and J. I. Arias. The Galactic O-Star Spectroscopic Survey. I. Classification System and Bright Northern Stars in the Blue-violet at $R \sim 2500$. *Astrophysical Journal, Supplement*, 193(2):24, April 2011.
- [41] F. van Leeuwen. Validation of the new hipparcos reduction. *Astronomy & Astrophysics*, 474(2):653–664, aug 2007.
- [42] Alfred Weigert, Heinrich J. Wendker, and Lutz Wisotzki. *Astronomie und Astrophysik - Ein Grundkurs*. John Wiley & Sons, New York, 2012.
- [43] Winkel, B., Kerp, J., Flöer, L., Kalberla, P. M. W., Ben Bekhti, N., Keller, R., and Lenz, D. The effelsberg-bonn hurvey: Milky way gas - first data release. *A&A*, 585:A41, 2016.

AAVSO - Visual Magnitudes

In Table 2, where we compiled the results of our observations, the apparent V-band magnitudes are given. Of course, this is also the case for the nova-type V1405 Cas variable star. Given its significantly varying brightness over time, the respective m_V values were researched individually from the AAVSO database. This is because the stars system has not been monitored with the OST during our observation period with regard to photometry. The following screenshots should demonstrate to which individual observation the given m_V values refer.

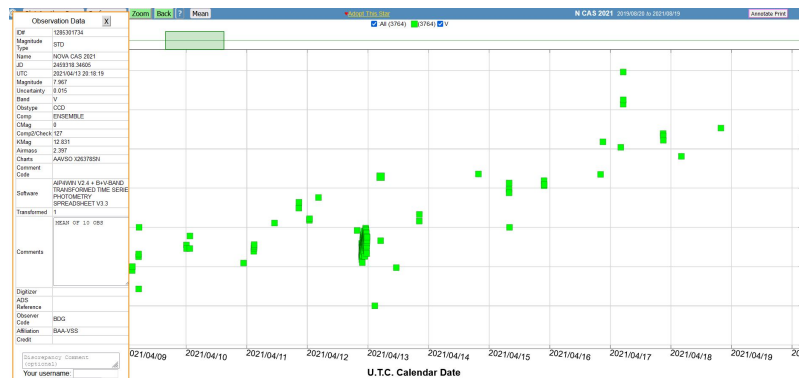


Figure 15.3: Associated data point for the OST observation, conducted on 2021-04-14.

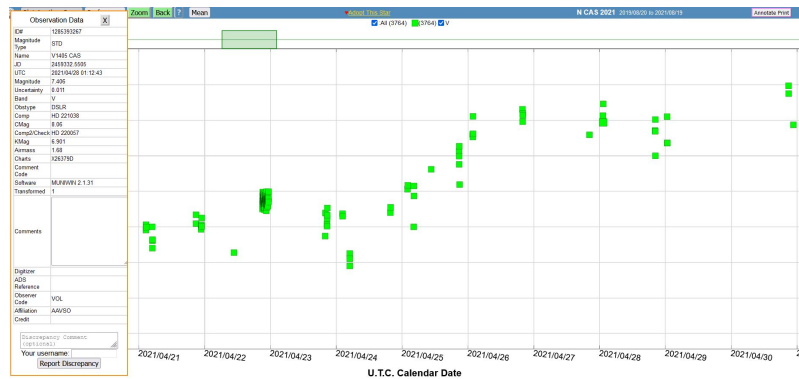


Figure 15.4: Associated data point for the OST observation, conducted on 2021-04-28.



Figure 15.5: Associated data point for the OST observation, conducted on 2021-05-10. According to the trend-line, the spectrum has been taken only a few days before the star's absolute brightness maximum.

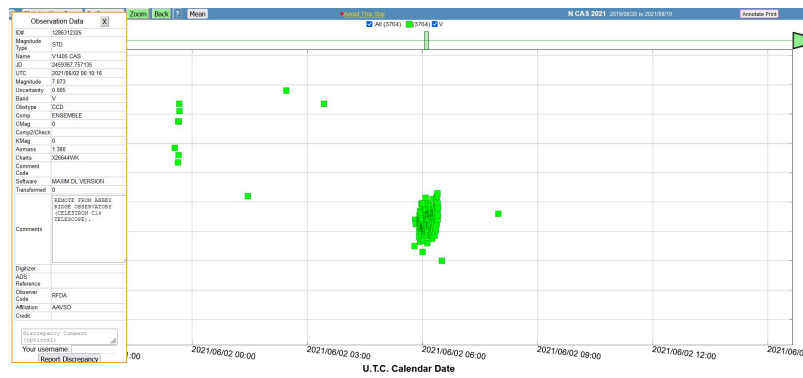


Figure 15.6: Associated data point for the OST observation, conducted on 2021-06-02.

16 Declaration of Originality

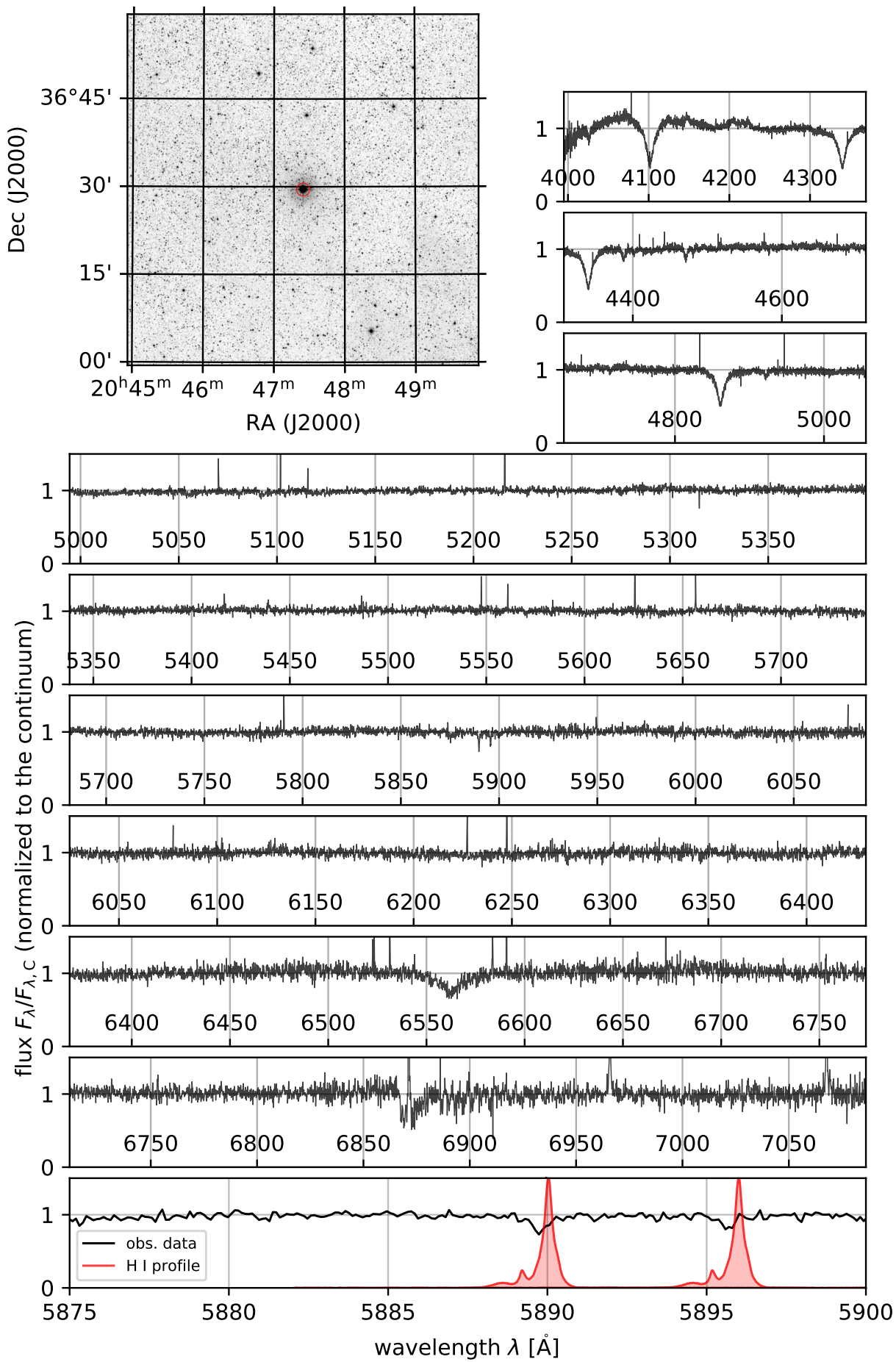
I herewith declare that I have written this thesis on my own and did not make use of any sources not mentioned in the literature. Citations in the text and figures like literature values or ideas of others are clearly marked as those in a scientifically correct manner. Furthermore, I declare that this thesis or parts of it have not been submitted to any other examination board before.

Florian Runger
Potsdam, September 29, 2021

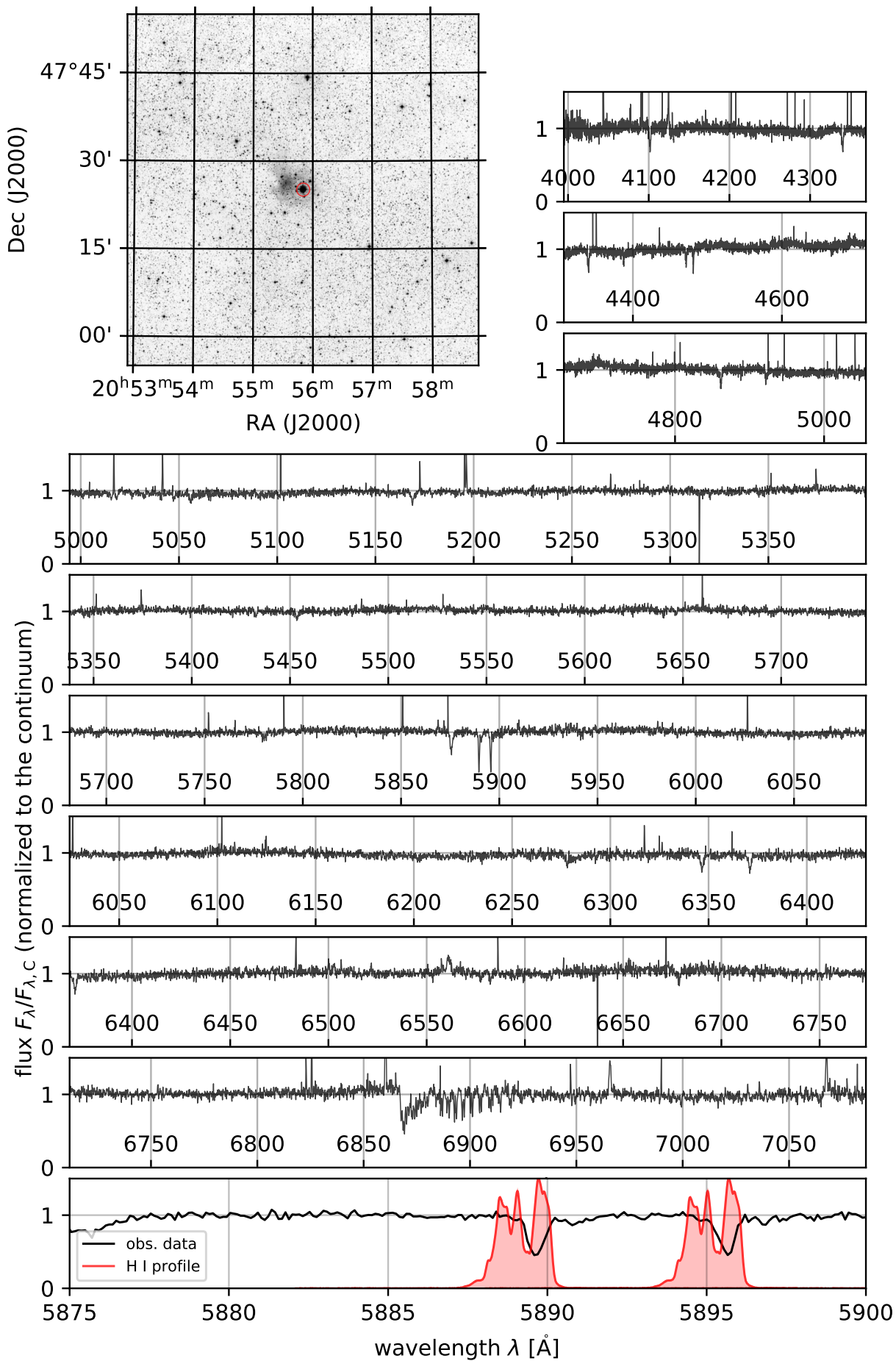
17 Star Spectra Plot Sheets

On the following pages, we can find plot sheets, including the whole star spectra, taken during our observations. In addition, there is also a small FOV, centered on each object, showing the vicinity of those stars. In some fortunate cases, we might be able to get an idea of where the ISM may originate from in this way. The images are retrieved from SIMBAD’s HIPS2FITS API and visualize the respective regions in the sky in the *DSS2/red* survey. It was accessed through the `astroquery` Python package.

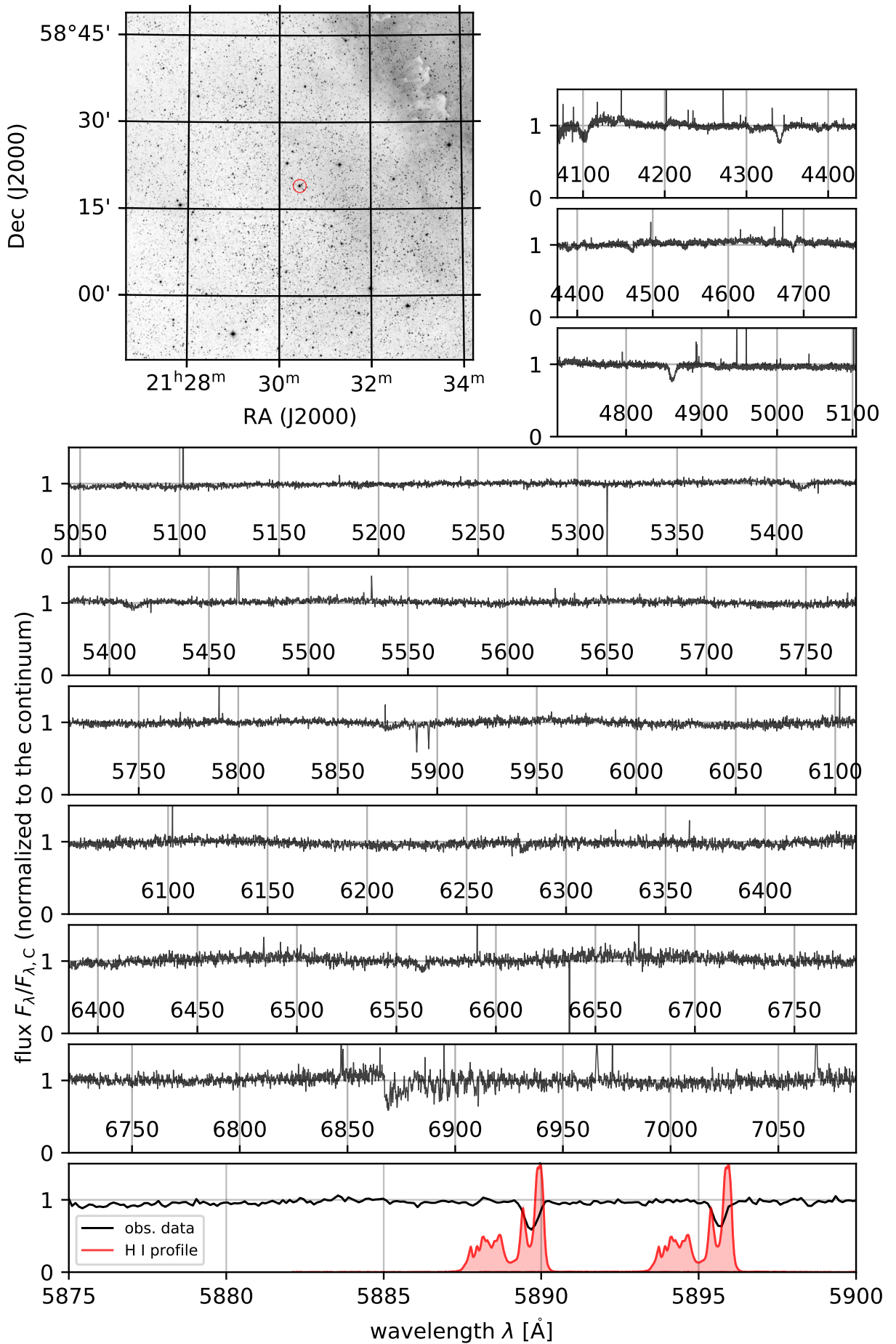
#1 - HIP102589
2021-04-28 01:38:22.848007 UTC



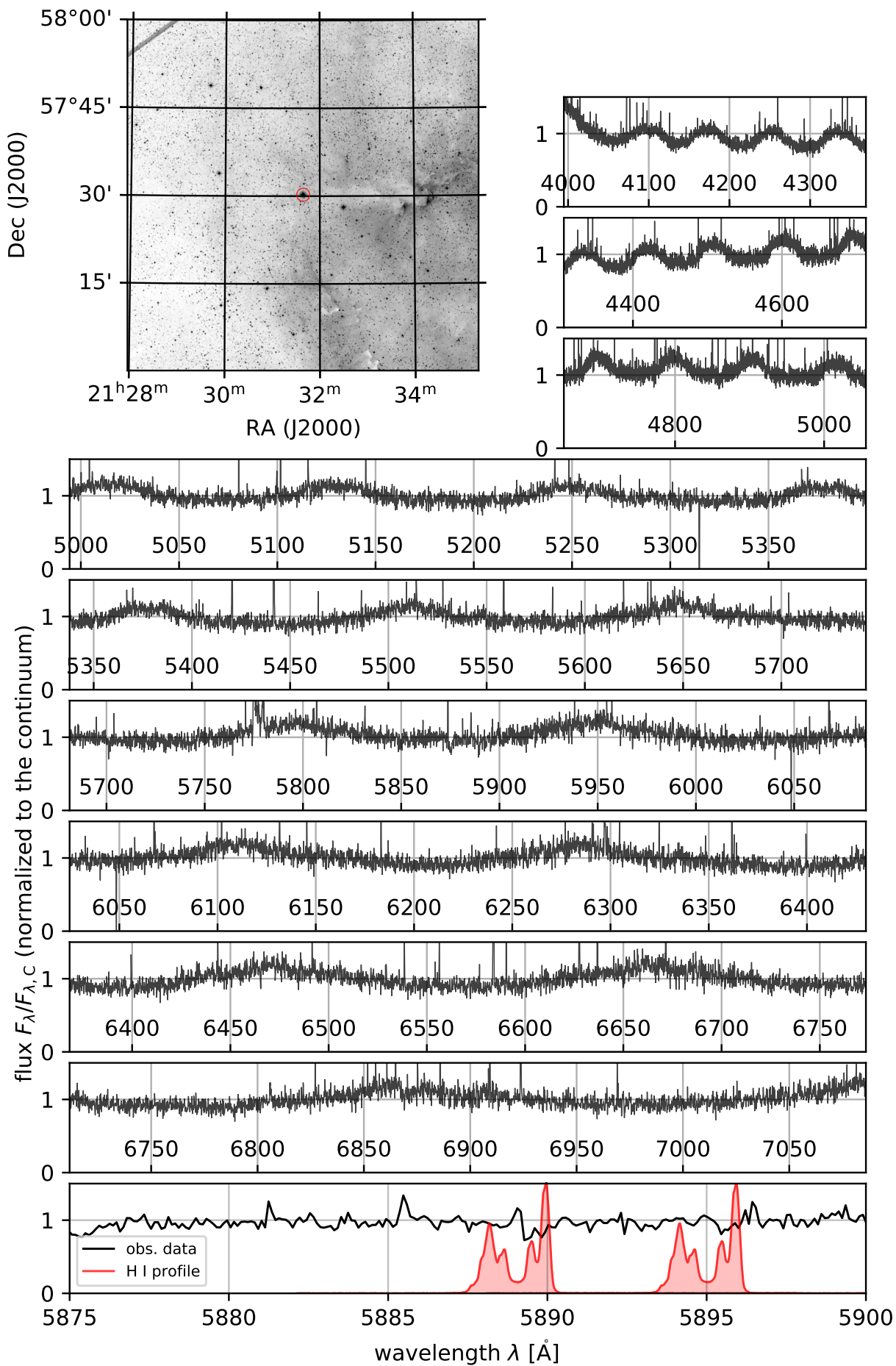
#2 - HIP103312
2021-04-27 23:20:03.264016 UTC



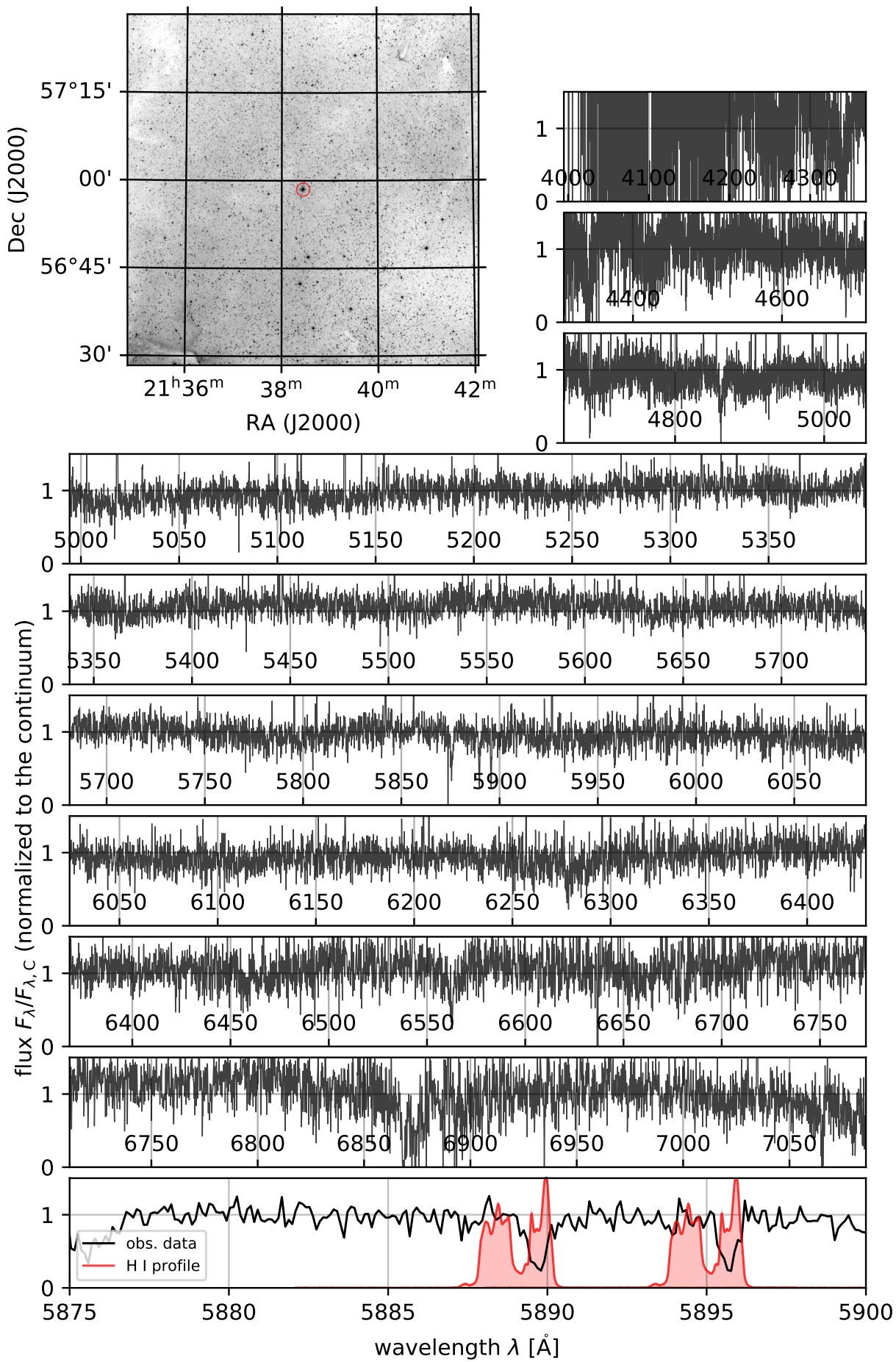
#3 - HIP106186
2021-04-27 23:43:26.399998 UTC



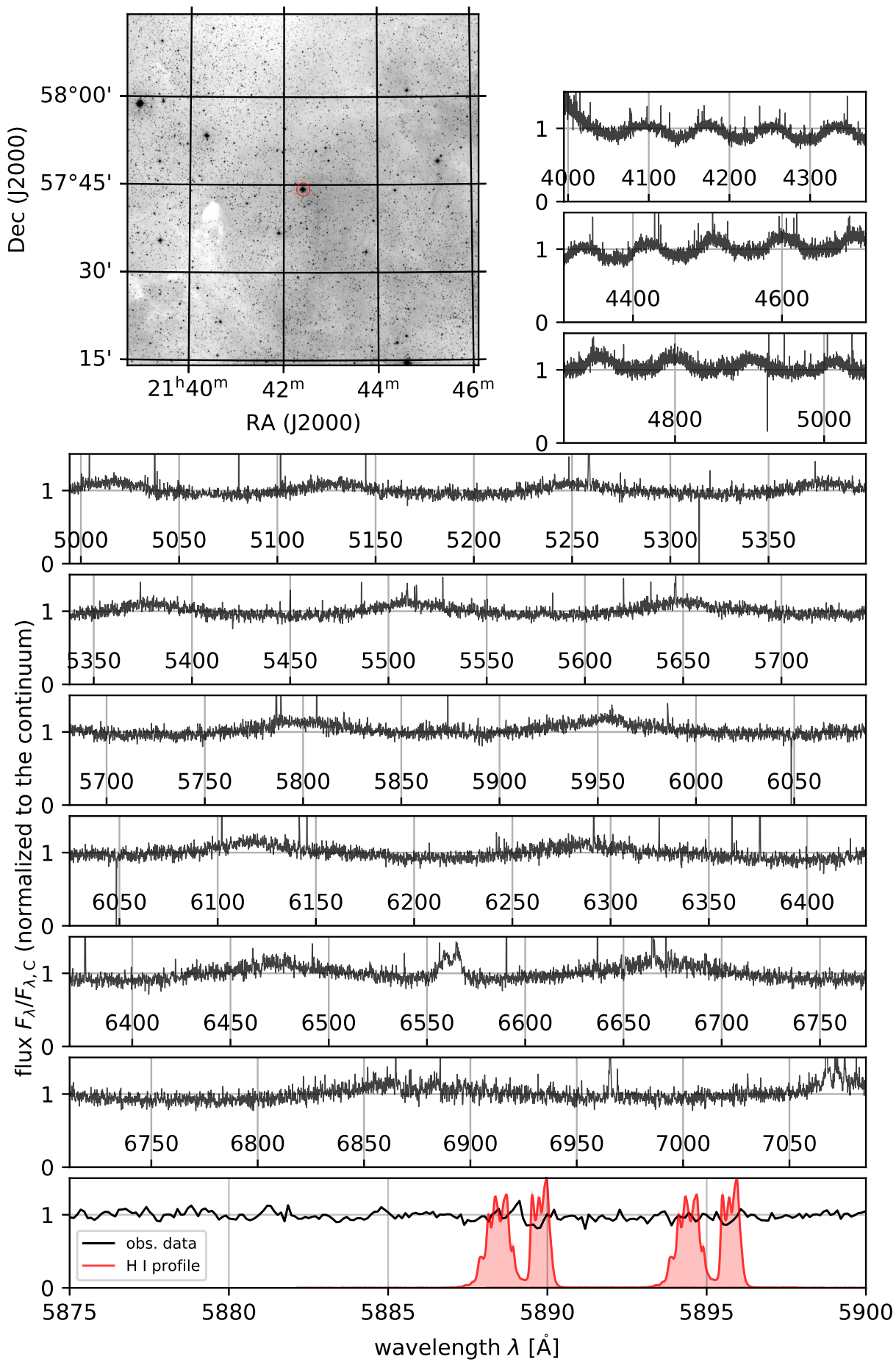
#4 - HIP106285
2021-04-27 20:34:41.951988 UTC



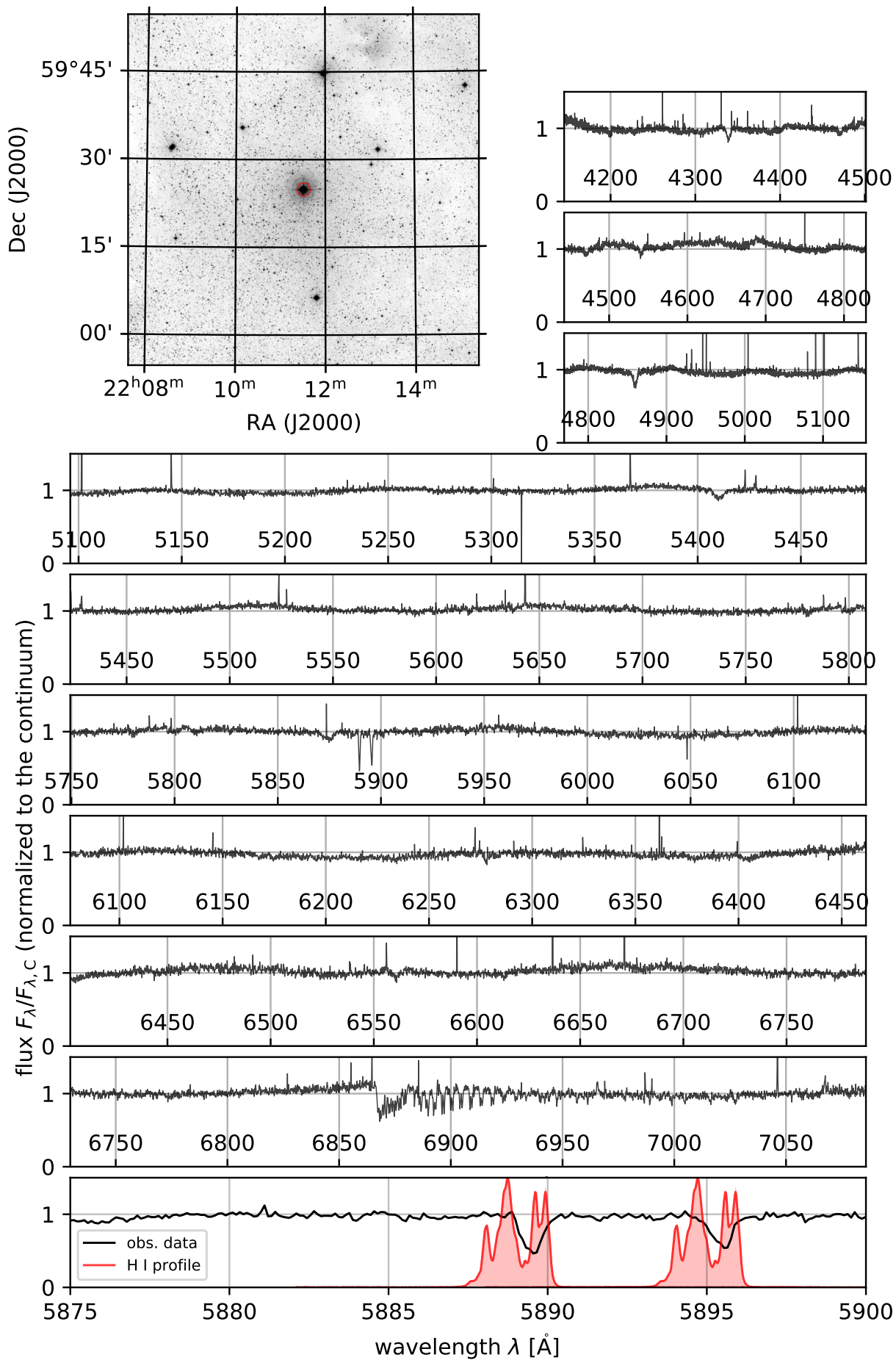
#5 - HIP106843
2021-04-27 21:28:55.775980 UTC



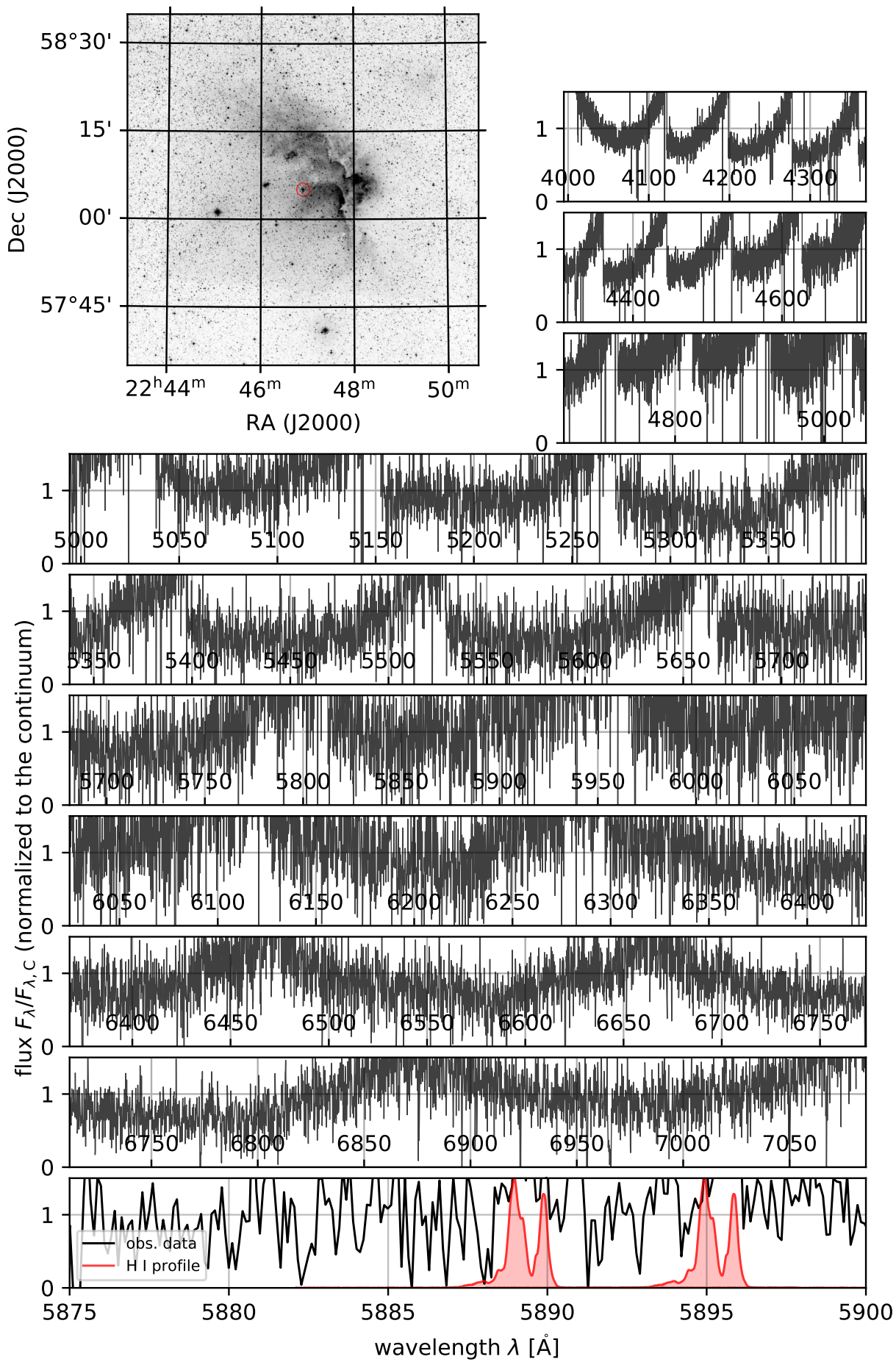
#6 - HIP107164
2021-04-27 20:58:36.192006 UTC



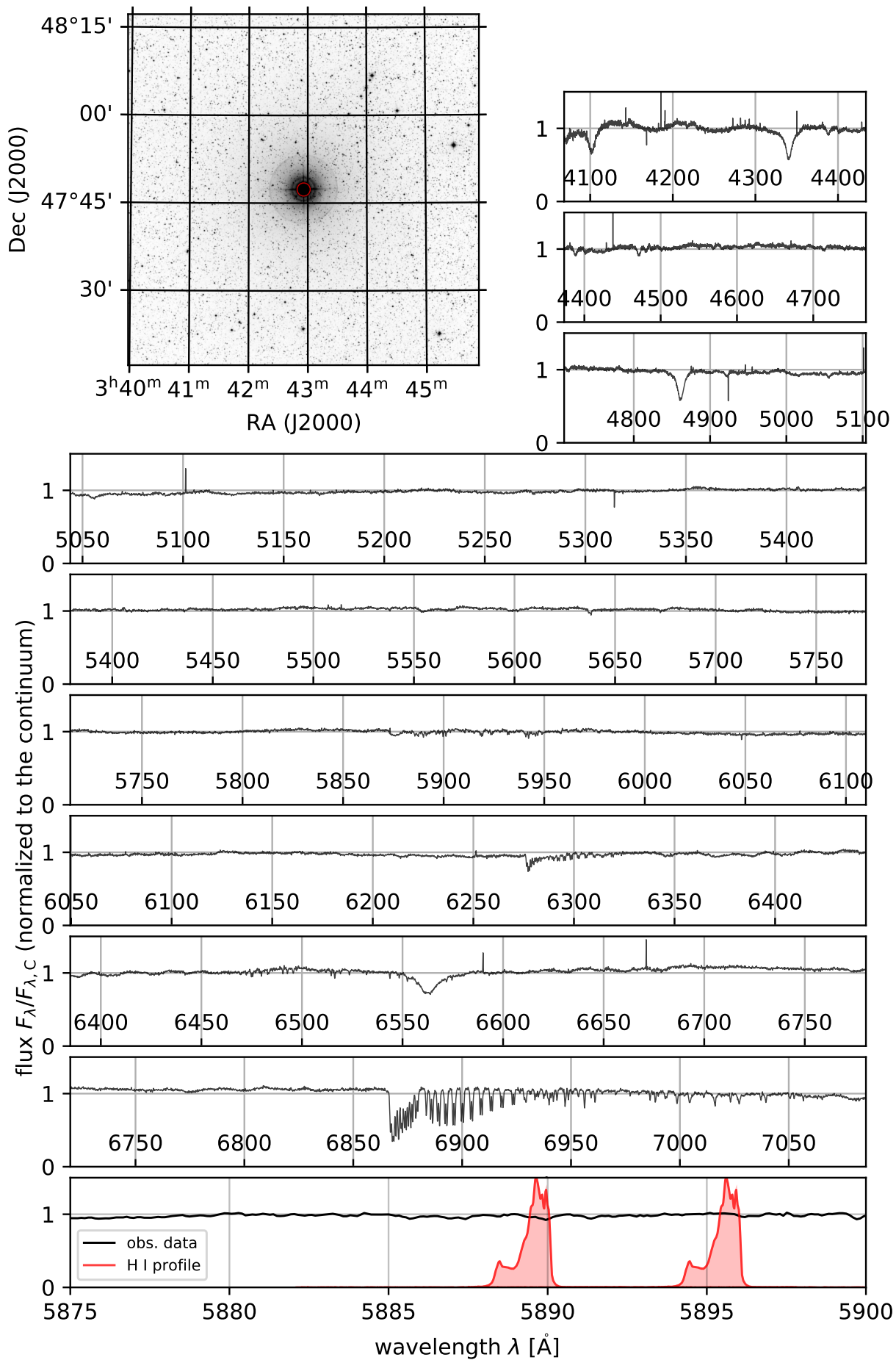
#7 - HIP109556
2021-04-27 20:11:20.544019 UTC



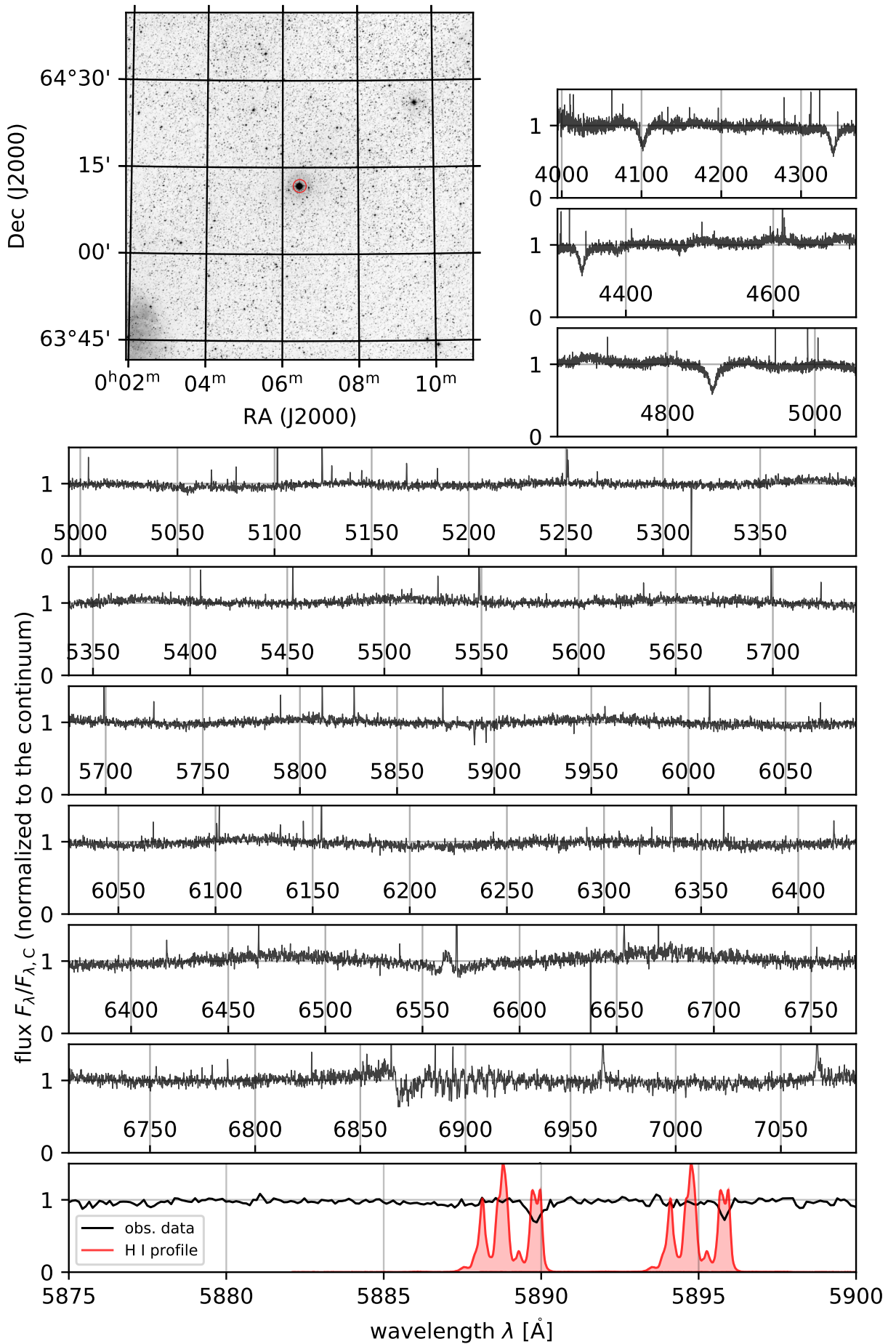
#8 - HIP112470
2021-04-28 00:11:20.831994 UTC



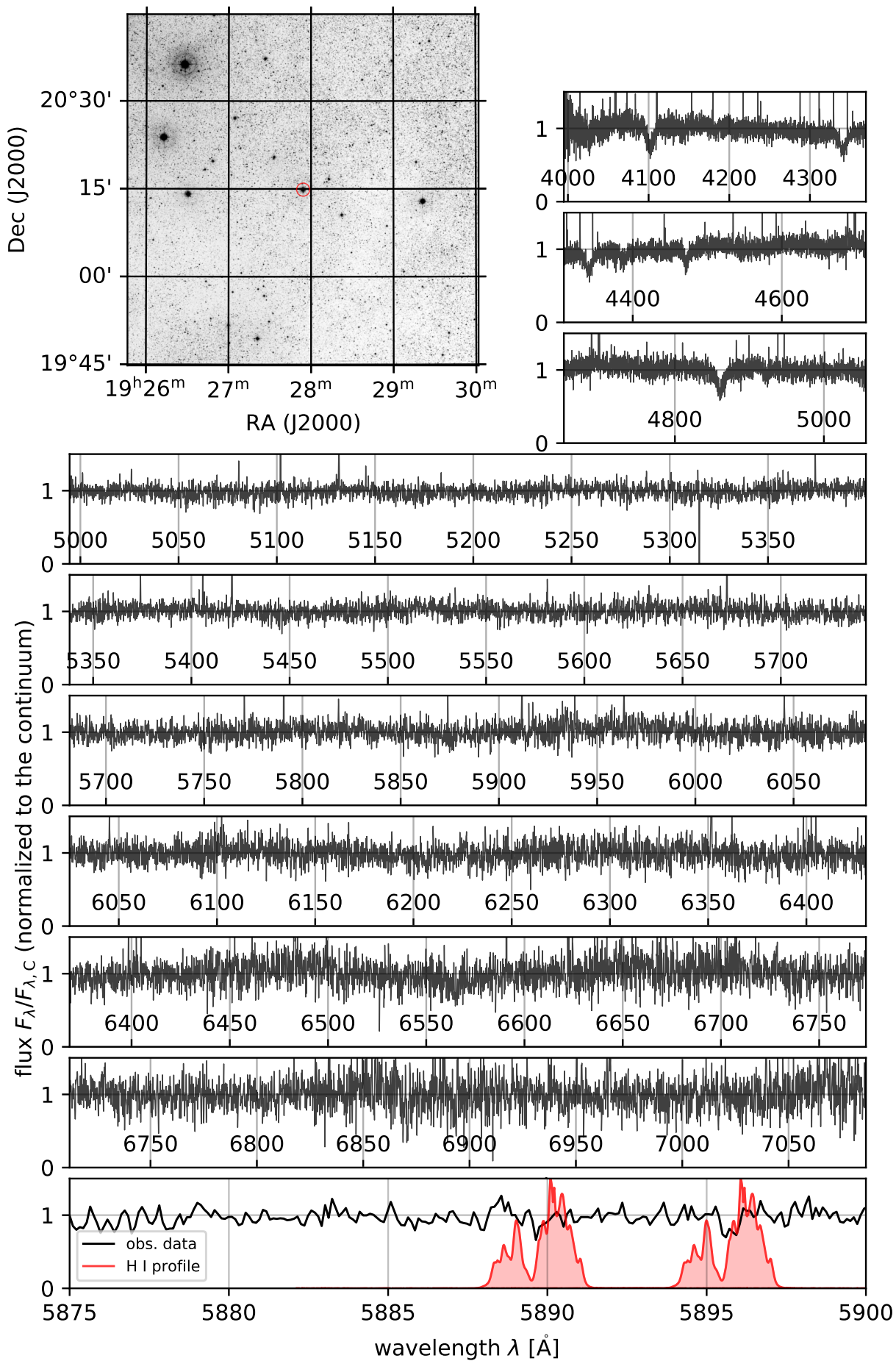
#9 - HIP17358
2021-04-27 19:45:52.128008 UTC



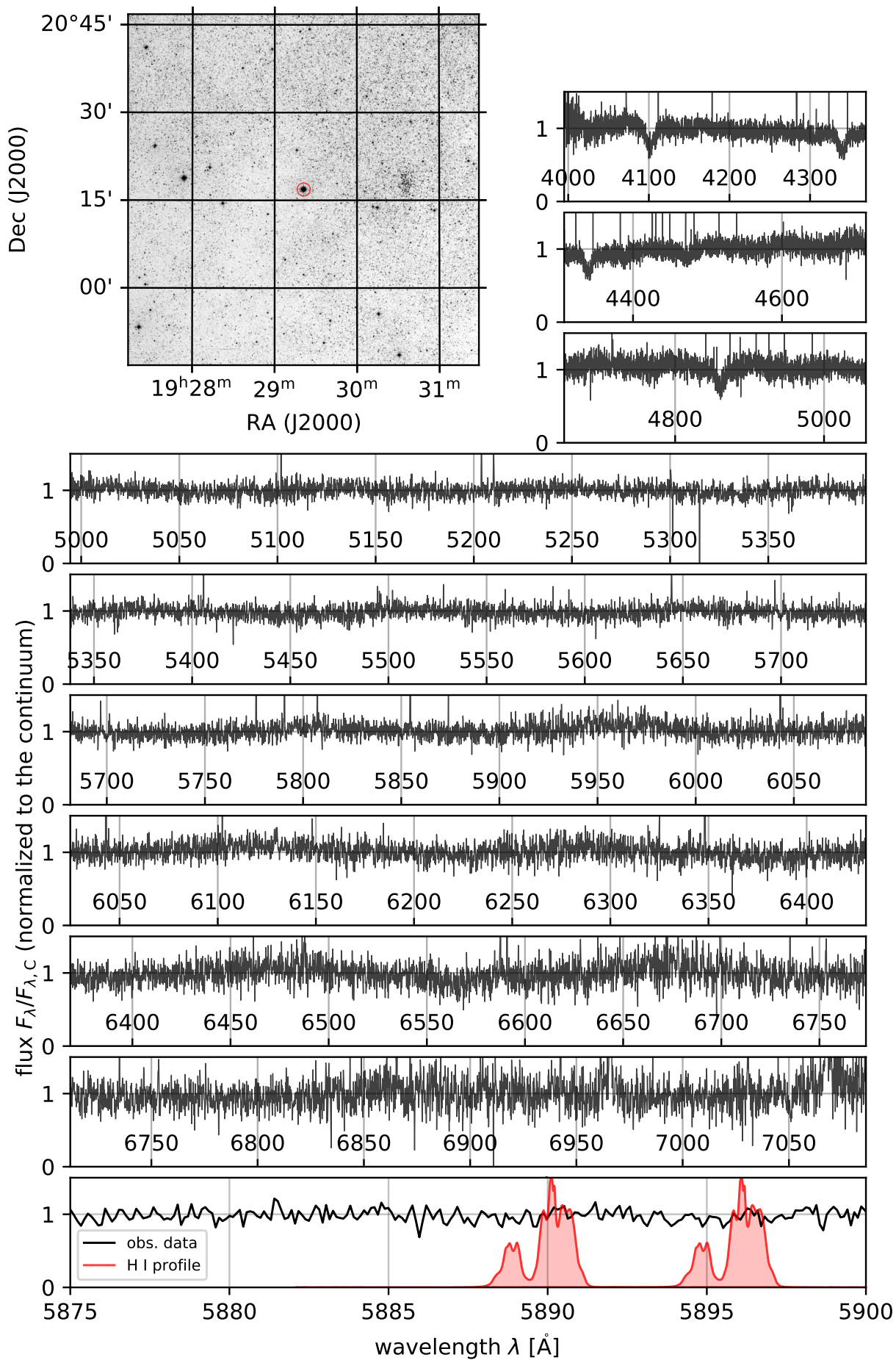
#10 - HIP531
2021-04-27 22:58:34.176017 UTC



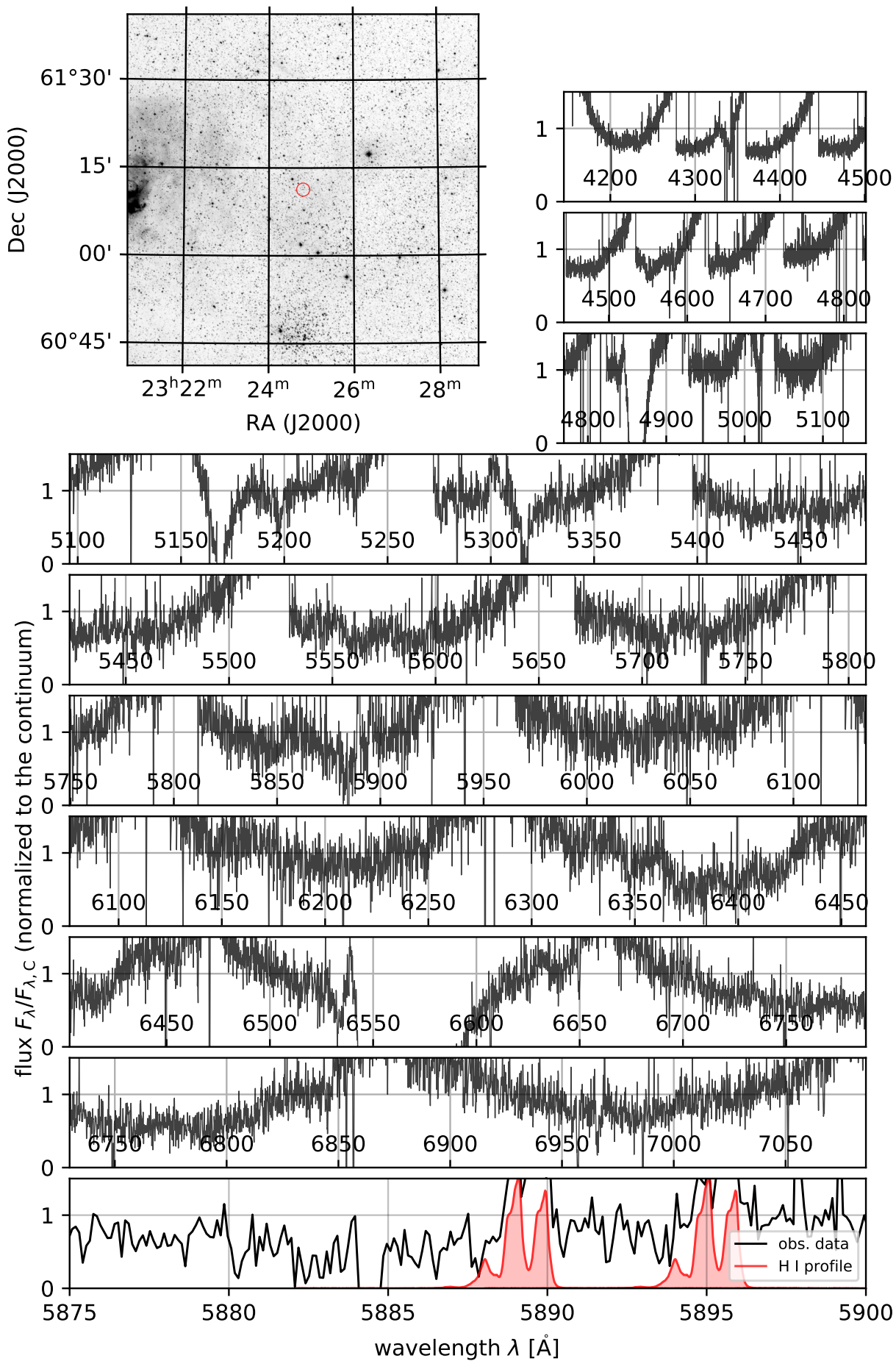
#11 - HIP95700
2021-04-28 00:54:12.096020 UTC



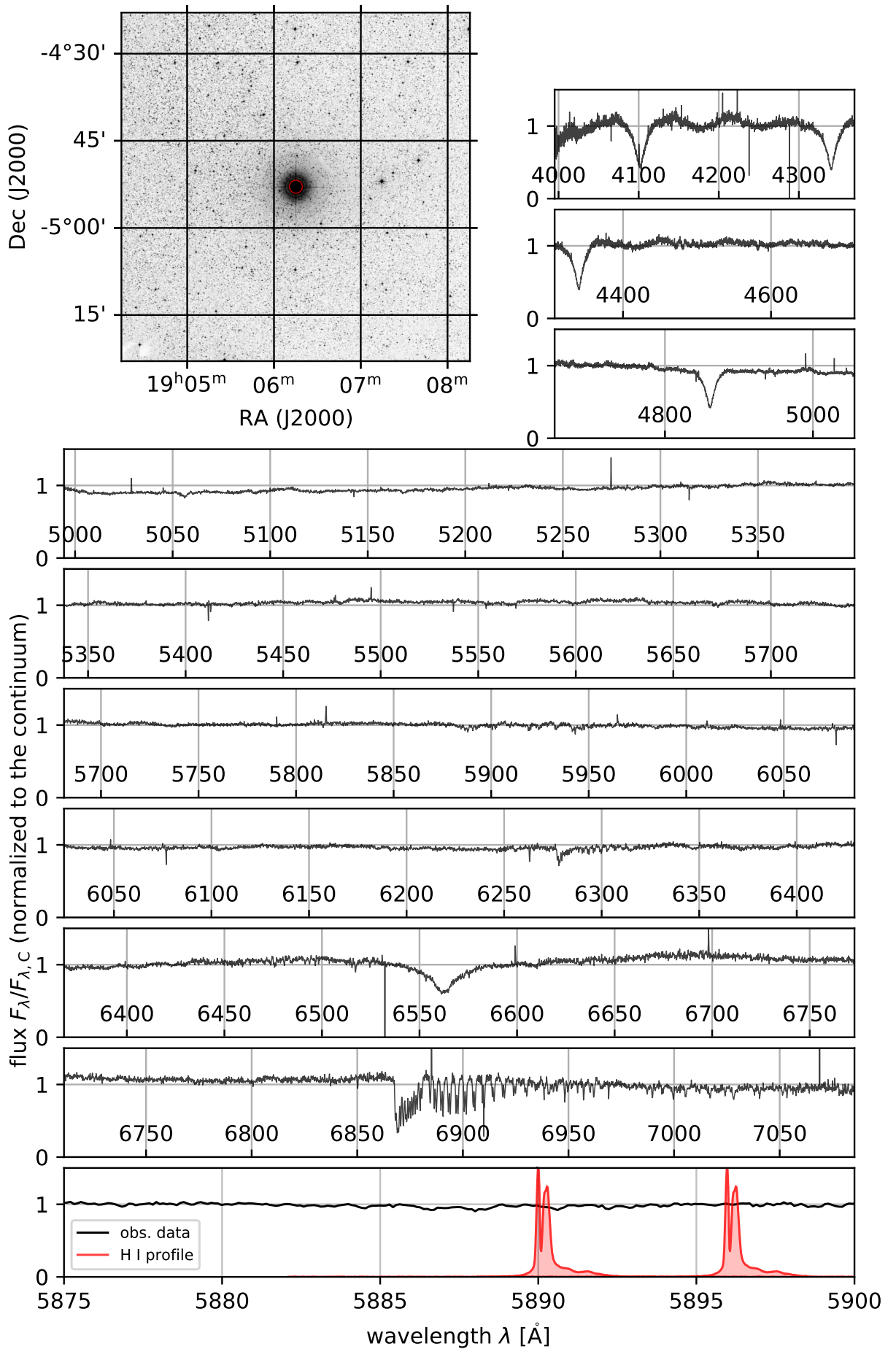
#12 - HIP95818
2021-04-28 01:16:28.704018 UTC



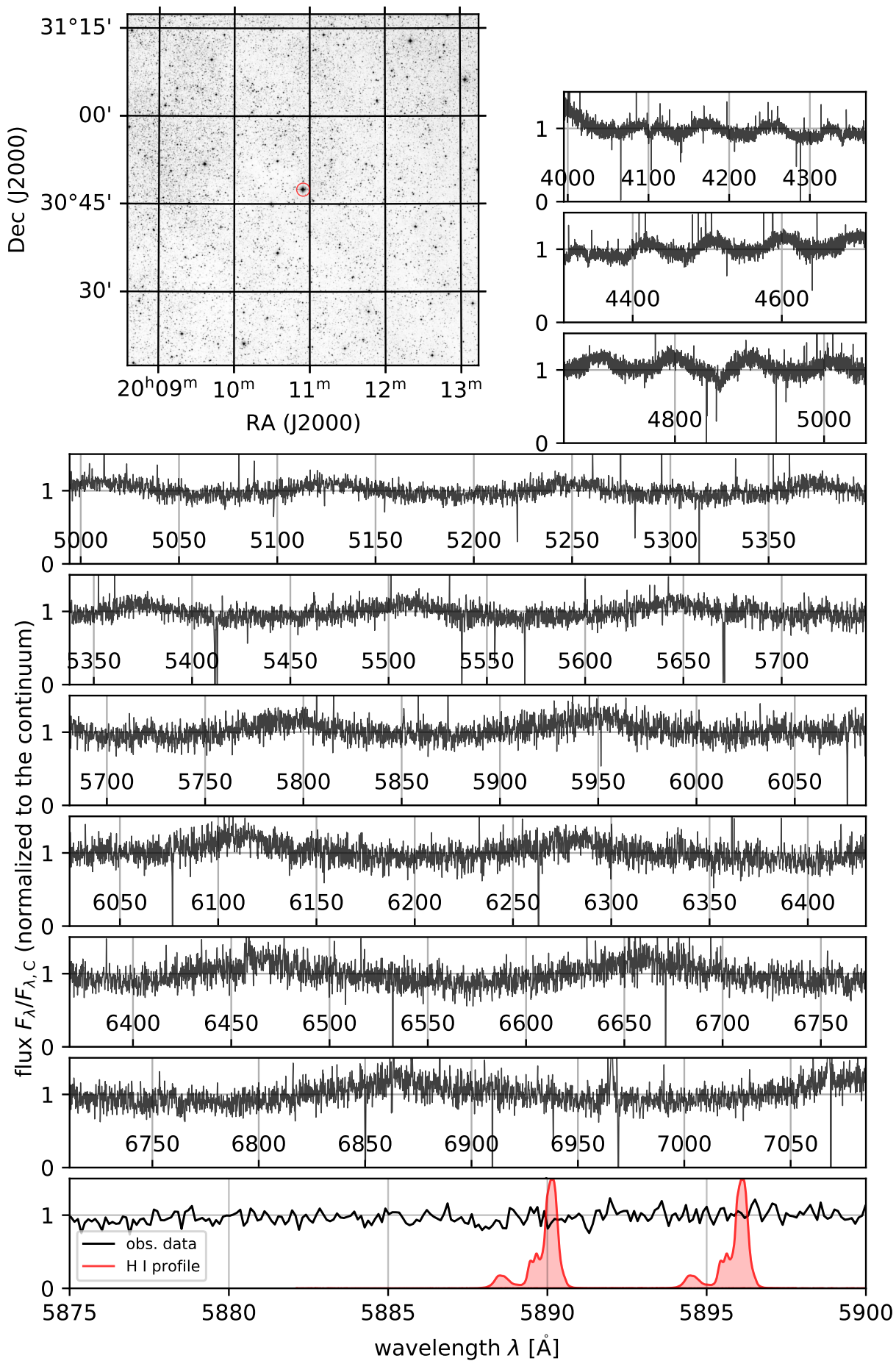
#13 - V1405Cas
2021-04-28 02:06:38.016000 UTC



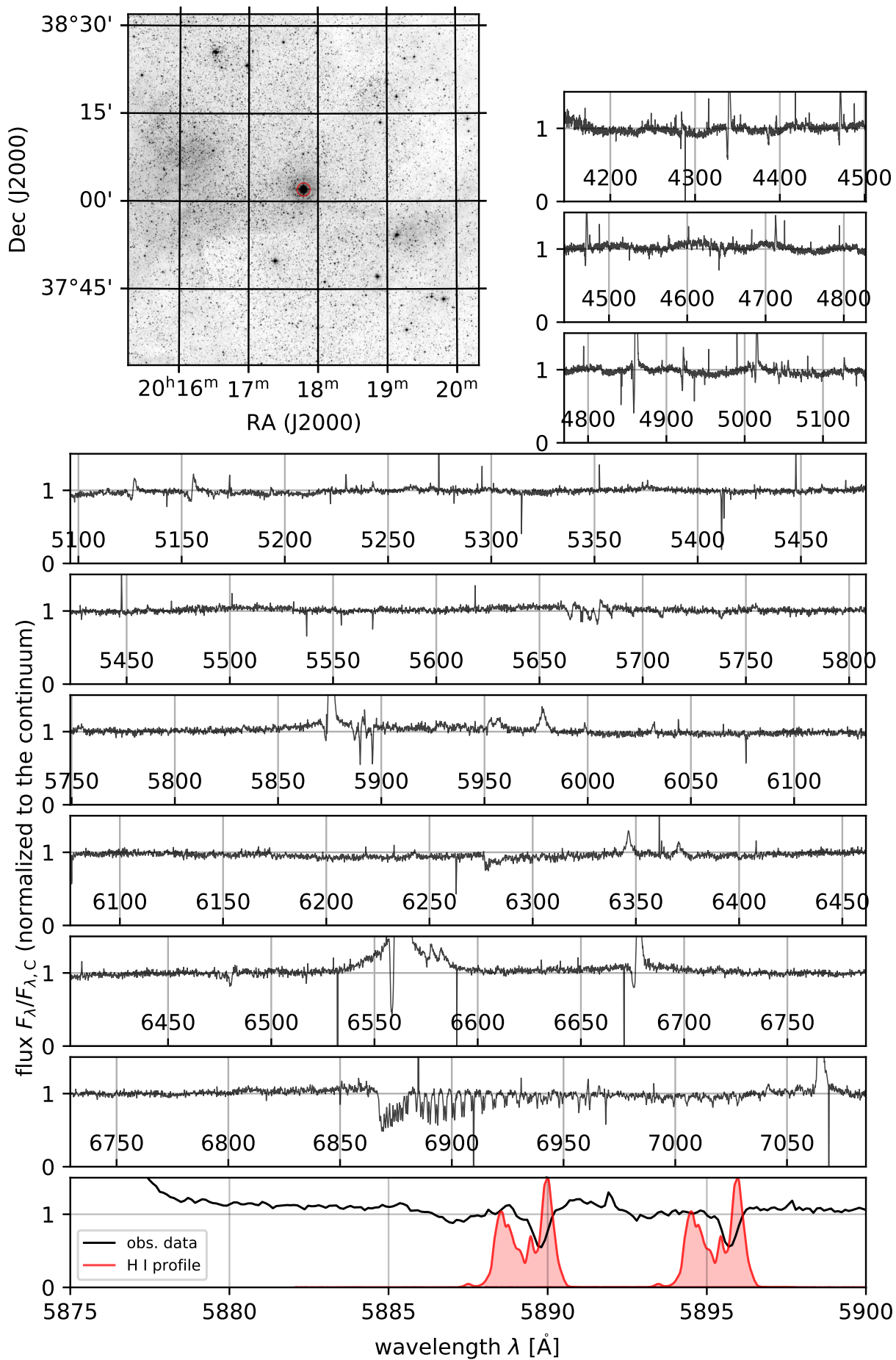
#14 - HIP93805
2021-04-27 01:46:11.999998 UTC



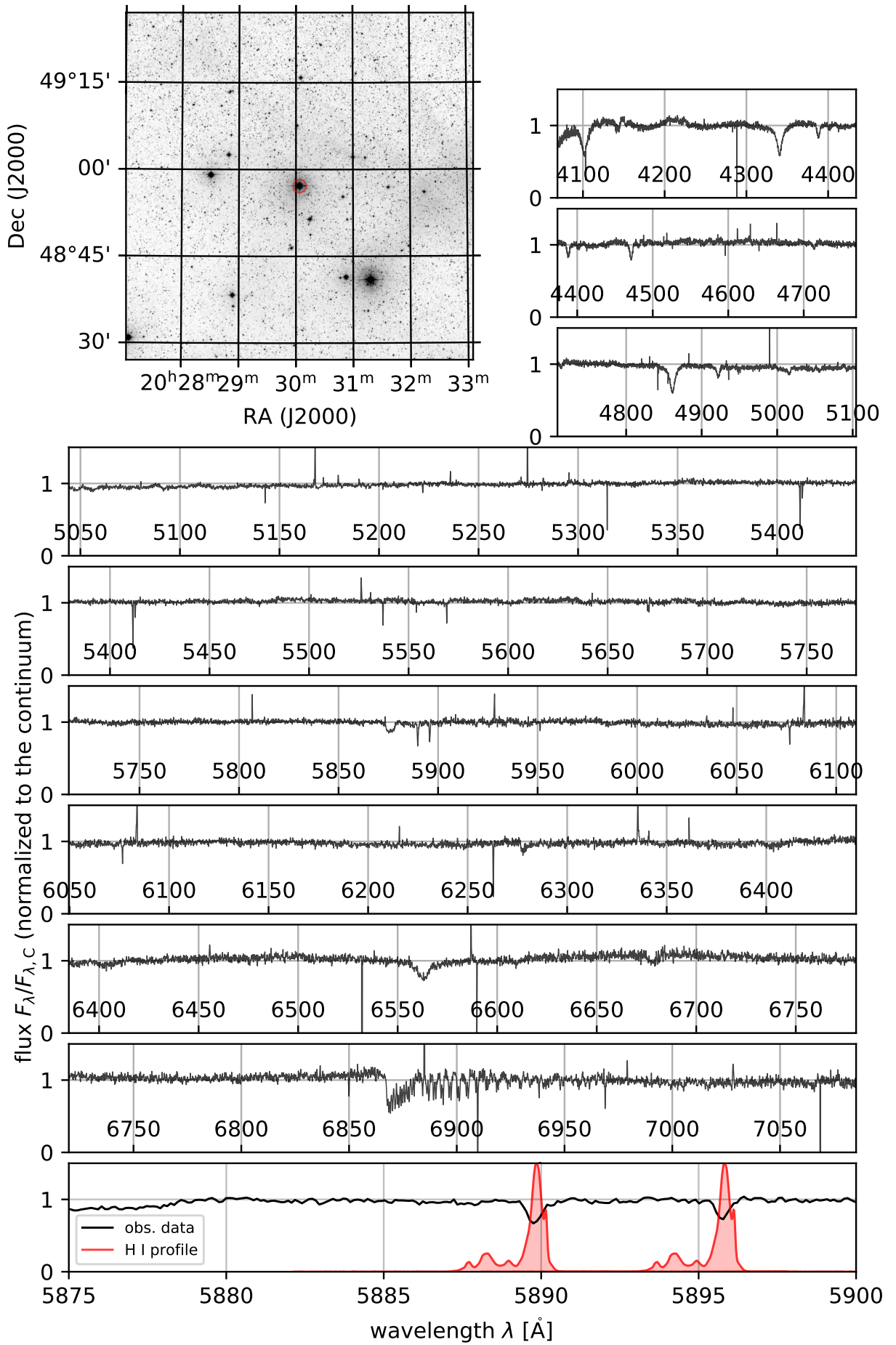
#15 - HIP99431
2021-04-26 23:42:25.919980 UTC



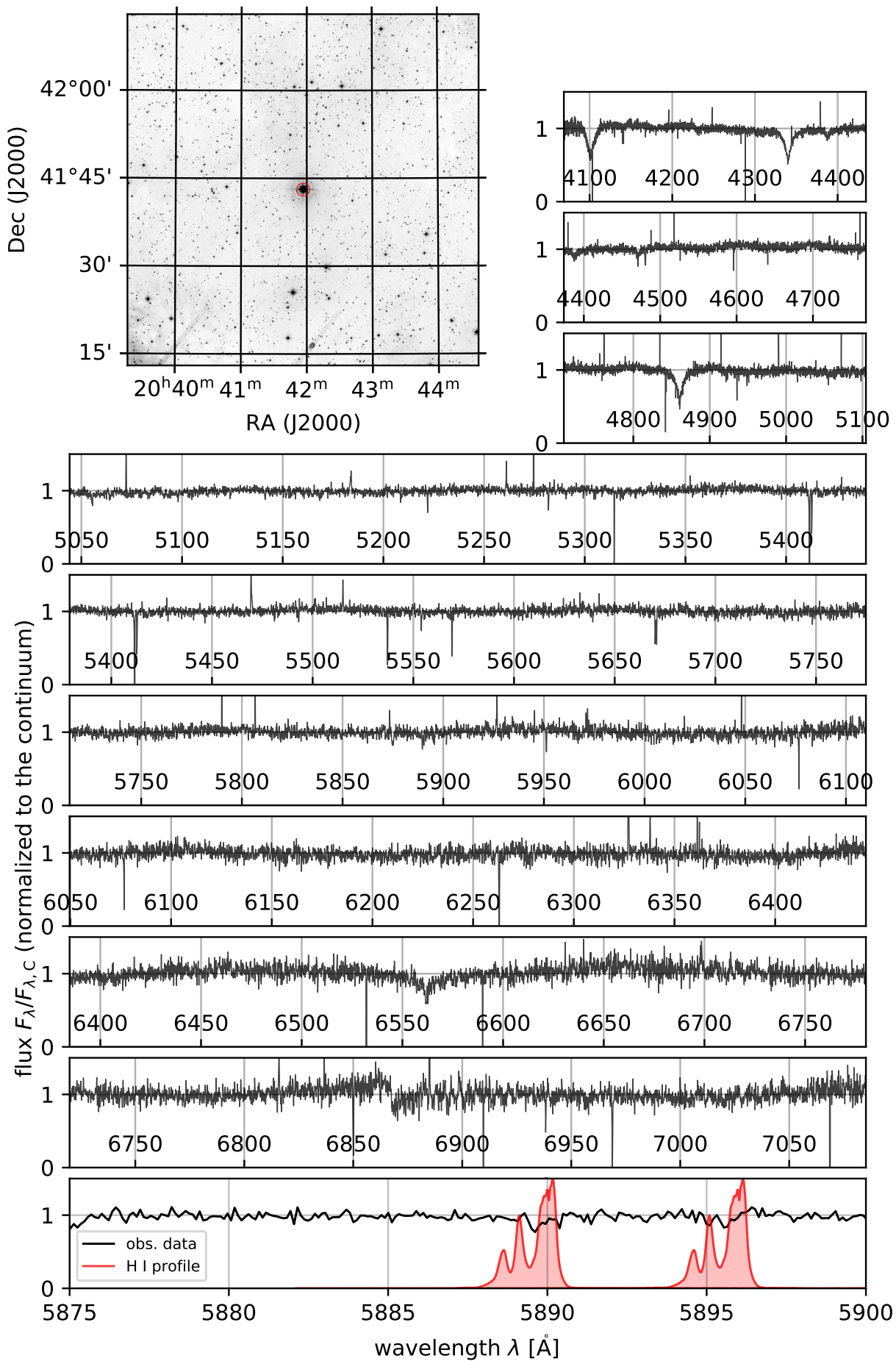
#16 - HIP100044
2021-04-26 22:18:11.519997 UTC



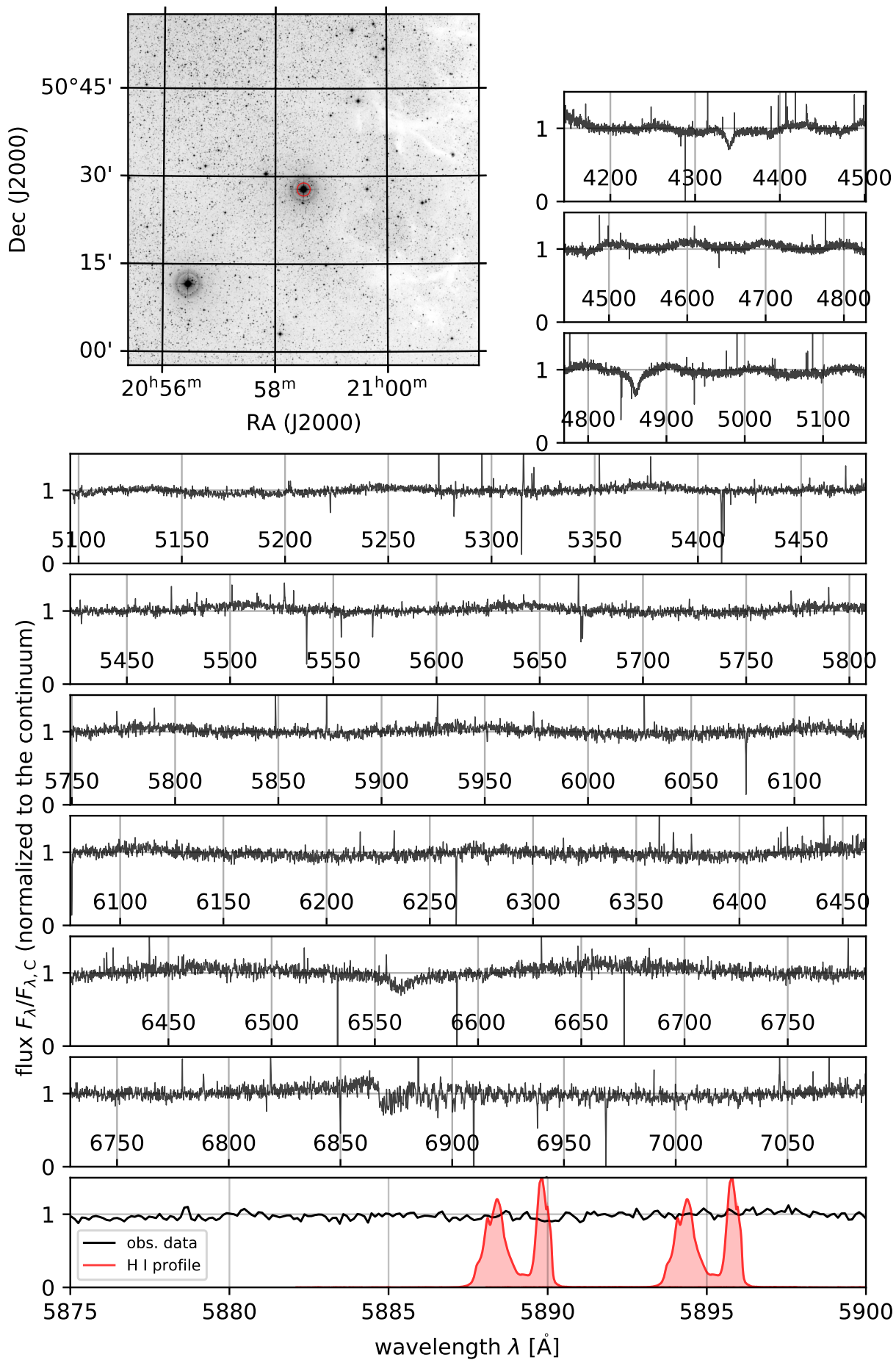
#17 - HIP101138
2021-04-27 00:08:52.223989 UTC



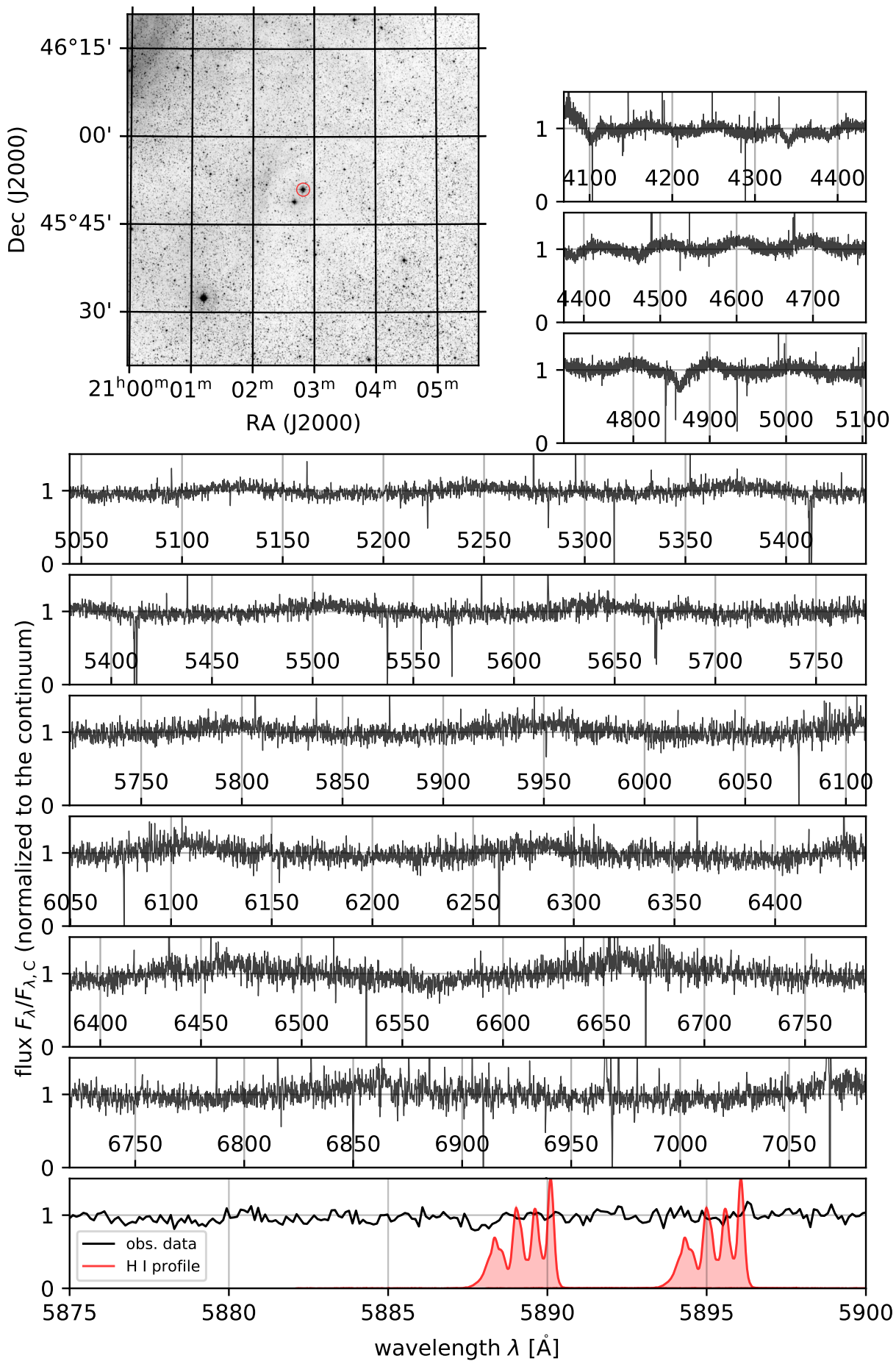
#18 - HIP102155
2021-04-27 00:38:57.120013 UTC



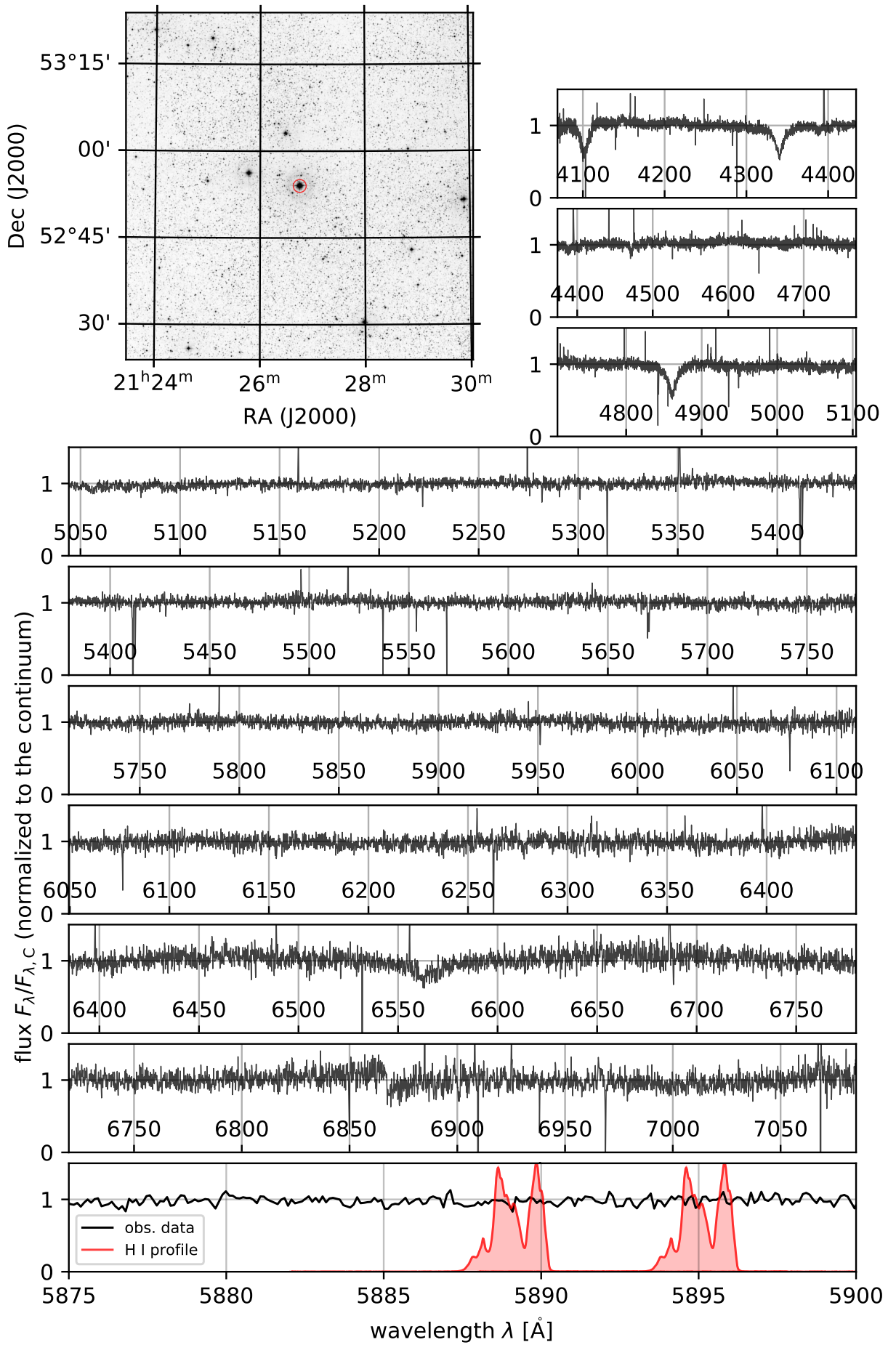
#19 - HIP103530
2021-04-26 21:50:12.768008 UTC



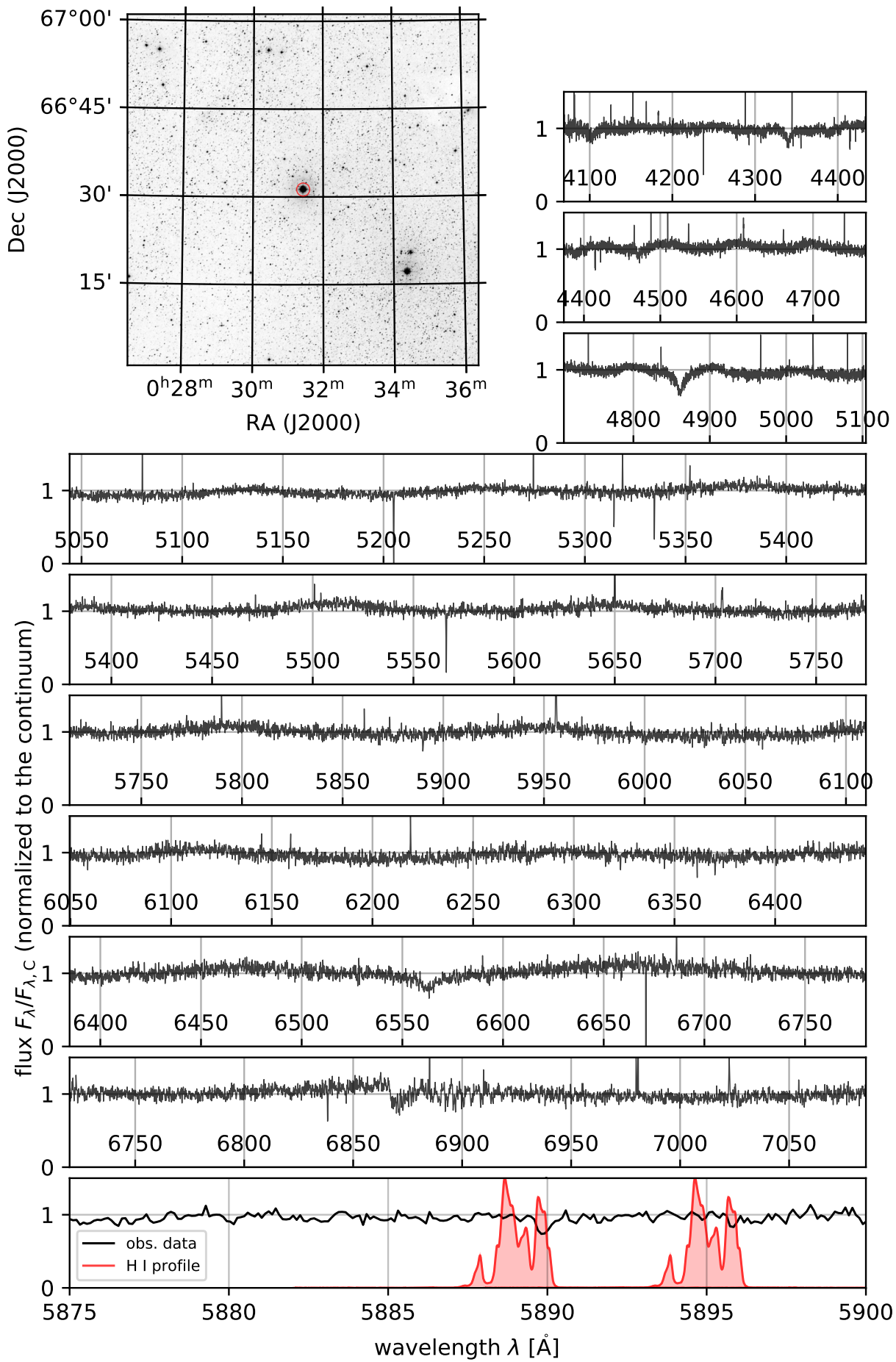
#20 - HIP103871
2021-04-26 23:15:47.520000 UTC



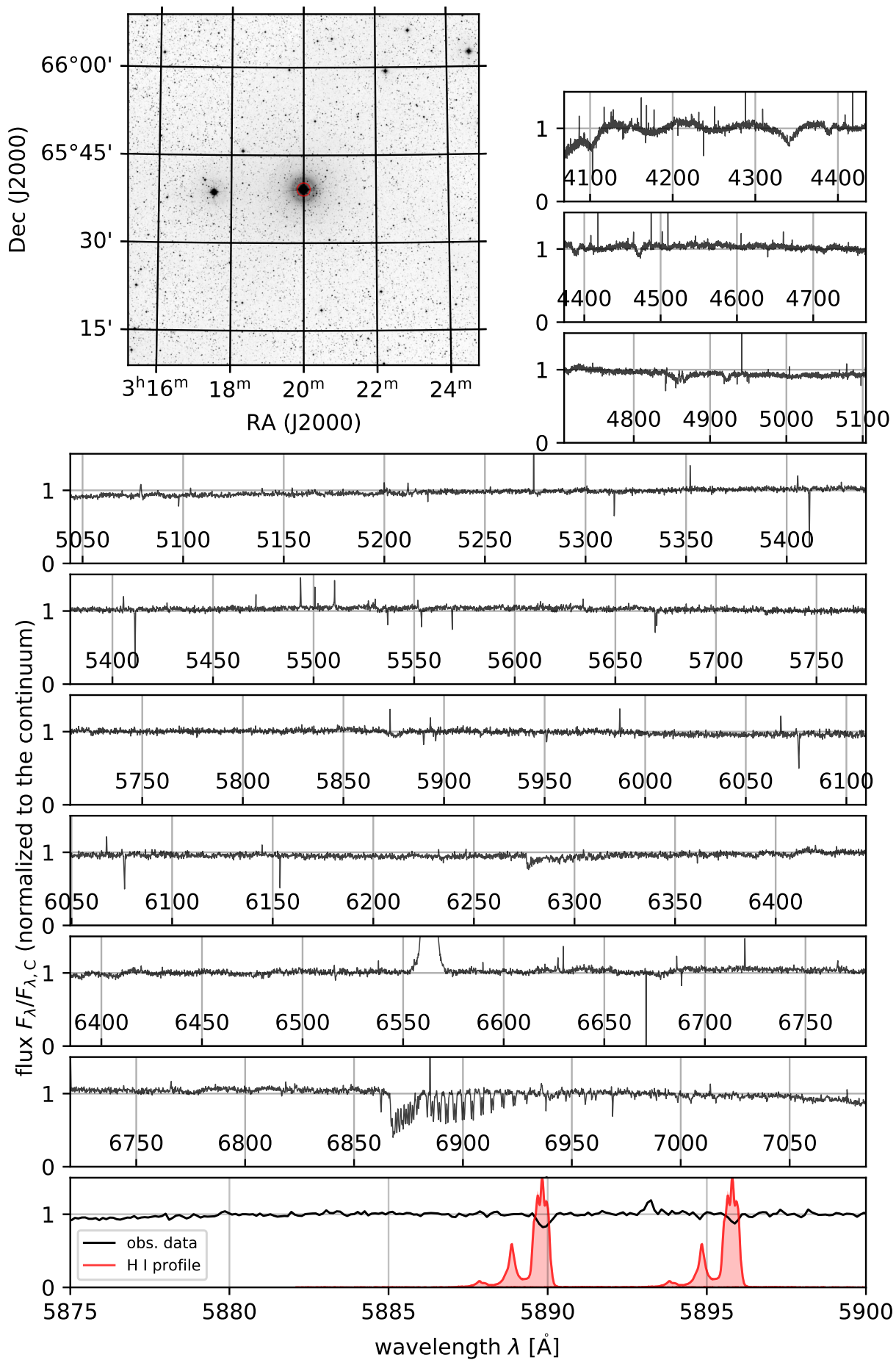
#21 - HIP105891
2021-04-27 01:05:11.328010 UTC



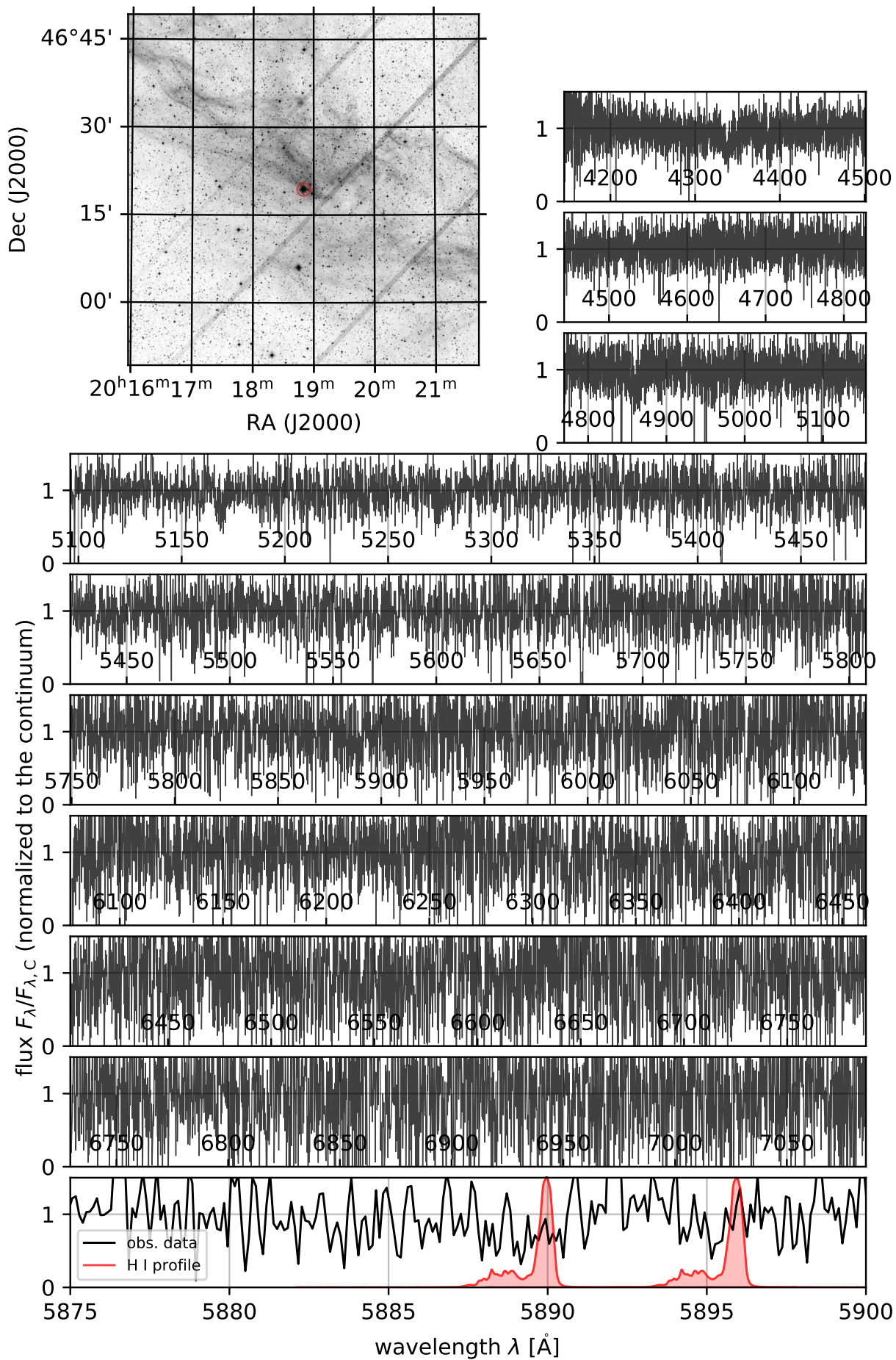
#22 - HIP2474
2021-04-25 20:57:47.807999 UTC



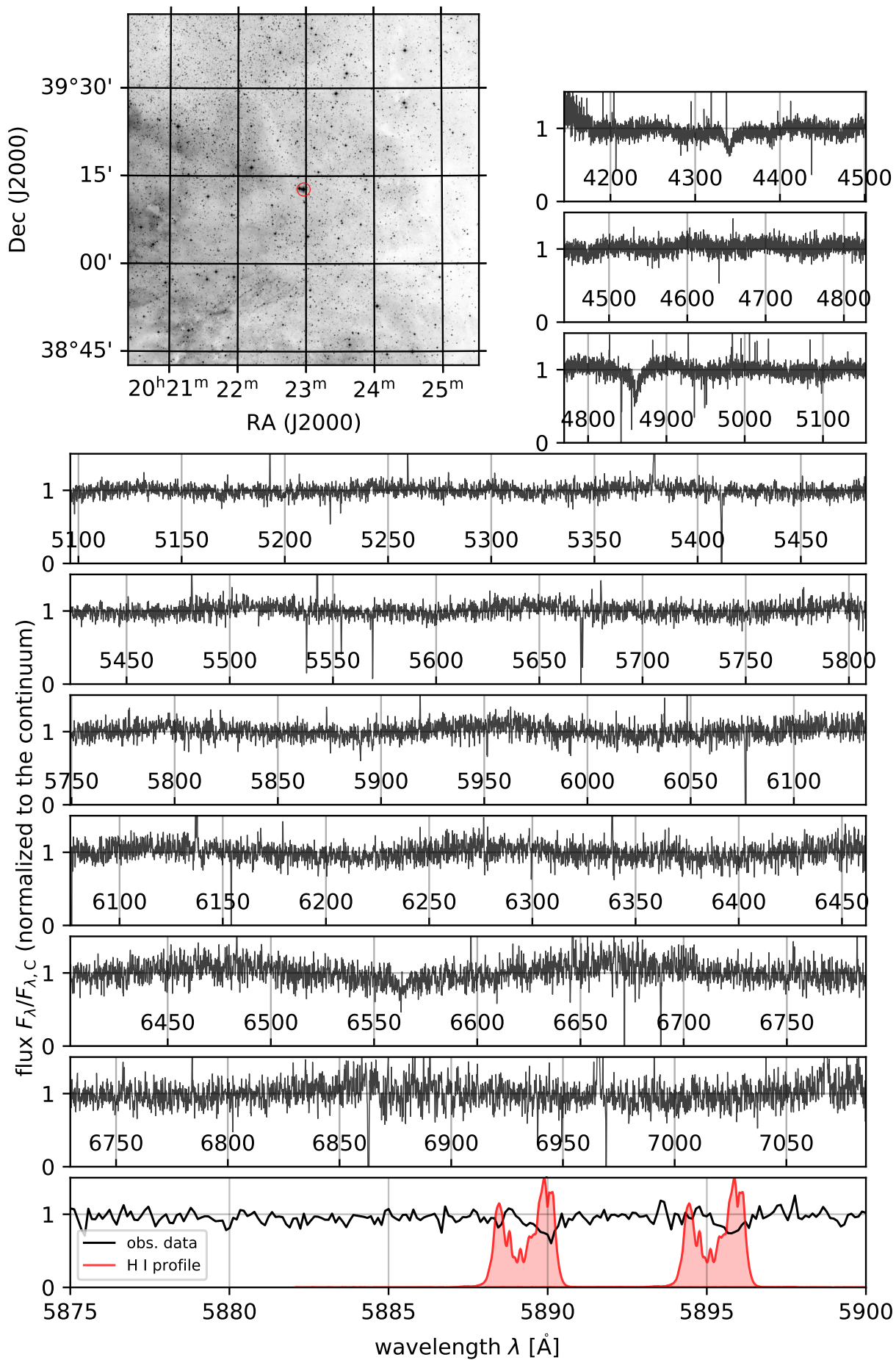
#23 - HIP15520
2021-04-25 21:33:59.039996 UTC



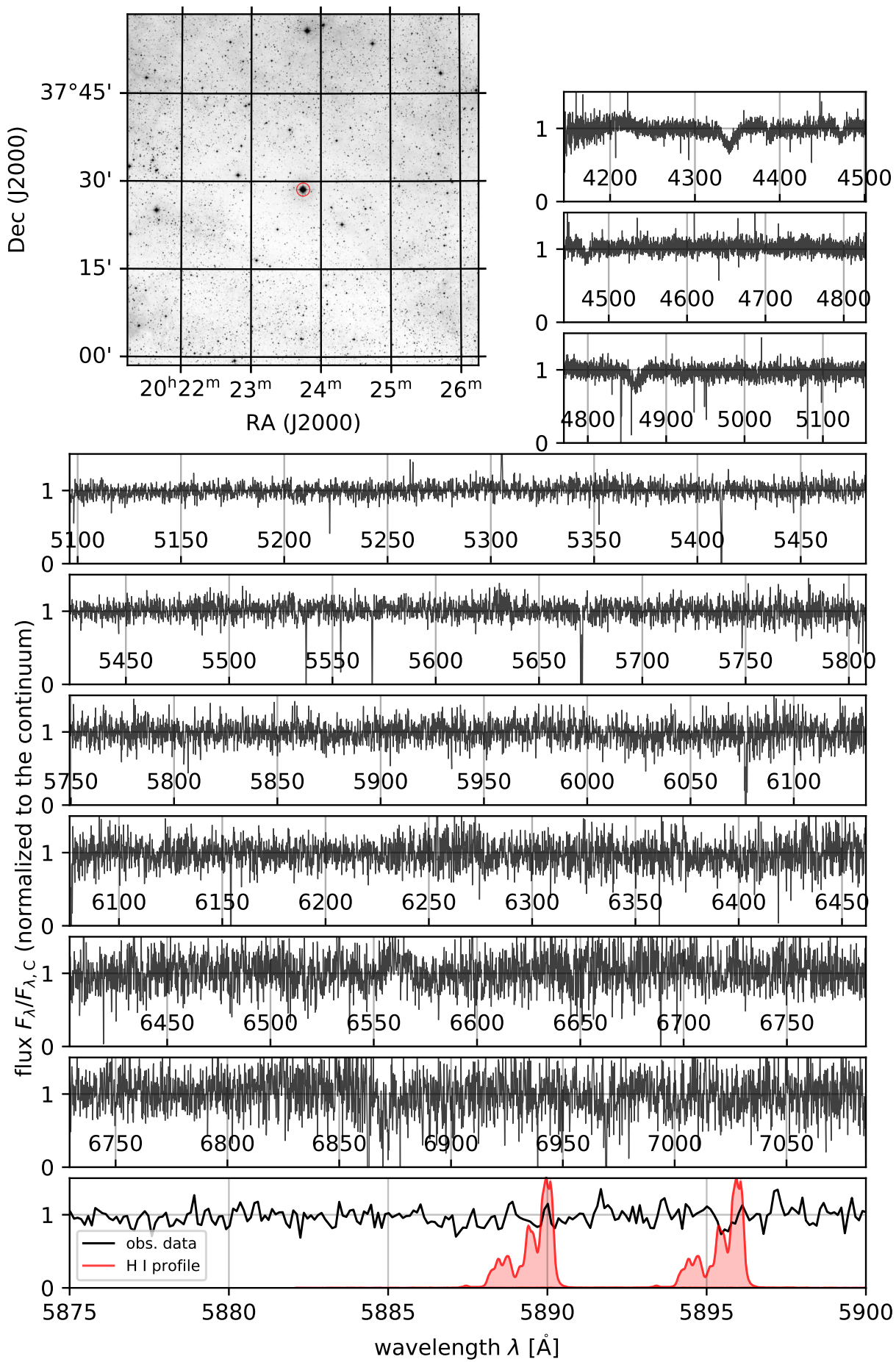
#24 - HIP100142
2021-04-26 02:36:59.327988 UTC



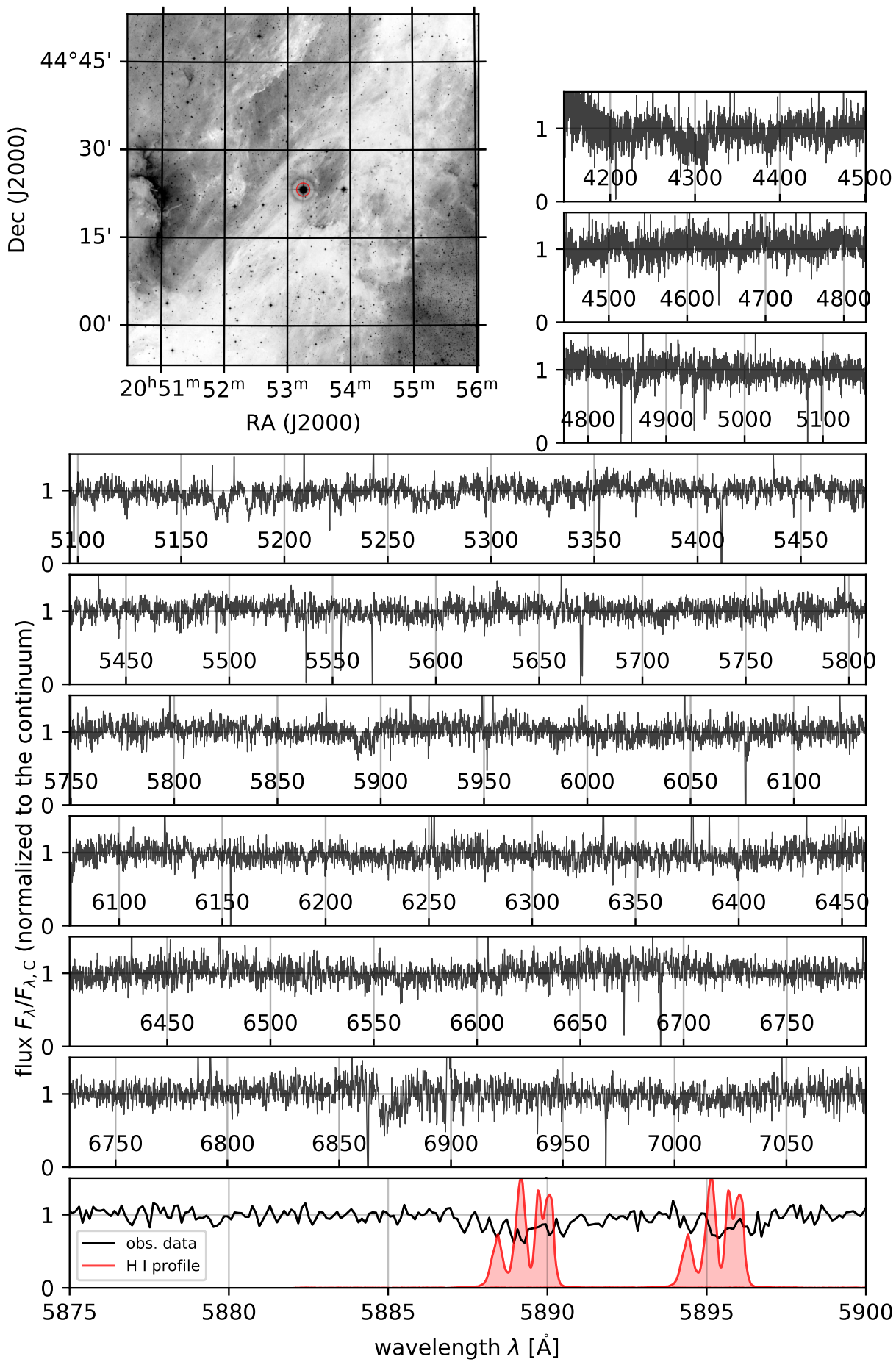
#25 - HIP100518
2021-04-26 00:37:46.271996 UTC



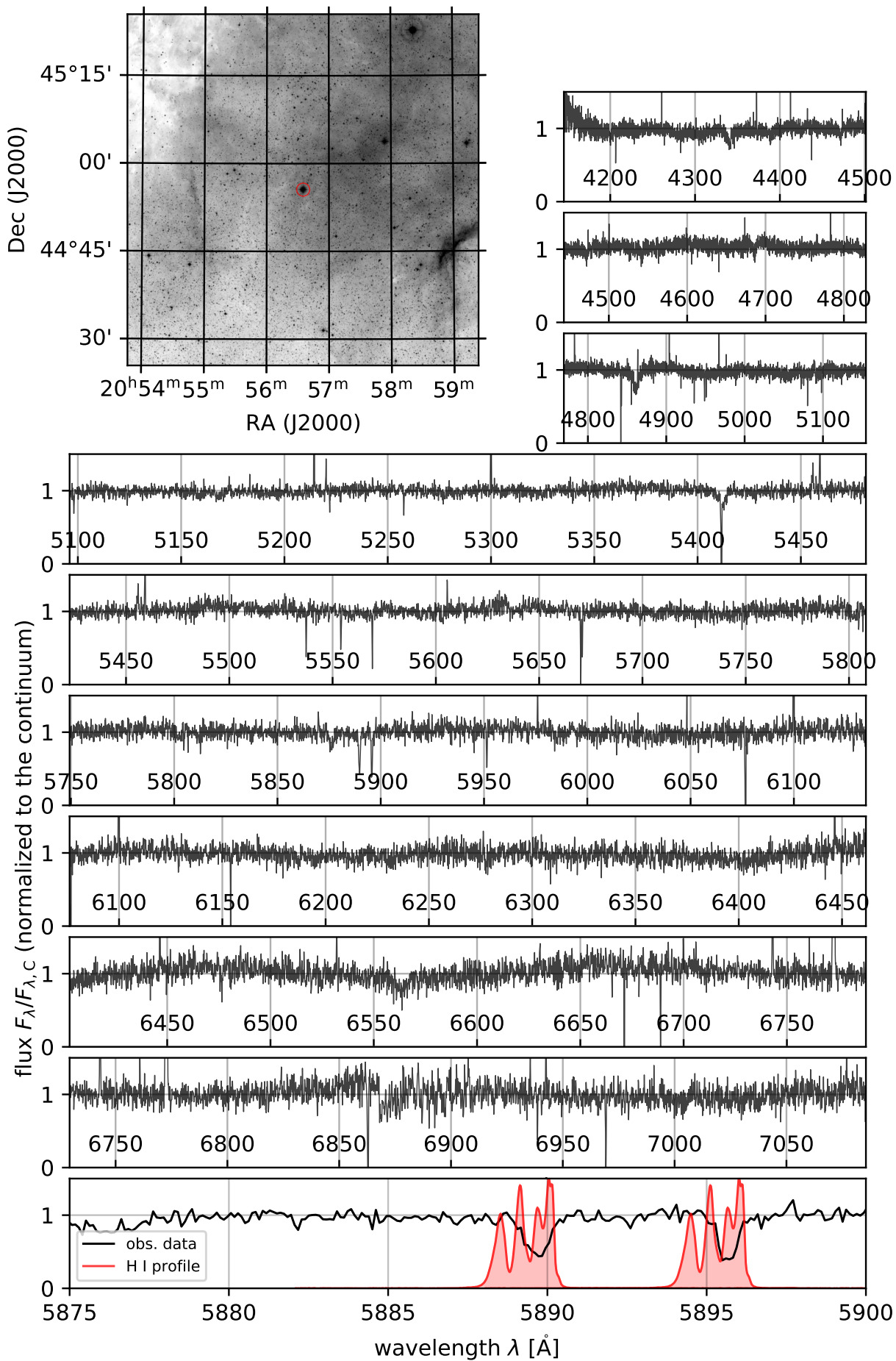
#26 - HIP100574
2021-04-26 02:16:42.816018 UTC



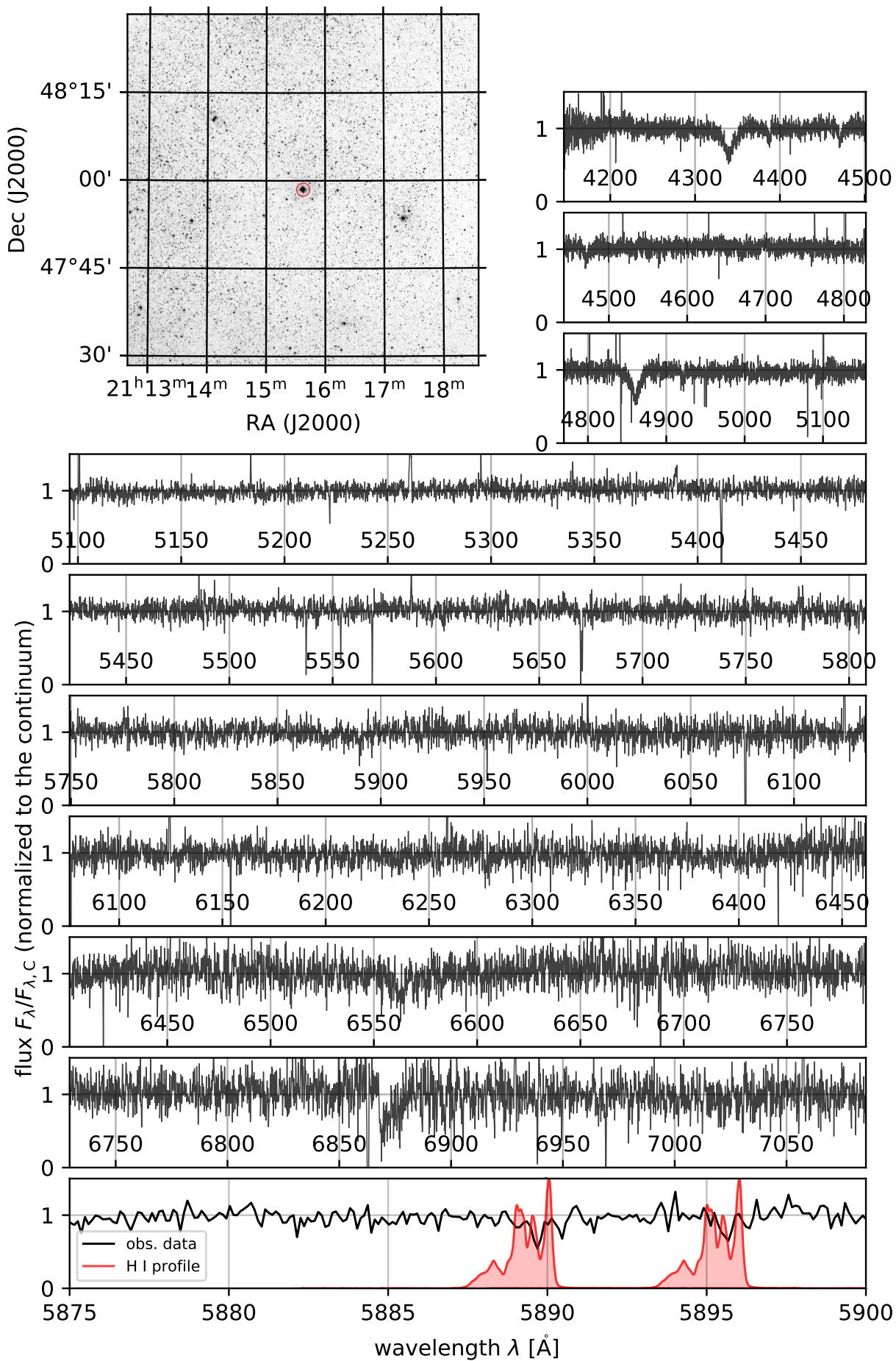
#27 - HIP103089
2021-04-26 01:09:25.344013 UTC



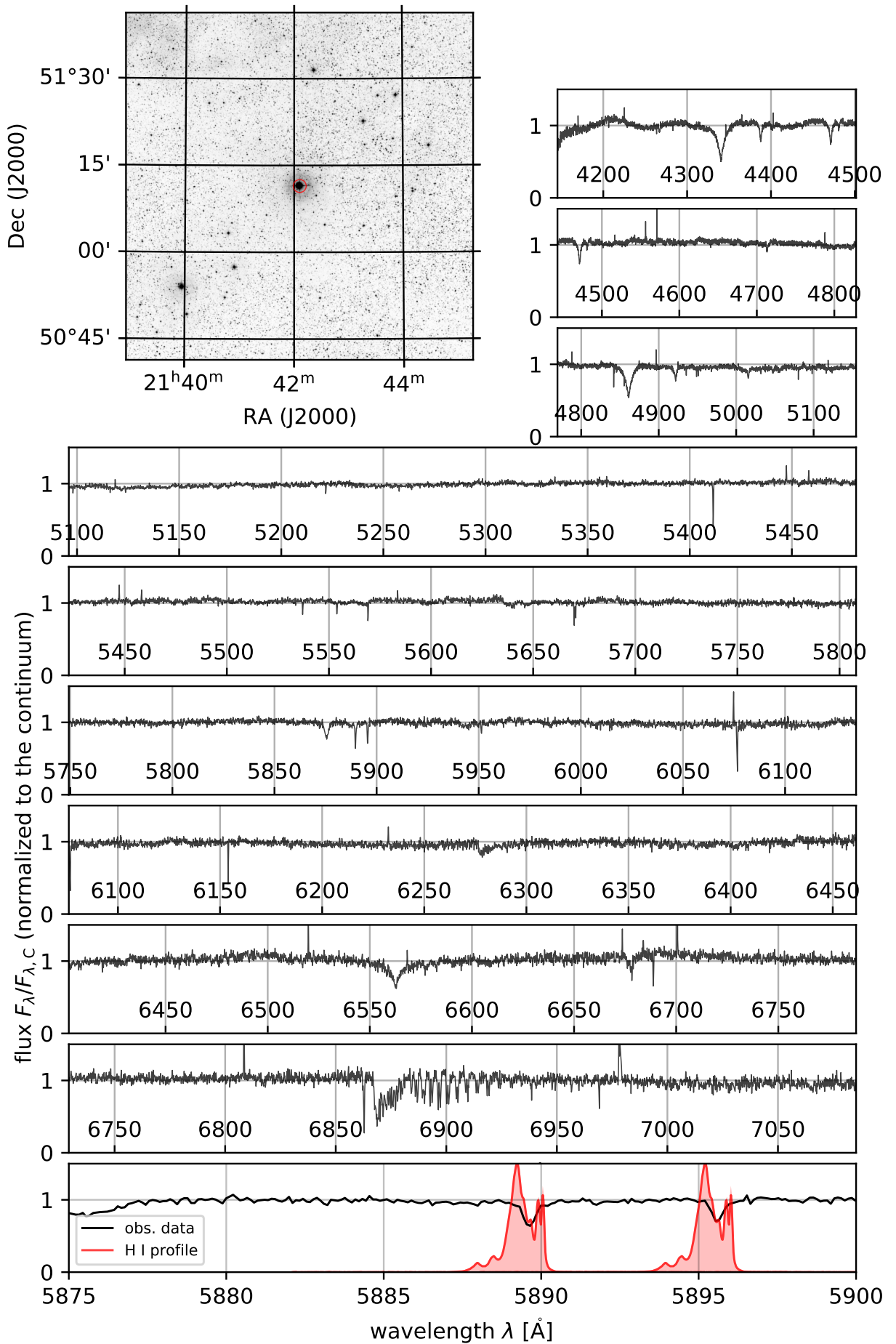
#28 - HIP103371
2021-04-26 00:12:13.535993 UTC



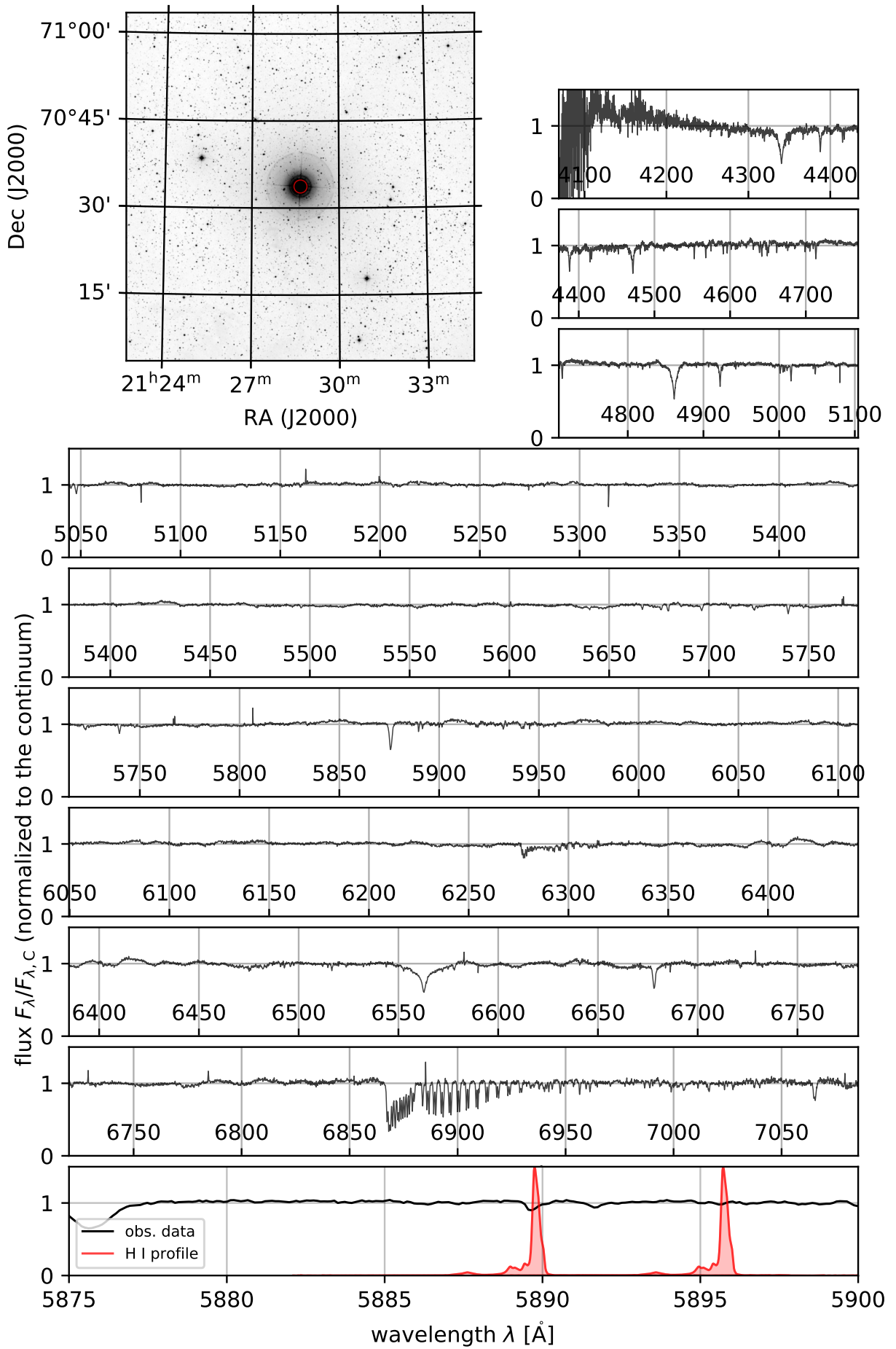
#29 - HIP104962
2021-04-26 01:56:21.120010 UTC



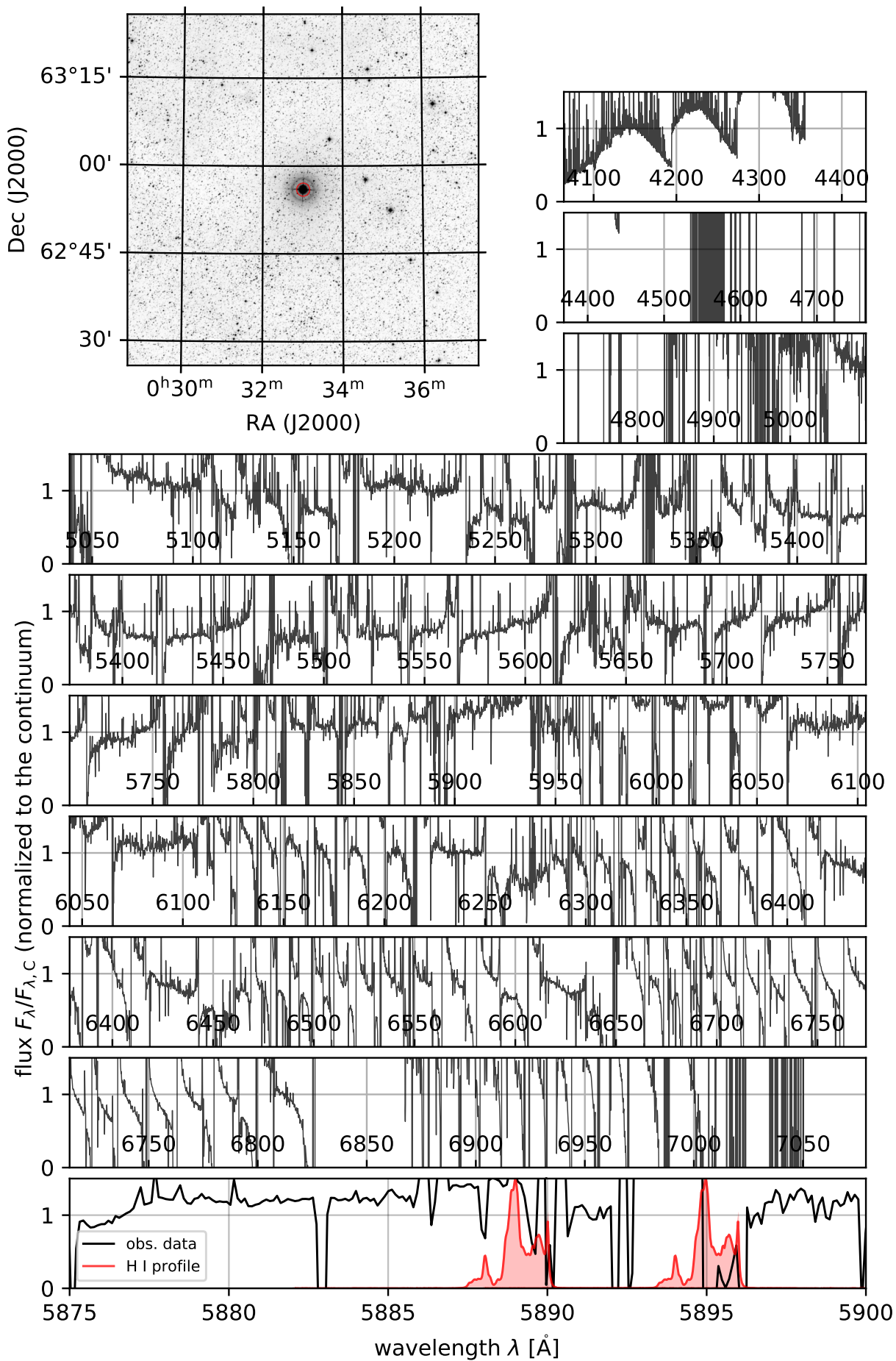
#30 - HIP107136
2021-04-26 01:35:48.191996 UTC



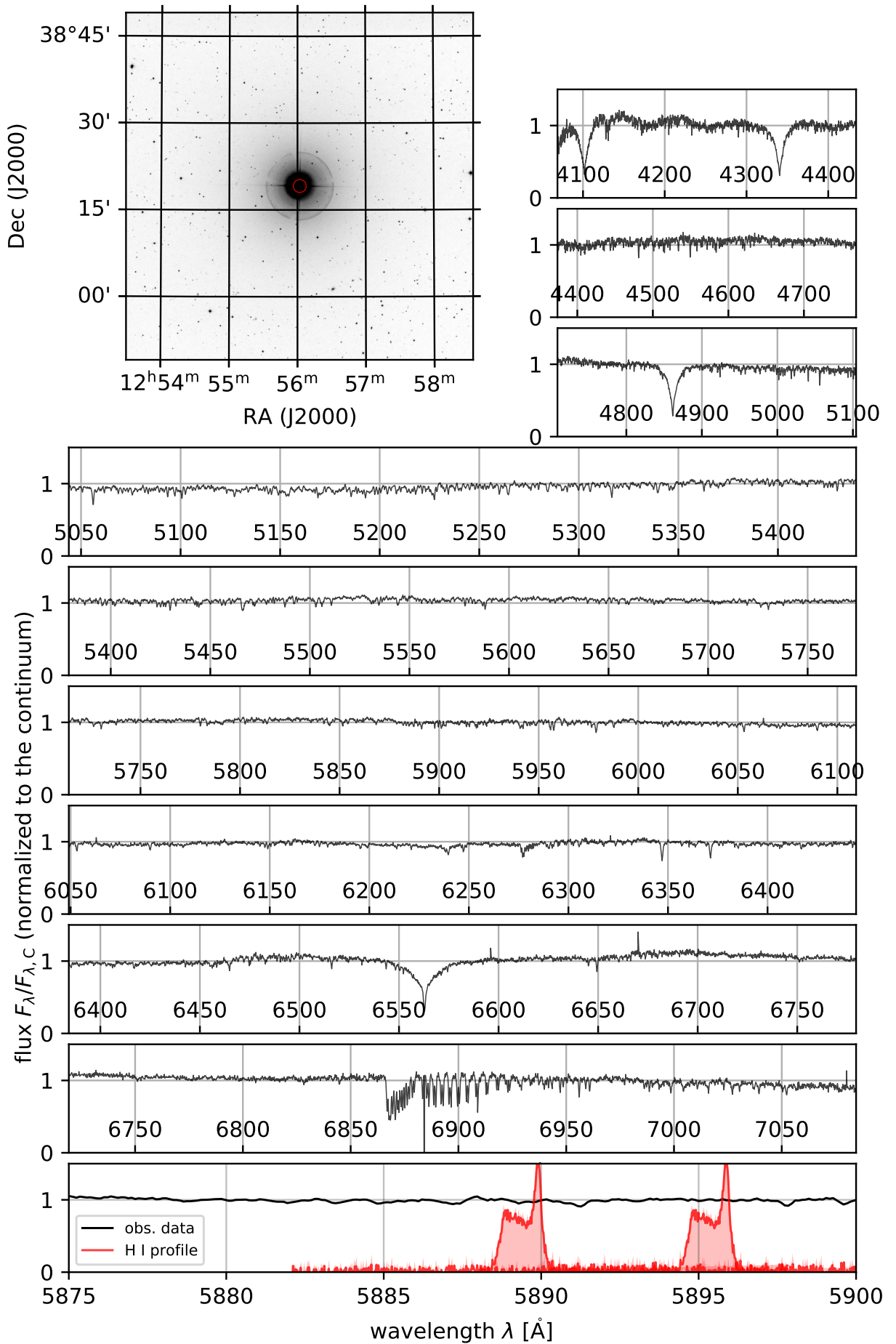
#31 - HIP106032
2021-04-22 00:18:00.000016 UTC



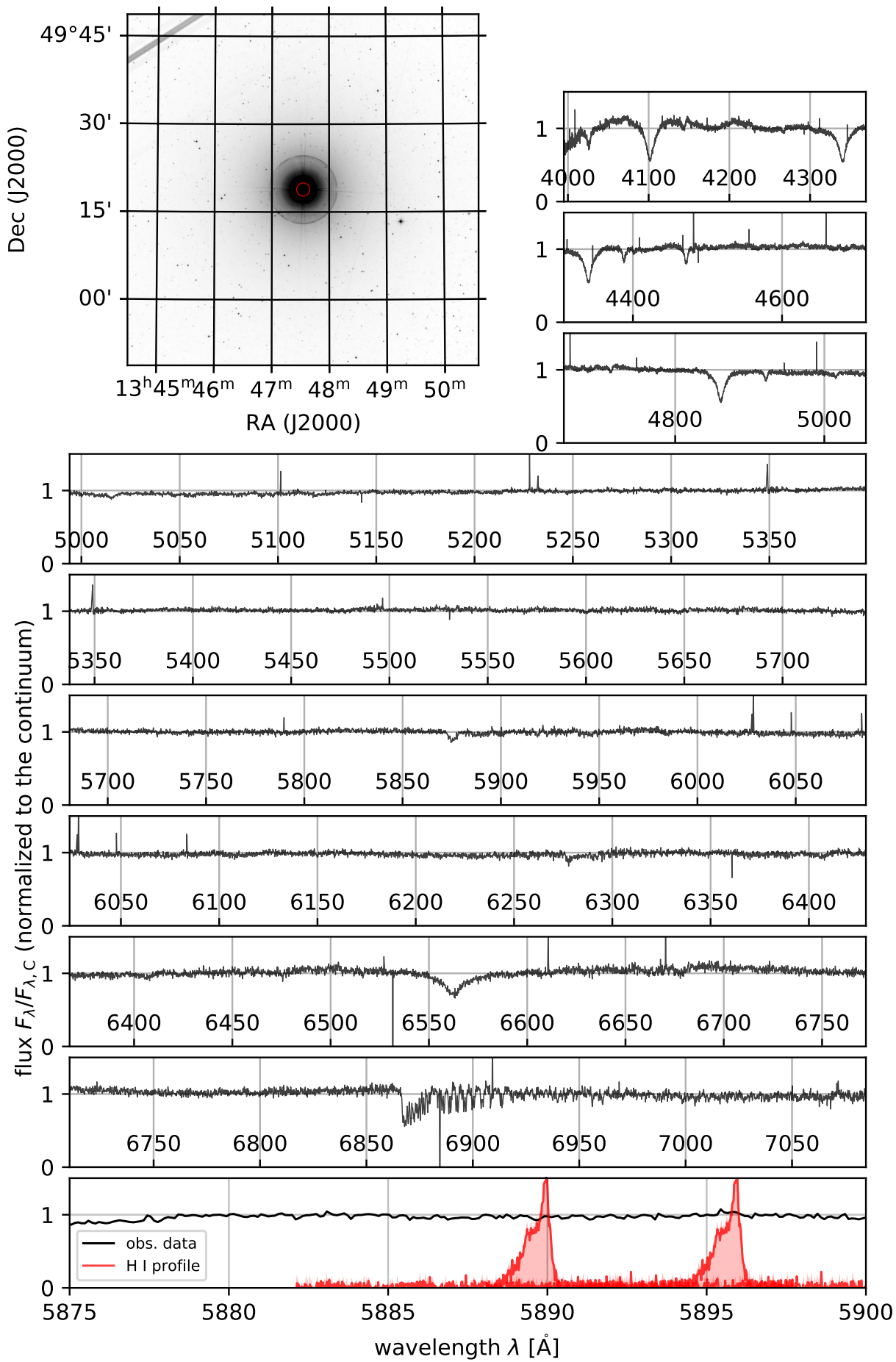
#32- HIP2599
2020-11-07 22:54:34.848005 UTC



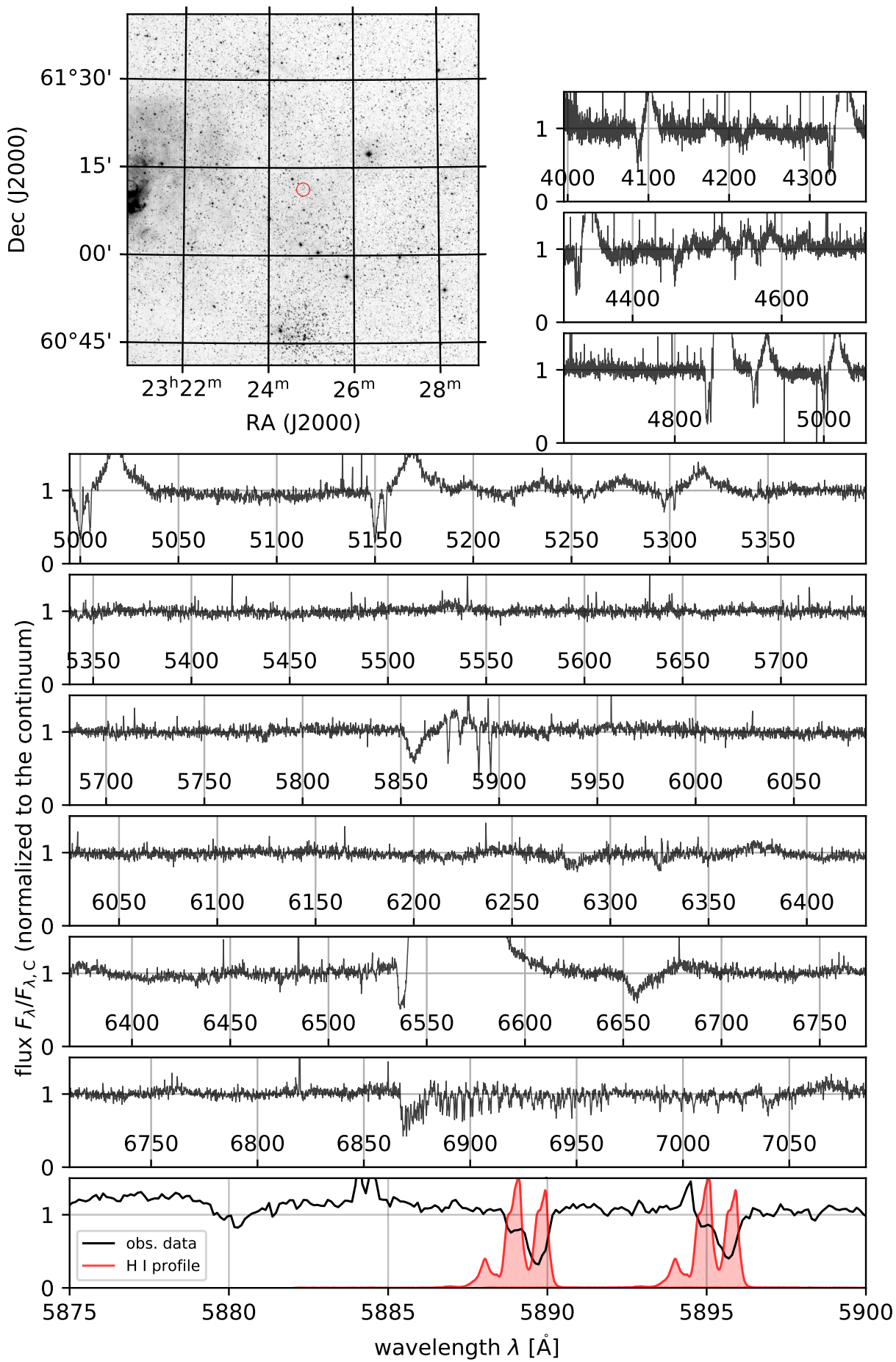
#35 - HIP63125
2021-05-08 01:06:31.680019 UTC



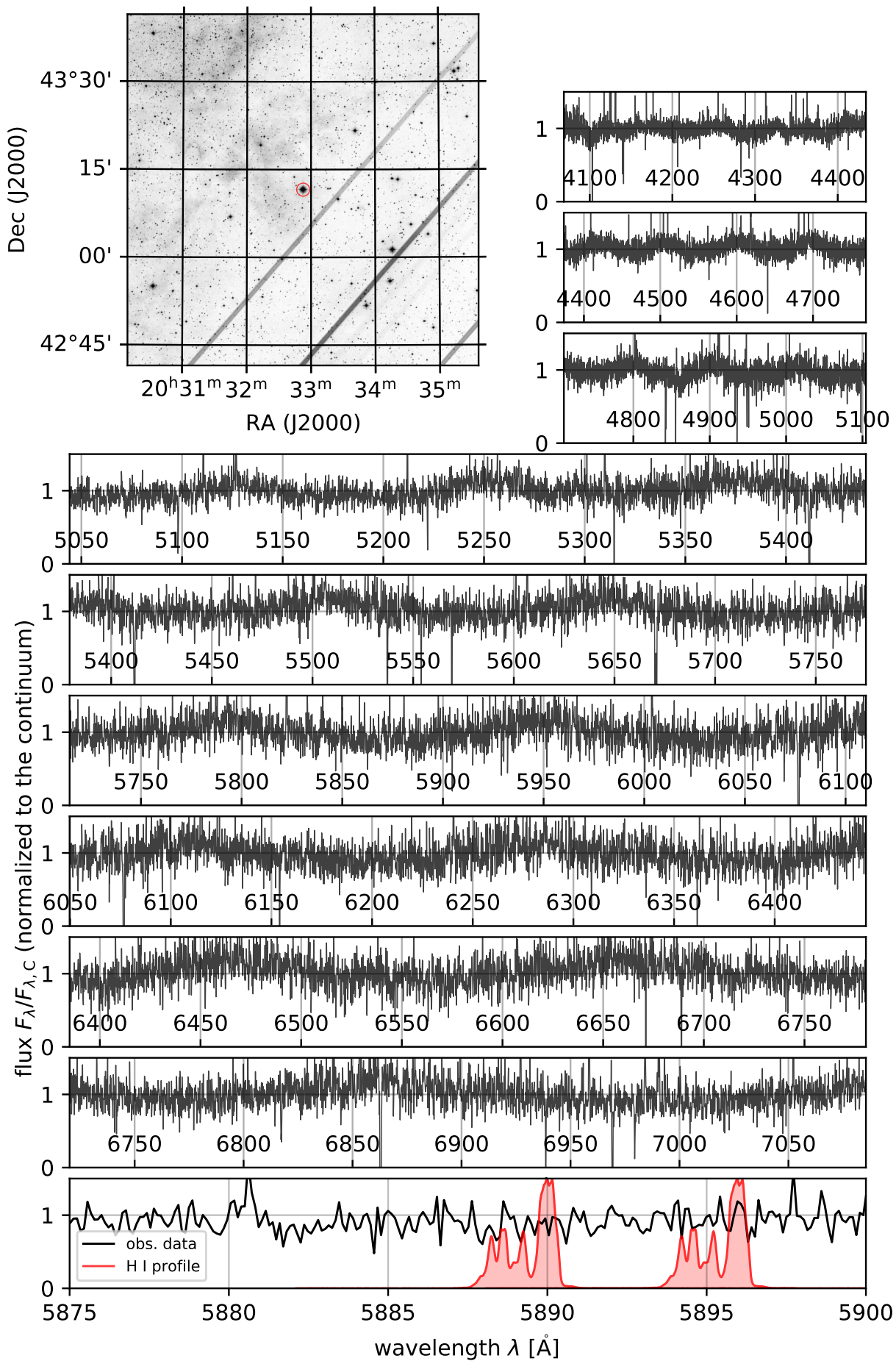
#36 - HIP67301
2021-05-07 22:56:15.936010 UTC



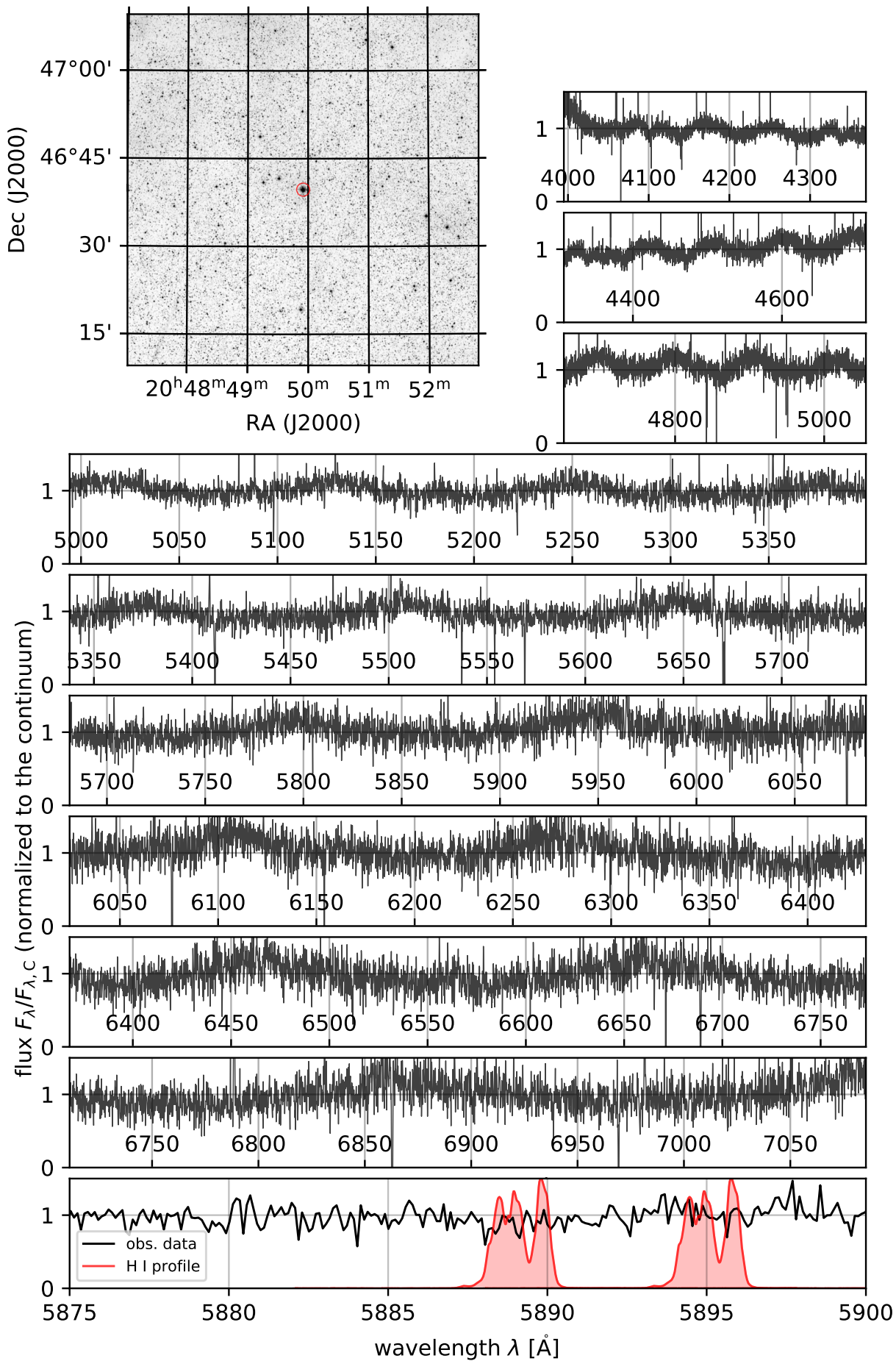
#37 - V1405Cas
2021-06-02 22:31:44.543991 UTC



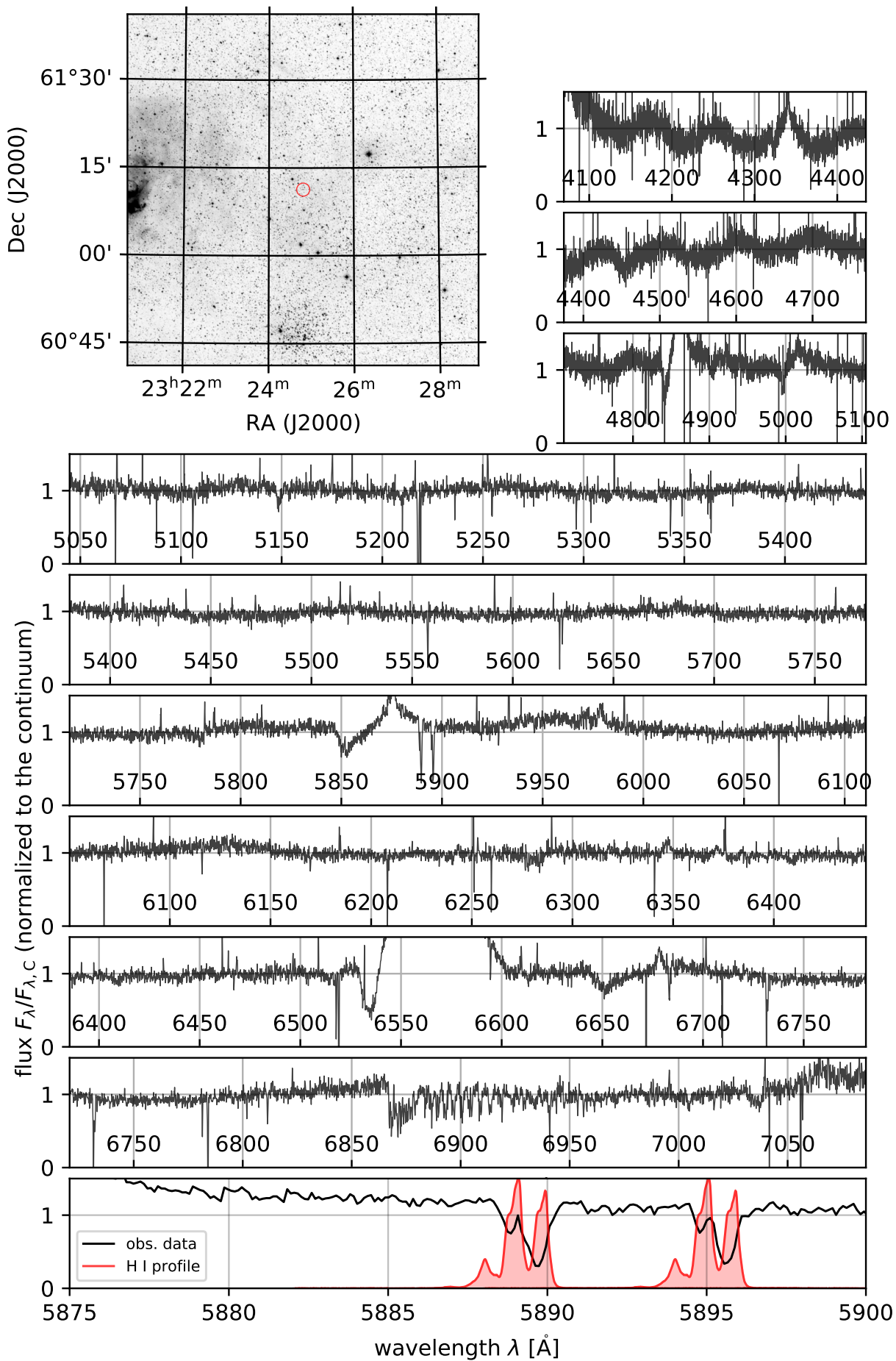
#38 - HIP101383
2021-04-25 22:17:38.687988 UTC



#39 - HIP102827
2021-04-25 23:06:38.016000 UTC



#41 - V1405Cas
2021-04-14 19:22:24.671993 UTC



#42 - V1405Cas
2021-05-10 21:17:35.807993 UTC

